Protein–Lipid Interactions and the Functional Role of Intra-Membrane Protein Hydration in the P$_{IB}$-type ATPase CopA from *Legionella pneumophila*

DISSERTATION

zur Erlangung des akademischen Grades

Doctor rerum naturalium

vorgelegt

der Fakultät Mathematik und Naturwissenschaften

der Technischen Universität Dresden

von

Elisabeth Fischermeier

geboren am 10. Juli 1984 in Nürnberg

Abstract

Membrane proteins are vital for cellular homeostasis. They maintain the electrochemical gradients that are essential for signaling and control the fine balance of trace elements. In order to fulfill these tasks, they need to undergo controlled conformational transitions within the lipid bilayer of a cell membrane. It is well-recognized that membrane protein structure and function depends on the lipid membrane. However, much less is known about the role of water re-partitioning at the protein–lipid interface and particularly within a membrane protein during functional transitions. Intra-membrane protein hydration is expected to be particularly important for ion transport processes, where the hydration shell of a solvated ion needs to be rearranged and partially removed in order to bind the ion within the transporter before it is re-solvated upon exiting the membrane protein. These processes are spatially and temporally organized in metal-transporting ATPases of the P_{IB}-subtype of P-type ATPases.

Here, the functional role of water entry into the transmembrane region of the copper-transporting P_{IB}-type ATPase CopA from *Legionella pneumophila* (*Lp*CopA) has been investigated. The recombinant protein was affinity-purified and functionally reconstituted into nanodiscs prepared with the extended scaffolding protein MSP1E3D1. Nanodiscs provide a planar native-like lipid bilayer in a water-soluble nanoparticle with advantageous optical properties for spectroscopy. The small polarity-sensitive fluorophore 6-bromoacetyl-2-dimethylaminonaphthalene (BADAN) was used as a probe for the molecular environment of the conserved copper-binding cysteine-proline-cysteine (CPC) motif which is located close to a wide "entry platform" for Cu^+ to the transmembrane (TM) channel. The systematic study of proteins with mutated metal-binding motifs using steady-state and time-resolved fluorescence spectroscopy indicates that strong gradients of hydration and protein flexibility can exist across the narrow range of the CPC motif. The data suggest that Cu^+ passes a "hydrophobic gate" at the more cytoplasmic C384 provided by rather stable TM helix packing before entering a more flexible and readily hydratable site in the interior of *Lp*CopA around C382 where the polarity is strongly regulated by protein–lipid interactions. This flexibility could also be partly

mediated by rearrangements of an adjacent amphipathic protein stretch that runs parallel to the membrane surface as a part of the cytoplasmic entry site. Using tryptophan fluorescence, circular dichroism, and Fourier-transform infrared absorption spectroscopy of a synthetic peptide derived from this segment, its lipid-dependent structural variability could be revealed. Depending on lipid-mediated helix packing interactions, the CPC motif has the potential to support a strong dielectric gradient with about ten units difference in permittivity across the CPC distance. This property may be crucial in establishing the directionality of ion transport by a non-symmetric re-solvation potential in the ion release channel of LpCopA. The experimental elucidation of these molecular details emphasizes not only the importance of intra-membrane protein water which has been hypothesized particularly for P_{IB}-type ATPases. Moreover it is shown here, that the lateral pressure of a cell membrane may provide a force that restores a low hydration state from a transiently formed state of high internal water content at the distal side of the CPC motif. ATP-driven conformational changes that induce intra-membrane protein hydration of a conformational intermediate of the Post-Albers cycle could thus be set back efficiently by lateral pressure of the cell membrane at a later step of the cycle.

Zusammenfassung

Membranproteine sind von zentraler Bedeutung für die Aufrechterhaltung aller zellulären Gleichgewichte. Dabei etablieren sie die für Signalprozesse grundlegenden elektrochemischen Gradienten und kontrollieren das empfindliche Konzentrationsgleichgewicht der Spurenelemente. Dafür verändern sie zyklisch ihre Konformation innerhalb der Lipiddoppelschicht der Zellmembran. Es ist allgemein bekannt, dass die Struktur und Funktion von Membranproteinen von der Lipidmembran beeinflusst wird. Viel weniger ist jedoch über die Rolle der Wasserumverteilung an Protein–Lipid Grenzflächen, insbesondere während der funktionellen Konformationsänderungen eines Membranproteins, bekannt. Es wird angenommen, dass die Proteinhydratation innerhalb des Membranproteins besonders wichtig für Ionentransportprozesse ist. Hierbei muss die Hydrathülle eines gelösten Ions neu angeordnet und teilweise entfernt werden um das Ion innerhalb des Transporters zu binden, bevor das Ion beim Austritt aus dem Membranprotein wieder neu solvatisiert wird. Derartige Prozesse sind sowohl räumlich als auch zeitlich in den Metalltransportern des P_{IB}-Untertyps der P-Typ ATPasen organisiert.

In dieser Arbeit wurde die funktionelle Rolle des Wassereintritts in die Transmembranregion der kupfertransportierenden P_{IB}-Typ ATPase CopA aus *Legionella pneumophila* (*Lp*CopA) untersucht. Das rekombinante Protein wurde affinitätsgereinigt und funktional in Nanodiscs rekonstituiert, welche mit dem Gerüstprotein MSP1E3D1 hergestellt wurden. Nanodiscs sind wasserlösliche Phospholipid-Nanopartikel mit vorteilhaften Eigenschaften für die Spektroskopie, in deren planare und native Lipiddoppelschicht Membranproteine eingebettet werden können. Das kleine polaritätsempfindliche Fluorophor 6-Bromacetyl-2-Dimethylaminonaphthalen (BADAN) wurde als Sonde für die molekulare Umgebung des konservierten kupferbindenden Cystein-Prolin-Cystein (CPC) Motivs verwendet. Dieses befindet sich in der Nähe einer weiten „Eintrittsplattform" für Cu^+ zum transmembranen Ionenkanal. Systematische Untersuchungen mit Hilfe von stationärer und zeitaufgelöster Fluoreszenzspektroskopie an *Lp*CopA-Proteinen mit mutierten Metall-Bindungsmotiven zeigen, dass innerhalb des kleinen Bereichs um das CPC-Motiv

starke Gradienten in Bezug auf Proteinhydratation und -flexibilität bestehen. Die Ergebnisse deuten darauf hin, dass Cu^+ eine „hydrophobe Pforte" am Zytoplasma-nahen C384 passiert, welche durch eine relativ stabile Transmembranhelix-Packung verursacht wird, bevor es eine flexibleren und leicht hydratisierbaren Bereich im Inneren von *Lp*CopA nahe C382 erreicht, wo die Polarität sehr stark von Protein–Lipid-Wechselwirkungen reguliert wird. Diese Flexibilität könnte teilweise auch durch Umordnung eines benachbarten amphipathischen Proteinabschnitts vermittelt werden, der parallel zur Membranoberfläche als Teil der „Eintrittsplattform" zum Cu^+-Transportkanal verläuft. Mit Hilfe von Tryptophanfluoreszenz-, Zirkulardichroismus- und Fourier-Transformations-Infrarotspektroskopischen Messungen an einem aus diesem Abschnitt abgeleiteten synthetischen Peptid, konnte dessen lipidabhängige strukturelle Variabilität gezeigt werden. Abhängig von der lipidvermittelten Transmembranhelixpackung kann über den Bereich des CPC-Motivs ein dielektrischer Gradient über etwa zehn Einheiten der Dielektrizitätskonstante vermittelt werden. Diese Eigenschaft kann entscheidend für die Festlegung der Richtung des Ionentransports durch ein nicht-symmetrisches Resolvatationspotential an der Ionenaustrittsstelle von *Lp*CopA sein. Die experimentelle Aufklärung dieser molekularen Details weist nicht nur auf die funktionale Bedeutung von Wasser innerhalb von Membranproteinen hin, welche vor allem für P_{IB}-Typ ATPasen angenommen wird. Sie zeigt darüber hinaus, dass der laterale Druck einer Zellmembran eine Kraft ausübt, welche in der Lage ist, einen niedrigen Hydratisierungszustand – ausgehend von einem vorübergehend gebildeten Zustand mit hohem internen Wassergehalt – wieder herzustellen. ATP-getriebene Konformationsänderungen, die den Wassereintritt in das Innere des Membranproteins während konformationeller Zwischenzustände des Post-Albers-Zyklus induzieren, könnten somit durch lateralen Druck der Zellmembran zu einem späteren Zeitpunkt des Zyklus effizient zurückgesetzt werden.

Table of Contents

Abbreviations

A.U.	arbitrary units
A-domain	actuator domain
ADP	adenosine 5'-diphosphate
ATP	adenosine 5'-triphosphate
ATR	attenuated total reflection
BADAN	6-bromoacetyl-2-dimethylaminonaphthalene
β-ME	β-mercaptoethanol
CD	circular dichroism
cfCopA	*Lp*CopA with all cysteines substituted by serin
CMC	critical micellar concentration
cmCopA	*Lp*CopA with all cytoplasmic cysteines substituted by serin
CV	column volume
DDM	n-dodecyl β-D-maltoside
DMPC	1,2-dimyristoyl-*sn*-glycero-3-phosphocholine
DOPC	1,2-dioleoyl-*sn*-glycero-3-ethylphosphocholine
DTT	dithiothreitol
ε	dielectric constant
EDTA	ethylenediaminetetraacetic acid
eV	electron volt
f	fraction
FT-IR	Fourier-transform infrared
HEPES	4-(2-hydroxyethyl)-1-piperazineethanesulfonic acid
HICT	hydrogen-bonded internal charge transfer state
HMBD	heavy metal-binding domain
ICT	internal charge transfer state
IMAC	immobilized ion affinity chromatography
IPTG	isopropyl β-D-1-thiogalactopyranoside
kB	kilobase
J	joule
kD	kilodalton
λ	wavelength
*Lp*CopA	CopA from *Legionella pneumophila*

LUV	large unilamellar vesicle
MBb	synthetic peptide of the amphipathic helix MBb of LpCopA
MD	molecular dynamics
MRE	mean residue ellipticity
MSP	membrane scaffolding protein
MW	molecular weight
MWCO	molecular weight cut-off (in kD)
v	wavenumber
N-domain	nucleotide-binding domain
Ni-NTA	nickel nitriloacetic acid
NMR	nuclear magnetic resonance
OD	optical density
oN	over night
PCR	polymerase chain reaction
P-domain	phosphorylation domain
P_i	inorganic phosphate
PMSF	phenylmethylsulfonyl fluoride
POPC	1-palmitoyl-2-oleoyl-sn-glycero-3-phosphocholine
psi	pounds per square inch
rpm	rounds per minute
RT	room temperature
SDS-PAGE	sodium dodecyl sulfate polyacrylamide gel electrophoresis
SEC	size exclusion chromatography
SERCA	sarco-endoplasmic reticulum Ca^{2+}-ATPase
SR	solvent relaxation
θ	ellipticity
TCEP	$tris$(2-carboxyethyl)phosphine
TFE	2,2,2-trifluoroethanol
TM	transmembrane
TRES	time-resolved emission spectra
Tris	tris(hydroxymethyl)aminomethane
WT	wild type

1. Introduction: complex interactions of protein, lipid, and water in membrane protein function

1.1. Homeostasis is crucial for the cell

The cell is a structurally definable, autonomous, and self-sustaining system of high complexity. In order to maintain this system it needs to delimit itself from the environment: it needs a barrier that only lets pass what is needed to sustain it. This selectively permeable barrier is the cell membrane [1]. Specialized proteins residing in the lipid bilayer mediate the passage of solutes across the cell membrane. These proteins regulate the uptake of nutrients and trace elements, the processing of signals, the establishment of (electro)chemical gradients, and manifold other substantial processes in response to various stimuli [2]. All vectorial processes across membranes either create or utilize solute gradients which need to be maintained in order to ensure cell survival. Accordingly, transmembrane transport can be divided into passive and active transport (see Figure 1.1). Passive transport of solutes is mediated primarily by channel proteins, which facilitate diffusion along a gradient by opening and closing transiently upon a specific signal. Channels play a central role in nerve signaling as well as in many other cellular processes [3, 4]. Transport of a solute against its concentration gradient can only be realized at the expense of energy [5]. This active transport can be either driven by the coupled transport of a second solute along its gradient (in symporters or antiporters) or directly by the hydrolysis of ATP. The latter process is also known as primary transport and is mediated by the membrane protein class of transport ATPases which are ATP-powered pumps. This class comprises the large family of ABC-transporters that transports organic ions as well as other small molecules, the proton-transporting V- and F-type ATPases, and the diverse P-type ATPase family of membrane proteins which almost exclusively transports cations. These TM pumps are the most elaborate transport systems and realize highly specific transport at a rate of a few up to hundreds of molecules per second [1].

A

ion channel with a single gate

closed gate   open gate

B

ion pump with alternating gates and occluded states

one gate open

other gate open
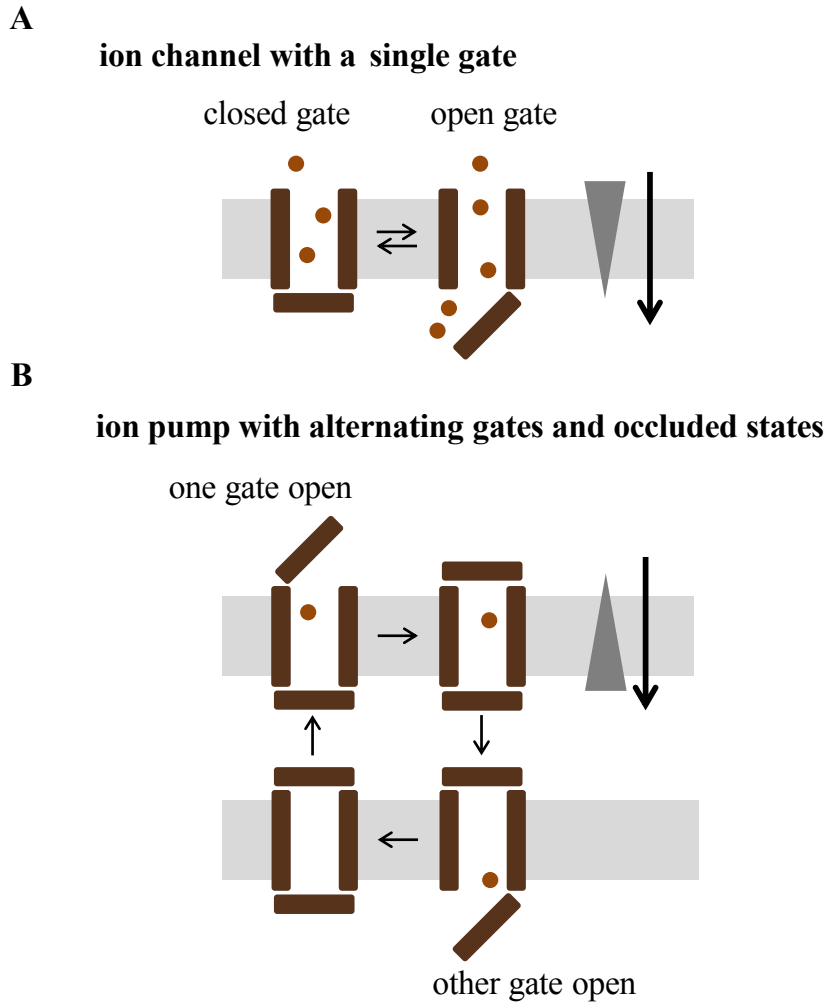
Figure 1.1: Principle of passive and active transport. (**A**) Schematic representation of an ion channel as a membrane-spanning pore. Ions (brown circles) move along their gradient through the transiently opened gate. (**B**) An ion pump translocates the ion against its concentration gradient. The ion enters from one side of the membrane through the open gate. Occlusion of the transport pathway prevents back diffusion. After opening of the alternate gate, the ion exit to the other side of the membrane and re-occlusion allows the ion pump to complete the reaction cycle. The figure is adapted from [6].

Membrane proteins comprise 20 to 30% of the encoding genome sequences [7] and are the targets of up to 60% of all current drugs [8]. These numbers emphasize the importance of understanding the complex working mechanisms of membrane proteins. However, this knowledge is lagging significantly behind the insights that have been gathered for soluble proteins [9]. This situation is due to the experimental challenges encountered when studying membrane proteins *in vitro*. Care must be taken to preserve membrane protein structure and function.

This usually requires the insertion of membrane proteins into membrane mimetic lipidic systems that sustain protein–lipid interactions to allow proper function.

1.2.   Membrane proteins depend on the lipid membrane

The lipid membrane is a bilayer of amphipathic molecules comprising a hydrophilic head directed towards the aqueous compartments and hydrophobic tails buried in the center of the membrane. It is constituted by a variety of lipid types. Species- as well as tissue-specific compositional differences substantiate the complexity of the system [10]. The interactions between a membrane protein and the surrounding lipid occur in various ways. Selective binding between a membrane protein and a certain lipid in a "co-factor-like" fashion may regulate protein function in a very specific way [11]. On the other hand, general physical properties of the lipid bilayer such as membrane curvature, hydrophobic thickness, or lateral pressure have a significant influence on tuning membrane protein structure in terms of changes in helix orientation or conformation, or changes in helix–helix interactions [12]. Moreover, the interfacial region between membrane and aqueous compartments constitutes a chemically complex environment, which offers various possibilities for noncovalent interactions with the protein [13]. The membrane–water interface is characterized by a steep polarity gradient from highly apolar near the hydrocarbon core to highly polar near the aqueous phase. Dipole-dipole interactions, H-bonding, as well as electrostatic interactions between the ester carbonyls, head groups and the surrounding (confined) water molecules and appropriate amino acid side chains can promote structural changes and folding of amphipathic protein segments and determine their orientation in the membrane [14, 15]. Thereby, these protein–lipid interactions can have a significant influence on tuning conformational changes of the membrane protein that again affect the allosteric couplings associated with the enzymatic cycle of the protein.

The fact that a transmembrane ion pump undergoes substantial conformational changes during its enzymatic cycle implies that favorable protein–lipid interactions are transient and need to be broken in certain intermediates of the reaction cycle. In other words, a working membrane protein goes through

alternating states of mismatch with respect to the hydrophobic constraints of a planar lipid bilayer. This is not expected in a micellar environment, where the amphipathic detergent molecules can constantly adapt to the membrane protein shape changes. This explains also the preferential population of certain protein states in a specific lipid composition as seen e.g. in the G-protein coupled receptor rhodopsin [16]. Conformational transitions of a membrane protein may also be associated with water re-partitioning at the lipid protein interface. It is known that protein–lipid interactions couple to hydration [17, 18], yet it is little understood how this is related to the functional role of membrane protein hydration. For example, the dynamic properties of intra-membrane protein water in proteorhodopsin are controlled by lipidic phase transitions [19] and intra-membrane protein water is taken up and released at specific states of the bovine photoreceptor rhodopsin [20].

Thus, *in vitro* studies on membrane protein structure and function in detergent micelles tend to reveal those functional processes that are largely uncoupled from the sterical constraints of a planar lipid bilayer [21, 22]. Thus, the gathered results may not reflect the full set of membrane protein structural changes and functions exhibited in the native membrane-embedded situation [23]. However, their comparison with equivalent studies in membrane-mimetic systems has been instrumental to eventually identify structural requirements provided predominantly by intra-protein constraints or by specific protein–lipid interactions [24]. As a reference system for membrane protein studies in lipidic phases, detergent-solubilized functional states of membrane proteins are thus indispensable to prove the involvement of structural constraints of the highly structured interface of water, protein, and lipids on membrane protein function.

Artificial membrane systems to study membrane proteins *in vitro*. A wide variety of lipidic systems is available that mimic the native membrane at various levels of complexity. Black lipid membranes, bicelles, or liposomes are just a few examples [21]. Over the last years a novel system, the so-called nanodiscs, has proven extremely useful for biochemical and biophysical studies. These are nano-sized phospholipid particles girded by a ring of two amphipathic α-helical

membrane scaffolding proteins derived from human apolipoprotein ApoA1 and
can be considered a "soluble portion" of planar lipid bilayer [25, 26].
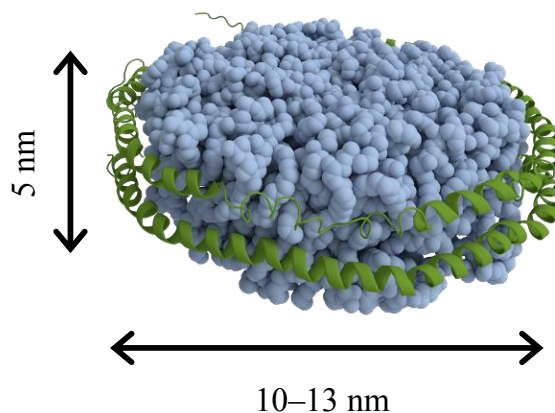
Figure 1.2: Illustration of a nanodisc. In a nanodiscs the lipid bilayer (gray) is encircled by
membrane scaffolding proteins (MSPs, green). Two amphipathic α-helical membrane scaffolding
proteins wrap around the hydrophobic edge of the lipid bilayer in an antiparallel fashion.
Depending on the choice of the membrane scaffolding protein, nanodiscs have a diameter of 10 to
13 nm. The height is defined by the lipid bilayer thickness and is approximately 5 nm. The figure
was created using the softwares PyMOL and Blender after extracting the MSP and lipid
coordinates from PDB 4V6M.

Due to their small size, a significant amount of the lipid population in nanodiscs
has an "interfacial" character, i.e. they are in contact with either the embedded
membrane protein or the membrane scaffold protein. This is also reflected in the
altered phase transition behavior and lateral pressure profile of the lipids in
nanodiscs and may actually resemble the high protein content and segregated
character of the native membrane very well [27, 28]. Nanodiscs can be prepared in
a simple self-assembly process with full control and flexibility in the choice of the
lipid composition, provide access to the membrane protein from both leaflets of
the membrane, and are virtually scatter-free due to their small size, rendering
them also an ideal membrane mimetic system for spectroscopic techniques in
solution. A central goal of the present study was to accomplish the so far not
reported insertion of a P_{IB}-type ATPase into nanodiscs. P-type ATPases are
known to undergo large conformational changes during their enzymatic cycle.
Moreover, hints on exceptional intra-protein hydration properties of P_{IB}-type
ATPases begin to emerge, rendering this protein subclass an exciting candidate
for spectroscopic investigations of protein–lipid and protein–water interactions.

1.3.   The P-ATPase transporter family: key players of ion transport

Among the families of primary ion transporters the P-type ATPase family is the most diverse one. Its representatives mediate the transport of a variety of cations, which are relevant for central cellular processes: they exchange Na^+ and K^+ in order to maintain the membrane potential, they pump Ca^{2+} back into the sarcoplasmic reticulum during muscle relaxation, they mediate the acidification of the stomach *via* proton export, and not least they regulate the fine balance between toxic and physiologically required concentrations of heavy metal trace elements like Zn^{2+} and Cu^+ [29]. Due to their central role in the cell they are also associated with a range of severe human diseases from neurological conditions like Alzheimer´s [30] to metabolic and muscle diseases [31, 32]. P-type ATPases are found in all kingdoms of life and carry out an even wider range of tasks like acidification of plant vacuoles or the detoxification from heavy metals like Cd^{2+} or Co^{2+} in bacteria [33, 34]. Thus, P-type ATPases are not only potent drug targets [35] but as well targets of antibiotics and fungicides [36]. Finally, their high degree of specificity renders them attractive templates for the development of bio-inspired metal-selective ion transport and separation methods.

According to their substrate specificity and sequence similarity, P-type ATPases are divided into five subclasses: subclass I comprises the untypical bacterial K^+-transporting P_{IA}-ATPases and the ubiquitous P_{IB}-ATPases which are all pumps for soft transition metal ions. The key players of electrogenic transport in mammals like the sarco/endoplasmic reticulum Ca^{2+}-ATPase (SERCA) and the Na^+/K^+-pump are type II P-ATPases. Subclass III represents mainly H^+-ATPases from plant and fungi. The representatives of subclass IV are the most unusual members of the family because they do not transport ions, but flip phospholipids between the membrane leaflets in order to maintain an asymmetrical membrane in eukaryotes. Subclass V, which is only found in eukaryotes, is the most elusive one with unknown substrate specificity. In total, around 500 proteins are classified as P-type ATPases up to now according to the UniProt database (www.uniprot.org) and only a handful of organisms apparently lacks P-ATPase specific genome sequences (http://traplabs.dk/patbase/NoATPases.html).

General topological features and enzymatic mechanism of P-type ATPases.
The conserved core of P-type ATPases comprises three cytoplasmic domains which form the so-called head piece and a transmembrane domain [37, 38]. The head piece comprises the distal nucleotide-binding domain (N-domain) which binds the adenosine ring of ATP thereby enabling the γ-phosphate of ATP for the covalent reaction with a conserved aspartate in the DKTG motif of the phosphorylation domain (P-domain). This covalent phosphorylation event gave the P-type ATPases its name [39]. Moreover, a Mg^{2+} ion interacting with the DKTG and the GDGxND motifs of the P-domain is crucial for the correct orientation of the attached λ-phosphate and plays a key role for the energy transduction during the reaction cycle [40]. The third cytoplasmic domain, the actuator domain (A-domain) is responsible for the dephosphorylation of the P-domain. Here, the conserved TGE motif plays an important role. The central core of the TM part of P-type ATPases is formed by six helices and harbors the binding sites for the transported ion. A conserved proline residue on TM helix M4 divides this helix into two parts, thereby creating an open space and exposing amino acid side chains that are necessary for ion coordination [41]. Additional subclass specific TM helices are possible.

The cyclic transport mechanism of all P-type ATPases follows the alternating-access model [42] and is named the "Post–Albers cycle" [43, 44] after the scientists who described it for the first time. During this enzymatic cycle, P-type ATPases undergo the very large conformational changes. Generally, the protein alternates between the E1 and E2 states, characterized by high and low substrate affinity, respectively. In Figure 1.3 the general transport cycle is illustrated. In the E1 state, ATP is bound to the N-domain while phosphorylation is prohibited due to the position of the A-domain. The exported ion(s), enter from the cytoplasmic side and bind to the TM binding site constituted by residues on the helices M4, M5, and M6. Moreover, the A-domain is triggered to tilt away from its prior position thereby allowing the close interaction of the λ-phosphate of ATP with the conserved aspartate in the DKTG motif of the P-domain. This leads to the occlusion of the transported ions within the TM domain of the ATPase. Upon phosphorylation of the aspartate (E1P state), the TM ion channel opens to

the extracellular side (E2P state). The ADP bound in the N-domain is exchanged for ATP and the A-domain rotates back to the P-domain thereby exerting traction on the helices M1, M2, and M3 leading to the release of the ions due to a lowered binding affinity. In this step binding of counter ions may take place [45, 46]. The channel now closes again. As a result of the A-domain rotation, its TGE loop is now close to the phosphorylated aspartate in the P-domain, thereby facilitating the hydrolytic dephosphorylation *via* the nucleophilic attack of a water molecule (E2 state) [40]. The relaxation to the E1 state concludes the reaction cycle.
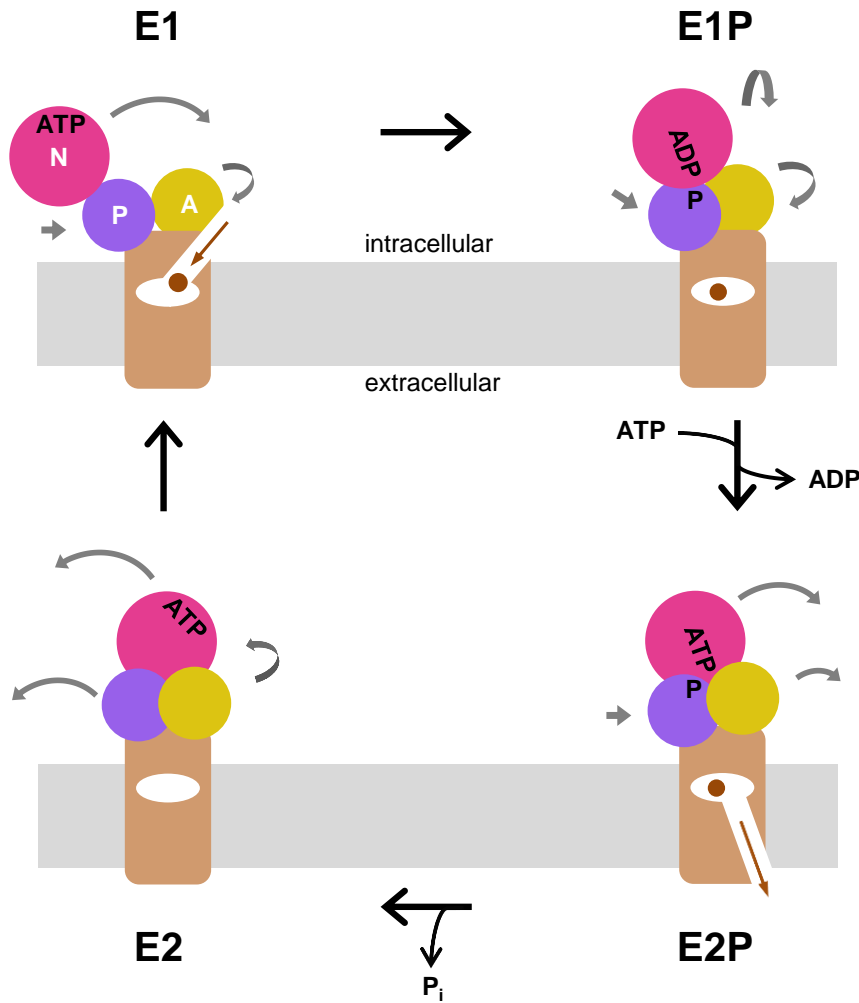
Figure 1.3: Schematic representation of the P-type ATPase transport cycle. The nucleotide-binding- (N), phosphorylation- (P), and actuator- (A) domains are represented in magenta, purple, and yellow, respectively. The TM part is shown in light brown. Gray arrows indicate the movements of the cytoplasmic domains during the transport of the ion (shown in brown). Only the major steps of the transport cycle are shown. In the E1 state, the binding of the exported ion(s) leads to the close interaction of the λ-phosphate of ATP in the N-domain with the conserved aspartate in the P-domain. This also triggers the occlusion of the transported ions. Upon phosphorylation of the aspartate (E1P state), the ion channel opens to the extracellular side (E2P state). ADP is exchanged for ATP and the ions are released. The subsequent dephosphorylation of the aspartate in the P-domain is facilitated by the A-domain (E2 state). The relaxation of the ATPase to the E1 configuration concludes the reaction cycle. See text for further details. The scheme is adapted from [47].

Primarily, the knowledge on the mechanistic cycle of P-type ATPases has been gathered through structural and functional studies of the P_{II}-ATPases SERCA and the Na^+/K^+-pump [40, 48]. Although the core topology is the same for all P-type ATPases and the transport mechanism follows the principle as described above, several subclass specific features can be found. This includes additional subclass-

specific domains as well as differences in ion transport stoichiometry and unique mechanistic features as will be described in the next section.

1.4. The unique features of Cu^+-transporting P_{IB}-ATPases

P_{IB}-type ATPases are found in all kingdoms of life. They are the key players of metal ion homeostasis by mediating the selective transport of both transition metal trace elements like Zn^{2+} and Cu^+ as well as detoxification from heavy metals like Co^{2+} or Cd^{2+} [49]. Thus, they are also of interest for selecting or engineering microorganisms for applications in bioremediation or bioleaching [50]. Defects in the human Cu^+-ATPases ATP7A and ATP7B cause the severe hereditary Menkes and Wilson's disease, respectively, and transition metal disparities are also associated with gastrointestinal diseases or neurological conditions [51, 52].

Physiology of copper homeostasis. The central importance of metal homeostasis can be, on the one hand, understood by the large number of transition metal dependent enzymes, which comprise 30 to 45% of all enzymes known to date [49]. For instance, copper is an essential co-factor of most oxidases which are involved in mitochondrial respiration, iron metabolism or radical defense [53, 54] as well as in electron transfer proteins [55]. On the other hand, free Cu^+, which is the exclusive redox state of copper in the intracellular milieu, is highly toxic in the cell due to its high redox potential. Therefore, Cu^+ is always coordinated in the cytoplasm by low-molecular weight chelators, like cysteine and glutathione, or specialized copper binding proteins, so-called copper chaperones. Nevertheless, in order to tightly regulate total cellular Cu^+-levels, sophisticated homeostasis systems are required. These vary among the kingdoms of life, but P_{IB}-type ATPases always play a key role. In eukaryotes, copper uptake into the cell is mediated by the homotrimeric CTR1 copper channels [55]. P_{IB}-type ATPases are located in the membrane of the trans-Golgi network and transport Cu^+ into the lumen, where it is then loaded onto Cu^+-dependent enzymes or into secretory vesicles destined for excretion. Relatively little is known about the mechanism of copper uptake into prokaryotic cells. There are indications of ABC transporters being involved [56, 57] as well as for P_{IB}-type ATPases themselves, but the evidence is still uncertain [58-60]. On the other hand, the Cu^+ export mechanism

of prokaryotes is relatively well studied. Apart from the gram-negative bacterium *E. coli* that uses the Cus (cation efflux) system, practically all other cells use P_{IB}-type ATPase for copper export [61].

Unique topological and mechanistic features of Cu^+-transporting P_{IB}-type ATPases. P_{IB}-ATPases exhibit several subclass-specific structural elements: they feature two additional N-terminal TM helices, at least one N-terminal cytosolic heavy metal binding domain (HMBD) and in some cases C-terminal HMBDs [62, 63]. In 2011, the knowledge about the structure of P_{IB}-ATPases was considerably deepened as the crystal structure of CopA from *Legionella pneumophila* (*Lp*CopA) was solved, which was the first crystal structure of a P_{IB}-ATPase [64]. See Figure 1.4 for the topology and structure of *Lp*CopA. Although not resolved in the crystal structure due to weak electron density, it is known from studies on individually expressed and purified HMBDs, that they possess a ferredoxin-like fold [65, 66] and bind heavy metals, either in histidine-rich sequences or MxCxxC motifs. To date, the role of the HMBD is still a matter of scientific debate and it is emerging that the function(s) might vary among the different representatives of the Cu^+-ATPases [67-69]. Usually, reduced ATP-hydrolytic activity is found as a result of HMBD removal [67, 70]. Moreover, it is assumed to play a regulatory role in auto-inhibition of protein activity in the absence of Cu^+ [71]. Furthermore, it might also be involved in translocation of Cu^+ from cytoplasmic chelators or chaperones to the TM Cu^+-binding sites *via* the CxxC sequence motifs found in the HMBD as well as in chaperones [72].

The crystal structure of *Lp*CopA revealed a putative Cu^+-transfer mechanism to the TM Cu^+-channel between either a soluble chaperone or the N-terminal HMBD itself *via* the so-called "entry platform". This platform is constituted by the class-IB-specific TM helices MA and MB together with M1. Strikingly, the helix MB kinks at the cytosol–membrane interface and forms an amphipathic helix, which will be denoted in the following as MBb (see also Figure 1.4 B and C). Notably, the helix-breaking glycine residues at the N-terminus of MBb and the amphipathic nature of MBb are conserved among all P_{IB}-type ATPases. The helix MBb presents mostly positively charged residues towards the cytoplasm thereby complying with the "positive-inside" rule [73].

Moreover, the positively charged residues could mediate electrostatic interactions with the negatively charged surface of the HMBD or soluble copper chaperones [74].

Generally, amphipathic helices play an important role in positioning a TM protein in a proper orientation relative to the lipid bilayer [75]. They are not only a hallmark of P-type ATPases [76, 77] but are also a typical motif in other transmembrane protein families like GPCRs [78, 79], ion channels, or receptors [80]. However, their function may go beyond a sole anchoring of the membrane protein. For instance, in *Lp*CopA MBb might act as a flexible structural element rather than a static platform and could be involved in rearrangements of the adjacent TM helices which bear the copper binding residues. Thereby copper coordination geometries and binding affinities could be varied throughout the copper transport cycle.

The Cu$^+$-transport mechanism. Additionally to the specific ion-binding geometries that change through conformational changes during the enzymatic cycle, the nature of the amino acids involved in ion coordination is fundamental in determining ion-specificity. The "hard and soft (Lewis) acids and bases concept" [81] rationalizes the amino acid preferences of different types of ions: hard, that is non-polarizable, Lewis acids like the alkali or alkaline earth metals Na$^+$ or Ca^{2+} will prefer hard Lewis bases like carboxylates for coordination, while soft, that is polarizable, Lewis acids like the transition metal Cu$^+$ will favor thiol or thioether functional groups. This explains why the metal binding sites of P$_{IB}$-type ATPases are predominantly constituted of cysteines and methionines as well as of the "intermediate" Lewis base histidine [41]. This is seen also in the Cu$^+$-transporting P$_{IB}$-type ATPase *Lp*CopA: the low-affinity copper "entry site" is presumably formed by M148 together with E205 and D337 on helices M1, M2, and M3, respectively [64, 67], while C382 and C384 on helix M4, and M717 on helix M6 constitute the purely sulfur-based high-affinity TM binding site [68, 82]. The cysteine-proline-x ion binding motif on helix M4, with x being cysteine, serin, or histidine [41, 82, 83] is conserved among Cu$^+$-transporting P$_{IB}$-type ATPases. For the exit pathway of the Cu$^+$-ion, presumably the sulfur-ligands M100 and M711 together with E189 play an important role [47].
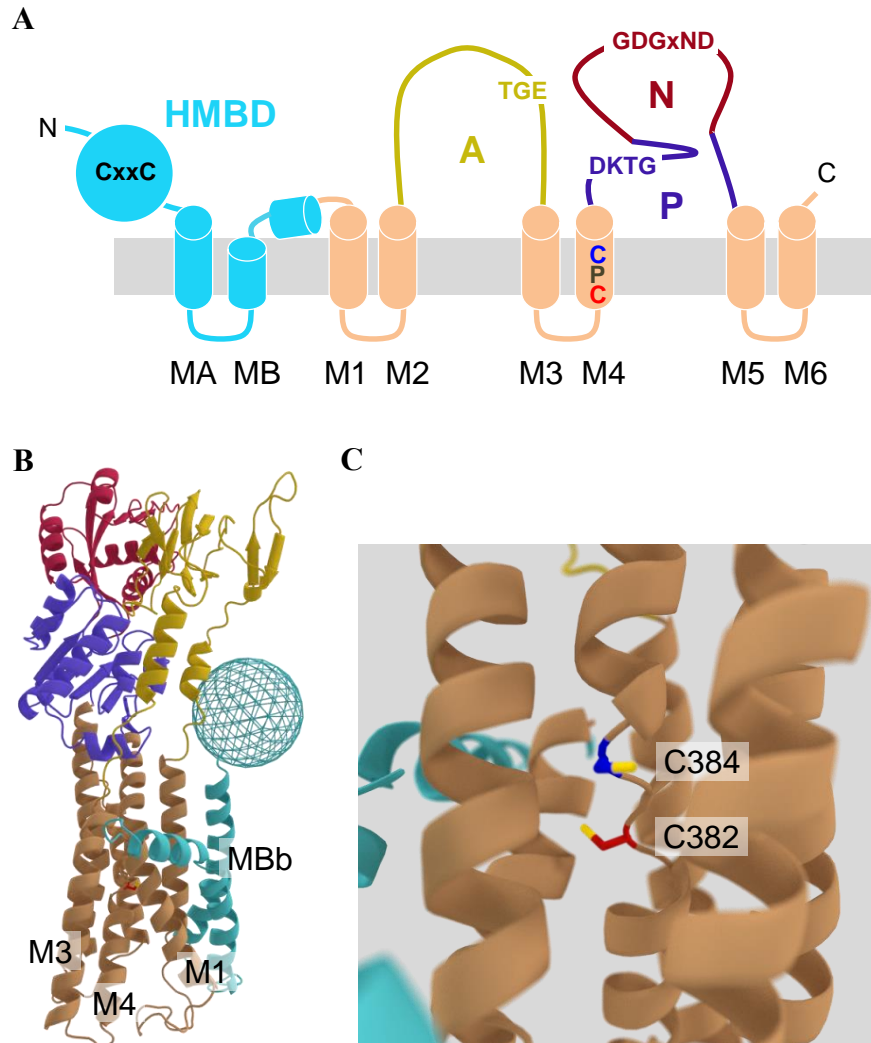
**Figure 1.4: Topology and structure of the P_{IB}-type ATPase CopA from *Legionella
pneumophila*.** The color code is as in Figure 1.3. The two additional N-terminal TM helices MA
and MB and the heavy-metal binding domain (HMBD) are shown in cyan. The CPC copper-
binding motif on helix M4 is shown in red (C382) and blue (C384). (**A**) Topology model of
*Lp*CopA. The conserved sequence motifs CxxC (HMBD), TGE (A-domain), DKTG (P-domain),
and GDGxND (N-domain) are indicated. (**B**) Tertiary structure of *Lp*CopA. The HMBD was not
resolved in the crystal structure. Thus, its estimated position is indicated by an open sphere. (**C**)
Close-up of the copper-binding CPC motif. The view is rotated by approximately 120° compared
to B. The figures B and C were created from PDB 3RFU.

Additionally to the subclass-specific features in topology and sequence, there is
accumulating evidence that Cu^+-ATPases couple dephosphorylation and ion
extrusion differently than the prototypical P_{II}-type ATPases. In P_{II}-type ATPases
the transport channel occludes during the transition from the phosphorylated E2P
to the dephosphorylated $E2.P_i$ state. This occlusion is stimulated by the release of

the exported ions to the luminal side and the binding of proton counter ions [84, 85]. However, the comparison of the copper-free structure of the dephosphorylation transition state E2.P$_i$ of the Cu$^+$-ATPase *Lp*CopA [64] with the structure of the preceding E2P state [47] revealed only little structural differences. The copper transport channel appears to stay in a luminally open configuration. Moreover, crystal waters could be detected reaching up to the copper-binding CPC motif. Remarkable intra-protein hydration was also seen in molecular dynamics calculations of the protein. This striking characteristic may play an important role in the ion exit mechanism of Cu$^+$-ATPases. As no counter-ion transport has so far been evidenced for this subclass, an alternative "pulling force" for the exit of the ion is needed [86, 87]. Thus, an internal water or proton network, potentially coordinated by the conserved tyrosine/tyrosinate Y688 on helix M6 and the conserved carboxylate E189 on helix M2, may mediate the ion exit through rehydration of the copper ion [47, 88].

However, it is noteworthy pointing out that the findings detailed above have been deduced from experiments that were performed in the absence of a lipidic phase. The lipid membrane imposes structural constraints leading on the one hand to the structure stabilization of the inserted membrane protein. On the other hand, the working ATPase has to go through alternating conformational states which implies also transient mismatch with respect to hydrophobic constraints of the lipid bilayer. In P-type ATPases, which are known to undergo very large conformational changes during their enzymatic cycle, this factor is expected to particularly carry weight. Moreover, the general lipid–protein interactions and the lateral pressure exerted by the lipid membrane define the degree to which water is expelled from the membrane-inserted protein and are therewith assumed to have a significant influence on intra-protein hydration and therewith on protein function [18, 89, 90].

1.5. Aim of this work

Cu$^+$-transporting P-type ATPases play a key role in cellular copper homeostasis. The understanding of their structure and function has to a great extent been extrapolated from the knowledge about the prototypical P-type ATPases

Na$^+$/K$^+$-ATPase and SERCA. However, subclass-specific structural elements as well as recent studies indicating unique features of the copper transport mechanism motivate the revaluation of this approach. According to crystallographic snapshots of the Cu$^+$-ATPase CopA from *Legionella pneumophila*, together with molecular dynamics calculations and biochemical studies, the transport mechanism of these ion pumps differs significantly in the ion entry as well as the ion release step. Particularly, water accessibility in the extracellular release channel appears to be maintained, whereas an occluded state is predicted for the prototypical catalytic cycle of SERCA. Likewise, the effect of the native lipidic environment on the conformation of the transmembrane pump has not been studied but can be considered crucial for the stabilization of conformational sub-states. In this context, the role of interactions between an amphipathic protein stretch and the lipid membrane at the interfacial copper entry site is of special interest. Furthermore, the dependence of intra-protein hydration at the intramembranous copper binding site on the structural constraints of a lipid membrane has not yet been addressed. Here, it is particularly the lateral pressure of the lipid bilayer that is expected to affect transmembrane helix interactions as opposed to a more flexible and, therefore, easier hydratable micellar state of the protein. A comparison between the two systems using site-specific spectroscopic probes could thus reveal the link between local intra-protein hydration and structural flexibility. Therefore this doctoral work aimed at

I.   Establishing an *in vitro* system to study *Lp*CopA in a micellar state and in a native membrane environment by reconstituting the purified recombinant protein into phospholipid nanodiscs.

II. Studying intra-protein hydration in the environment of the intramembranous CPC copper-binding motif under the influence of a lipidic phase using a polarity-sensitive fluorescent probe.

III. Characterizing the amphipathic helix MBb at the copper entry site with the help of a synthetic peptide in order to understand its possible role as a membrane surface-attached protein element for the early steps of copper uptake.

2. Material and methods

2.1. Materials and instruments

Chemicals and consumables. All substances were obtained in the highest quality available. Table 2.1 lists all chemicals used in this work.

Table 2.1: List of all used chemical and its suppliers

supplier	chemicals
Avanti Polar Lipids (Alabaster, USA)	DMPC, DOPC, POPC, E.coli total lipid extract
Bio-Rad (Munich, Germany)	Bio-Beads SM-2 protein assay dye reagent concentrate
GE (Fairfield, USA)	His SpinTrap, HisTrap HP 1 ml and 5 ml columns, Superdex 200 10/300 GL column, PD-10 and PD-10 mini desalting columns, track etched polycarbonate membranes
Invitrogen (Carlsbad, USA)	Novex Sharp Prestained protein size standard
IBA (Göttingen, Germany)	Strep-Tactin superflow resin
Roche (Basel, Switzerland)	DNaseI
Carl Roth (Karlsruhe, Germany)	agar-agar, antibiotics (ampicillin, kanamycin, chloramphenicol), ß-mercaptoethanol, boric acid, disposable microcuvettes, DDM, glycine, HEPES, HCl, IPTG, KCl, KH_2PO_4, L-glutathione, $MgSO_4$, motivase, Rotiphorese® Gel 30 (37.5:1), N,N,N',N'-tetramethylethylendiamin, tryptone/peptone, SDS, Tris base, yeast extract
Sartorius (Göttingen, Germany)	Vivaspin15 Turbo centrifugal devices (MWCO 10,000), 0.22 µm filters
Sigma Aldrich (Munich, Germany)	ammonium molybdate, ammonium persulfate asolectin, citric acid, Coomassie Blue G-250, L-cysteine, Malachite Green, NaOH, PMSF, SIGMAFAST™ Protease Inhibitor Cocktail Tablets (EDTA-free), TFE, Whatman filter paper #2
Stratec (Birkenfeld, Germany)	Invisorb® Spin Plasmid Mini Two
VWR International (Darmstadt, Germany)	acetic acid, Bromophenol Blue, chloroform, Coomassie Blue R-250, $CuSO_4$, D-desthiobiotin, DTT, EDTA, ethanol, KOH, methanol, $MgCl_2$, NaCl, n-pentanol, TCEP

Peptides were synthesized and HPLC-purified (free of trifluoroacetate) by ThermoFisher (Ulm, Germany) with carboxyl- and amino termini amidated and acetylated, respectively. His-tagged TEV-protease was obtained from the protein purification facility of the MPI-CBG Dresden, Dr. David Drechsel. All oligonucleotides were synthesized by Eurofins (Luxemburg).

Buffers and media. Table 2.2 lists all buffers and media commonly used in this work. All buffers were filtered through 0.22 μm filters before use.

Table 2.2: List of commonly used media and buffer

media	composition
Luria-Bertani (LB) medium	20 g/l tryptone, 5 g/l yeast extract, 5 g/l NaCl
LB-plates	15 g of agar-agar / liter LB-medium
SOC medium	20 g/l tryptone, 5 g/l yeast extract, 0.5 g/l NaCl, 0.186 g/l KCl. Add 10 mM $MgCl_2$, 10mM $MgSO_4$, and 0.4% w/v glucose sterile after autoclaving
2xYT medium	16 g/l tryptone, 10 g/l yeast extract, 5 g/l NaCl pH 7.0
antibiotics	antibiotics were used in the following concentrations: 100 μg/ml Ampicillin, 50 μg/ml Kanamycin, 50 μg/ml Chloramphenicol

buffers	
TNC2	40 mM Tris pH 8.0, 300 mM NaCl
TNC1	20 mM Tris pH 8.0, 150 mM NaCl
HKMSG	50 mM HEPES pH 7.4, 200 mM K_2SO_4, 5 mM $MgSO_4$, 20% w/v glycerol
HNMS	50 mM HEPES pH 7.4, 200 mM Na_2SO_4, 5 mM $MgSO_4$
10x TBE	89 mM Tris base, 89 mM boric acid pH 8.0, 2 mM Na-EDTA
6x DNA loading buffer	0.25% w/v Bromophenol Blue, 50% w/v glycerol in 0.5x TBE buffer

Table 2.2 continued

buffers	composition
10x SDS running buffer	250 mM Tris-base, 2 M glycine, 1% w/v SDS
SDS stacking gel buffer	0.5 M Tris-Cl pH 6.8, 0.4% w/v SDS
SDS running gel buffer	1.5 M Tris-Cl pH 8.8, 0.4% w/v SDS
5x SDS-PAGE loading buffer	50% v/v SDS stacking gel buffer (see above), 50% w/v glycerol, 10% w/v SDS, 7.7% w/v DTT, and 0.025% w/v Bromophenol Blue
Coomassie gel staining solution	0.06% w/v Coomassie Blue R250, 0.06% w/v Coomassie Blue G250, 45.4% v/v methanol, 9.2% v/v acetic acid
Coomassie gel destaining solution	45.4% v/v ethanol, 9.2% v/v acetic acid

Instruments. PH was measured with a pH 211 meter from HANNA instruments (Kehl am Rhein, Germany). Weighing was performed on a GENIUS microbalance or a AX 2202 balance (both from Sartorius). PCR was performed in the Mastercycler Personal from Eppendorf (Wesseling-Berzdorf, Germany). The agarose gel electrophoresis chamber was from Peqlab (Erlangen, Germany). Cells were cultivated in the SI-300R Lab Companion from Jeio Tech (Seoul, Korea) or the Innova 4230 from New Brunswick Scientific (Eppendorf) and handled in the Hera Safe sterile workbench from Thermo Fisher. Cell density was measured with the Ultrospec 1000 from Pharmacia Biotech (GE). Centrifugations were performed in a MiniSpin or a 5804 R centrifuge from Eppendorf or in the Evolution RC or WX Ultra 80 from Sorvall (Thermo Fisher). Cells were homogenized using an Ultra Turrax T-18 basic from IKA (Staufen, Germany) and lysed using a Microfluidizer M-110L from Microfluidics (Newton, USA) or a W-250 D Sonifier from Branson (Danbury, USA). Fast performance liquid chromatography was performed on an Äkta Avant system from GE. The electrophoresis system for SDS-PAGE was the Protean Mini from Bio-Rad. For sample incubation and shaking a Thermomixer Comfort from Eppendorf was used. Large unilamellar vesicles were extruded with the LiposoFast extruder from

Avestin (Ottawa, Canada) supplied with gastight syringes from Hamilton (Bonaduz, Switzerland).

UV-Vis spectroscopic determinations were performed with the NanoDrop 2000c from Nanodrop Technologies (Wilmington, USA) or the Lambda 35 spectrophotometer from Perkin Elmer (Waltham, USA). Circular dichroism (CD) spectra were recorded on a J-815 spectrometer from Jasco (Groß-Umstadt, Germany) in 1 mm x 1 cm Suprasil quartz glass cuvettes from Hellma (Müllheim, Germany). Static fluorescence spectra were recorded on a LS 55 luminescence spectrofluorometer from Perkin Elmer or on a Fluorolog 3 FL3-11 from HORIBA JY spectrofluorometer (Unterhaching, Germany) in 1 cm x 1 cm reduced volume Suprasil quartz glass cuvettes from Hellma. Time-resolved fluorescence spectra were recorded on a IBH 5000 U SPC instrument equipped with a IBH NanoLED-11 diode laser (375 nm peak wavelength, 90 ps FWHM, 1 MHz repetition rate) and a cooled Hamamatsu R3809U-50 microchannel plate photomultiplier (Hamamatsu, Shizuoka, Japan) with 30 ps time resolution and time setting between 7 and 14 ps per channel from HORIBA JY. Fourier transform infrared-spectroscopy was performed on a IFS/66v/S spectrometer from Bruker (Billericam, USA).

2.2. Molecular biology and protein biochemistry methods for *Lp*CopA

2.2.1. Molecular cloning and expression

Restriction enzyme cloning. The gene encoding for *Lp*CopA was synthesized by GeneArt (Life Technologies, Carlsbad, USA) with optimized codon usage for the expression in *E.coli* and cloned into the standard vector pET28a(+) from Novagen. In order to optimize the expression and purification of *Lp*CopA, the gene was also subcloned into the vectors pProExHTa, pBR-IBA1, and pET51b_mod. This was done using the restriction sites for the EcoRI and XhoI restriction enzymes. The restriction enzyme sites were introduced using the forward primer 5'-gtcgaattcatgaaacatgatcatcatcagg-3' and the reverse primer 5'-ttactcgagttacagggtcacacgtttcagacgcag-3'. The primer properties were analyzed

using the free web tool OligoCalc (http://simgene.com/OligoCalc) and met the standard quality criteria. For restriction enzyme cloning, the desired DNA fragment was amplified with the appropriate primers to introduce the restriction enzyme sites using the Phusion® High-Fidelity DNA Polymerase Kit according to the manual. The PCR product and a negative control sample from a PCR mixture lacking the template was analyzed on a 0.8% agarose gel according to [91]. The product band was cut out and DNA was eluted into 50 µl of double-distilled water. The vector and the insert were digested freshly with the restriction enzymes for 2 h at 37°C, then loaded again on an agarose gel, cut out, and eluted into double-distilled water. The fragments were ligated for 15 min at RT. The appropriate amount of insert m_{insert} was calculated as follows:

$$m_{insert} = \frac{m_{vector} \cdot 3 \cdot l_{insert}}{l_{vector}} \qquad (2.1)$$

with the masses m given in ng and the lengths l of the DNA strands given in kB. After chilling, 1–5 µl of the reaction were transformed into 50 µl competent Giga(DH5α) cells from Novagen. To this end, the plasmids were incubated 30 min with the competent cells on ice, heat shocked for 45 sec at 42°C and chilled for 2 min on ice. After growing for 1 h in SOC medium the cells were plated on LB-plates supplied with the appropriate antibiotics and incubated oN at 37°C. Five to six clones were chosen and cultivated in liquid culture in order to determine the success of cloning by an analytical digest of freshly prepared plasmid DNA. The plasmids from positive clones were transformed into the expression strain and the correct DNA sequence was verified by DNA sequencing. Competent cells were produced according to [92]. Table 2.3 shows an overview of the tags and protease sites introduced by cloning into the respective vectors.

Table 2.3: Overview of expression vectors for *Lp*CopA

vector	purification tag	protease site	name of construct
pProEXHTa Life Technologies (Carlsbad, USA)	N-term: 6-His tag	N-term: TEV	CopA_1N
pBR-IBA1 IBA (Göttingen, Germany)	N-term: 6-His tag C-term: Strep-tag II	N-term: TEV C-term: EK, 3c	CopA_Nhis_Cstrep
pET28a(+) Novagen	N-term: 6-His tag C-term: 6-His tag	N-term: thrombin	CopA_sg
pET51b_mod created by Ahmed Sayed	C-term: 10-His tag	C-term: 3c	CopA_C10His

Site-directed mutagenesis of the CPC motif. The mutation of selected cysteine residues to serine was accomplished with the QuikChange Lightning Multi Site-Directed Mutagenesis Kit from Agilent according to the manual. The DNA sequence was verified by sequencing. The mutagenesis primers (see Table 2.4) were designed with the help of the online tool provided by the kit manufacturer (http://www.genomics.agilent.com/primerDesignProgram.jsp).

Table 2.4: Overview of site-directed mutagenesis primers and *Lp*CopA mutants

substituted residues	primer	template	name of construct
C18S	5'-atagcggtaaaggtcatgcaag ccatcatgaacataatagccc-3'	CopA_1N	Mutation of the four cytoplasmic cysteines in one single PCR gives **cmCopA**
C42S	5'-aggtccgattgtttataccagc ccgatgcatccggaaatt-3'	CopA_1N	
C56SC59S	5'-gagcgcaccgggtcatagcccg ctgagcggtatggcactg-3'	CopA_1N	
C382S	5'-gcagttagcgttctgattattg caagcccgtgtgcactgg-3'	cmCopA	**cmC382S**
C384S	5'-tgatattgcatgtccgagcgca ctgggtctggcaac-3'	cmCopA	**cmC384S**
C382SC384S	5'-gattattgcaagcccgagcgca ctgggtctggcaa-3'	cmC382S	**cfCopA**

Recombinant expression of *Lp*CopA. Several expression strains (see Table 2.5) were tested for their suitability to express LpCopA and its mutants at sufficient yield and in a functional form. Moreover, for each strain different expression conditions (OD at induction, IPTG concentration, induction time, and cultivation temperature) were tested and the results were analysed using SDS-PAGE according to [93]. In the following, the general protocol is described and the conditions that were selected are mentioned.

Table 2.5: E. coli expression strains used in this work

strain	features
BL21(DE3)Gold Novagen	High-level protein expression of non-toxic protein using T7 RNA polymerase-based expression systems.
BL21(DE3)Rosetta Novagen	Designed to enhance the expression of eukaryotic proteins that contain codons rarely used in E. coli. Strain supplies tRNAs for the codons AUA, AGG, AGA, CUA, CCC, and GGA on a chloramphenicol resistant plasmid.
C43(DE3)pLysS Lucigen (Middleton, USA)	Effective in expressing toxic and membrane proteins from all classes of organisms. Contains at least one uncharacterized mutation that prevents cell death associated with expression of many toxic recombinant proteins. The chloramphenicol resistant pLysS plasmid encodes T7 phage lysozyme, an inhibitor for T7 polymerase which reduces expression from transformed T7 promoter containing plasmids when not induced.

All expression cultures were started from frozen glycerol stocks of *E.coli* cells transformed with the expression plasmid. *Lp*CopA was expressed in C43(DE3)pLysS cells and cmCopA and the mutants derived from it were expressed in BL21(DE3)Rosetta cells. In all cases, first 10 ml of preculture inoculated from the glycerol stock were grown oN at 37°C in 2xYT medium containing the appropriate antibiotics. The next day, four times 500 ml of prewarmed 2xYT medium containing antibiotics were inoculated 1:250 v/v with the preculture and cultured at 37°C with 150 rpm shaking in flasks with chicanes to an OD of 0.8 for *Lp*CopA and an OD of 1.0 for cmCopA and mutants. Protein expression was induced by adding IPTG to 0.1 mM for *Lp*CopA and 0.5 mM for cmCopA and the corresponding mutants. Cells were then cultivated at 18°C oN and cells were harvested by centrifugation (20 min, 3,000 g, 4°C), washed with

2xYT medium and with 2xYT medium containing 50% w/w glycerol, and stored at -20°C.

2.2.2. Cell breakage and solubilization of membranes

All purification steps were performed at 4°C or in ice. Typically 5 g of frozen cells were suspended in 50 ml buffer HKMSG supplied with 12 µg/ml DNase I, 5 mM β-ME and one protease inhibitor tablet per 100 ml of solution using the Ultra Turrax. The cells were disrupted by passing the solution 20 times at increasing pressure (6,000–18,000 psi) through the high pressure homogenizer. The total cell lysates were cleared by centrifugation (30 min, 18,000 g). Membrane proteins were solubilized from the supernatant by adding solid DDM to 0.63% w/v and gently mixing them for 20 to 30 min. Insoluble material was separated by centrifugation (40 min, 18,000g). Alternatively, the membranes were harvested from the total cell lysates by ultracentrifugation (60 min, 200,000 g) and the membrane pellet was resuspended thoroughly in buffer HKMSG including 5 mM β-ME and 1% DDM w/v, mixed gently for 30 min and insoluble material was separated as described above.

2.2.3. Protein purification

Different affinity-tagged constructs of *Lp*CopA were tested for affinity purification. First, a construct with an N-terminal 6His-tag (termed CopA_1N) was tested. Due to the identification of C-terminally truncated protein fragments by SDS-PAGE also C-terminally tagged constructs were tested: CopA_C10His with a C-terminal 10His-tag or CopA_Nhis_Cstrep with N-terminal 6His-tag and C-terminal Strep-tag II. This section describes the corresponding protocols. If not stated otherwise, all steps were performed at 4°C or on ice.

Purification of *Lp*CopA using the Strep-tag II. CopA_Nhis_Cstrep was purified using Strep-tag II affinity purification as follows: the solubilized protein was applied to the StrepTactin column equilibrated in 100 mM Tris-Cl pH 8.0 including 0.1% DDM and 5 mM β-ME. The column was washed with 5 CVs of equilibration buffer, then with 10 CVs of equilibration buffer including 20 mM Na-ATP, and again with 5 CVs of equilibration buffer. The protein was eluted

with the equilibration buffer containing 2.5 mM desthiobiotin in fractions of 1 ml. The column was regenerated afterwards by washing three times with 5 CVs of the equilibration buffer containing 1 mM 2-[4'-hydroxy-benzeneazo]benzoic acid.

Purification of *Lp*CopA using His-tags. The His-tagged constructs were purified as follows: the solubilized protein was brought to 50 mM imidazole and applied to a 1 ml HisTrap HP column equilibrated in buffer HKMSG including 0.25% DDM, 50 mM imidazole, and 5 mM β-ME using the Äkta Avant FPLC system. The column was washed with 15 CVs equilibration buffer and 5 CVs buffer HKMSG including 0.1% DDM, 50 mM imidazole, and 5 mM β-ME. *Lp*CopA was eluted in buffer HKMSG including 0.1% DDM, 500 mM imidazole, and 5 mM β-ME in fractions of 1 ml. Usually the first 2 ml were discarded as they were of minor purity. Imidazole was removed by exchanging the buffer to HKMSG including 0.1% DDM and 5 mM β-ME. The concentration was determined spectrophotometrically (see below) using a molar extinction coefficient of 65,890 $M^{-1}cm^{-1}$ and purity was analyzed by SDS-PAGE according to [93]. Usually 2–4 mg of protein at a concentration of 18–25 μM were obtained per preparation. The protein solutions were frozen in liquid nitrogen and stored at -70°C. Optionally the N-terminal 6His-tag was cleaved off using TEV-protease 1:100 w/w at 25°C for 1.5 h.

2.3.   Recombinant expression and purification of MSPs

In nanodiscs, the rim of a nano-scaled planar lipid bilayer is encircled by two molecules of an amphipathic α-helical membrane scaffolding protein (MSP). Here, the expression and purification of these proteins is described. Two versions of MSP are commonly used: MSP1D1, giving nanodiscs with 10 nm diameter, and the extended MSP1E3D1 containing repeats of helices 4, 5 and 6, giving nanodiscs with 12–13 nm diameter. The preparation of MSP1D1 and MSP1E3D1 follows essentially the same protocol. The expression plasmids for the MSPs were obtained from Addgene (MSP1D1: #20061, MSP1E3D1: #20066). The expression constructs feature an N-terminal 7His-tag followed by a TEV-protease cleavage site. For expression, BL21(DE3)Gold cells harboring the expression plasmid for the respective MSP were grown in 20 ml of 2xYT medium containing

kanamycin for 6–8 h at 37°C. From this pre-culture, fresh 2xYT medium containing kanamycin was inoculated 1:500 v/v and cells were grown oN at 37°C to an OD_{600} of approximately 2.5. Protein expression was induced with 0.3 mM IPTG. After shaking for 4 h at 28°C, cells were harvested by centrifugation (20 min, 3,000 g, 4°C), washed with 2xYT medium and stored at -20°C.

If not stated otherwise, all purification steps were performed at 4°C or on ice. In a typical protein preparation 10 g of cells were suspended at 0.1 g/ml in 25 mM phosphate buffer (pH 7.4) using the Ultra Turrax. Then Triton X-100 was added to 1%, DNase I to 12 µg/ml, and one protease inhibitor tablet per 100 ml of solution. Cell lysis was performed by passing the solution 20 times at increasing pressure (6,000–18,000 psi) through the high pressure homogenizer. The lysate was cleared by centrifugation (70 min, 15,000 g). The supernatant was brought to 25 mM imidazole and loaded onto a 5 ml HisTrap HP column equilibrated in buffer TNC2 including 25 mM imidazole. The column was washed with 5 CVs of buffer TNC2 including 1% Triton X-100, 5 CVs of buffer TNC2 including 50 mM Na-Cholate and 20 mM imidazole, and 5 CVs of buffer TNC2 including 50 mM imidazole. The protein was eluted in buffer TNC2 including 400 mM imidazole and immediately diluted with buffer TNC1 1:2 to prevent precipitation. Then the buffer was exchanged to TNC1 using PD10 columns. The 7His-tag of the MSP was cleaved off by incubating the protein solution with his-tagged TEV-protease at a ratio of 500:1 w/w for 20 h at RT. The sample was then loaded onto two 1 ml HisTrap HP columns connected in series in buffer TNC1 including 25 mM imidazole and recovered from the flow through and a 10 CVs wash with buffer TNC1 including 25 mM imidazole. The flow through and wash was concentrated using centrifugal filter devices (MWCO 10,000) and the buffer was exchanged to TNC1 on PD10 columns. The concentration of the tag-free MSP (denoted by the appendix "(-)") was determined spectrophotometrically using molar extinction coefficients of 18,540 $M^{-1}cm^{-1}$ for MSP1D1(-) and 26,930$M^{-1}cm^{-1}$ for MSP1E3D1(-) and purity was analyzed by SDS-PAGE.

2.4. Reconstitution of *Lp*CopA into nanodiscs and SEC

For the reconstitution of *Lp*CopA into nanodiscs the protein was thawed on ice and transferred to buffer HNMS containing 5 mM (0.25% w/v) DDM using PD10 columns. Also the MSP was thawed on ice. For the lipid–detergent suspension the lipids were vacuum dried from chloroform for 2 h in a glass vial and the lipid film was then resuspended in an aqueous solution of DDM and vortexed and sonicated in a water bath for 1 min alternately until a clear solution was obtained. In case of asolectin a mixture of 8 mM lipids in 12 mM DDM was used. For other lipids 8 mM DDM was used.

For the assembly of nanodiscs *Lp*CopA, MSP, and the lipid-detergent suspension were mixed in molar ratios of asolectin : MSP1D1(-) : *Lp*CopA 60:3:1 or asolectin : MSP1E3D1(-) : *Lp*CopA 200:5:1. Typically, the *Lp*CopA concentration was 3–8 μM in a total volume of 2 ml. After incubating the mixture on ice for 1 h, the detergent was removed by adding Bio-Beads equilibrated in buffer HNMS at a ratio of 1:1 v/v and incubating overhead-rotating at 4°C for 3 h. Then, Bio-Beads and aggregates were removed by centrifugation (15 min, 20,000 g). IMAC was used to separate *Lp*CopA-nanodiscs and empty nanodiscs. The nanodiscs solution was supplemented with 30 mM imidazole and processed with His SpinTrap columns according to the manual with the following modifications: the resin was incubated with the mixture for 10 min between loading steps and for 2 min between elution steps. In order to remove possible aggregates and to assess the quality of the preparation size-exclusion chromatography was performed on a Superdex200 10/300 GL column. The protein signal was monitored at 280 nm. The formation of nanodiscs with the correct mass ratio of *Lp*CopA and MSP was also verified by analysing the Coomassie stain density of SDS-PAGEs with ImageJ (http://rsb.info.nih.gov/ij/disclaimer.html). The concentration of *Lp*CopA-MSP1E3D1(-)-nanodiscs was estimated spectrophotometrically using a calculated molar extinction coefficient of 95,450 $M^{-1}cm^{-1}$ for a nanodiscs comprising one *Lp*CopA and two MSP1E3D1(-). Moreover, to test the general applicability of the protocol and of different lipids and detergents, empty nanodiscs were prepared

according to the protocol described above. In this case the final molar ratios of MSP to lipid were 1:110 for MSP1E3D1(-) and 1:70 for MSP1D1(-).

2.5. ATPase activity assay of *Lp*CopA

In order to assess the functionality of *Lp*CopA reconstituted in nanodiscs its ATP-hydrolytic activity upon activation with Cu^+ was studied. Hydrolyzed organic phosphate P_i was determined using the method described by Lanzetta et al. [94]. To this end, *Lp*CopA-nanodiscs at a concentration of 0.1 µM were transferred to the assay buffer (35 mM Na-HEPES pH 7.4, 10 mM KCl, 2.5 mM $MgCl_2$, 0.5 mM ß-ME) using PD10 columns and preincubated with different amounts of $CuSO_4$ for 5 min at 37°C. The reaction was started by adding Na-ATP to a final concentration of 2 mM. 100 µl aliquots were removed at $t = 0$ and $t = 30$ min and transferred to tubes containing 10 µl of 0.5 M Na-EDTA at pH 8.0 to stop the reaction. The released P_i in the samples was determined according to a standard curve of known concentrations of P_i and the hydrolytic activity per time and per *Lp*CopA was calculated.

2.6. Site specific-labeling of *Lp*CopA with BADAN

In order to monitor the intra-membrane protein polarity and hydration the thiol-reactive solvatochromic fluorescent probe BADAN (6-bromoacetyl-2-dimethylaminonaphthalene) was attached site-specifically to the cysteines in the copper-binding motif of cmCopA. To avoid background signal by unbound residual BADAN in the sample the labeling was performed during the purification on the IMAC column. The purification was performed as described in sections 2.2.2 and 2.2.3 with the modifications described below. β-ME was omitted in the whole protein preparation. After loading the solubilized protein on the IMAC column, the column was washed with 25 CVs of equilibration buffer and then flushed with 15 CVs BADAN in equilibration buffer at a flow rate of 0.3 ml/min. BADAN was rapidly diluted 1:1000 v/v immediately before use from a 15 mM stock in dimethylformamide into equilibration buffer. The column was then washed with 70 CVs of equilibration buffer and 20 CVs of buffer HKMSG including 0.15% w/v DDM and 50 mM imidazole. The removal of free BADAN

was monitored by following the BADAN absorption in the flow-through. The protein was eluted with a gradient from 50 to 500 mM imidazole over 12 CVs in fractions of 0.5 ml. The buffer was exchanged to HKMSG including 0.15% w/v DDM using PD10 columns. Label coupling efficiency (*CE*) and protein concentration were determined according to [95] using the equation:

$$CE = \frac{\varepsilon_{280}(Lp\text{CopA}) \cdot A_{382}}{(A_{280} - (CF_{280} \cdot A_{382})) \cdot \varepsilon_{382}(Lp\text{CopA})} \qquad (2.2)$$

with the extinction coefficients ε_{280} being 65,890 M^{-1}cm^{-1} and 21,000 M^{-1}cm^{-1} for *Lp*CopA and BADAN, respectively. The correction factor CF_{280} was determined as follows:

$$CF_{280} = \frac{A_{280} \text{ (BADAN)}}{A_{382} \text{ (BADAN)}}. \qquad (2.3)$$

2.7. Handling of hydrophobic peptides and preparation of lipid vesicles

The MBb peptide was dissolved in 20 mM Tris-SO$_4$ pH 7.5 and the concentration was determined spectrophotometrically using a molar extinction coefficient of 11,000 M^{-1}cm^{-1}. Large unilamellar vesicles (LUVs) were prepared by dissolving a vacuum-dried lipid film of POPC in the appropriate volume of buffer to obtain the desired lipid concentration. The suspension was vortexed for about 20 minutes and extruded through two track-etched polycarbonate membranes with sharply defined pore sizes of 100 nm with the help of an extruder. Extrusion was assumed to be successful, when the solution became opaque and the required pressure for extrusion significantly decreased.

2.8. Spectroscopic techniques

In this section the details of the spectroscopic techniques used throughout this work are described. For all spectra, corresponding baseline measurements of buffer and/or cuvettes were recorded and subtracted from the spectrum of the sample. If not stated otherwise, spectra were recorded at 20°C.

UV-Vis spectroscopy. UV-Vis spectroscopic measurements were performed either using the Nanodrop 2000c or the Lambda 35 spectrophotometer. For DNA

and protein concentration determinations, usually the Nanodrop 2000c was used due to its minimal sample consumption. The concentration c was calculated according to the Lambert-Beer law:

$$A_\lambda = \varepsilon_\lambda \cdot c \cdot d \tag{2.4}$$

with A_λ being the unitless wavelength-dependent absorption, ε_λ the wavelength-dependent molar extinction coefficient in $M^{-1}cm^{-1}$, and d the path length in cm. In the Lambda 35 spectrophotometer, the scan speed was 100 nm/min, the band width was 1 nm, and cuvettes with 1 cm path length were used. In the Nanodrop 2000c instrument these parameters are adjusted automatically.

Circular dichroism spectroscopy. Circular dichroism (CD) spectroscopy is a powerful technique to determine secondary of biological macromolecules. CD refers to the differential absorption of the left- and right-handed polarized component of plane polarized light by chiral chromophores. In the far-UV region, the spectrum of each secondary structure type (α-helix, β-sheet, turn, etc.) has a characteristic shape. Thus, the secondary structure of an unknown sample can be determined by deconvoluting its CD spectrum into the known reference spectra of the secondary structure types [96].

The far-UV CD spectra of *Lp*CopA and MSP were measured in quartz cuvettes with 1 mm path-length using the Jasco J-815 CD spectrometer from 260 to 190 or 197 nm. The scan speed was 100 nm/min, data integration time was 2 s, band width was 4 nm, and data pitch was 1 nm. Five to ten accumulations were averaged for each sample in order to reduce noise. Sensitivity and scanning mode were set to standard and continuous, respectively. The raw ellipticity θ was converted to mean residue ellipticity (MRE) according to

$$MRE = \frac{\theta}{n_{aa-1} \cdot c_M \cdot l \cdot 10^{-5}} \tag{2.5}$$

with n_{aa-1} being the number of peptide bonds of the protein, c_M the protein concentration in μM, and l the path length of the cuvette in cm. The number of amino acids is 766 for *Lp*CopA, 256 for MSP1E3D1(-) , and 190 for MSP1D1(-). Protein concentration was between 0.1 μM and 1 μM.

Fluorescence spectroscopy. Fluorescence spectroscopy detects changes in the physical environment as well as dynamic properties of biological macromolecules and requires only small sample concentrations [97]. It does not give direct structural information, but provides information on the physical environment of a specific site within a larger molecule. The data derived from fluorescence measurements can give detailed insights into the complexity of protein structure–function relationships when combined with the structure information gained from CD or IR spectroscopy. In this work fluorescence spectroscopy is used to observe lipid-interactions of an amphipathic peptide at the water–membrane interphase exploiting the intrinsic fluorescence of the amino acid tryptophan and to study intra-protein hydration using the site-specifically introduced fluorescent probe BADAN.

Steady-state fluorescence spectroscopy. Fluorescence emission spectra were recorded from 410 to 550 nm with excitation at 390 nm to detect BADAN fluorescence or from 310 to 550 nm with excitation at 280 nm to detect intrinsic tryptophan fluorescence. The band width in both the excitation and detection monochromators was set to 10 nm for BADAN and to 5 nm for tryptophan on the LS55 instrument. When using the Fluorolog 3 instrument the bandwidths were 2 nm. The scan speed was 100 nm/min and 850 to 900 V photomultiplier voltage was typically chosen. Protein concentration was between 0.1 µM and 1 µM.

The tryptophan fluorescence spectra were fitted with the help of non-linear least-square fitting to a log-normal distribution:

$$I_\lambda = I_0 + \frac{A}{\sqrt{2\pi} \cdot w \cdot \lambda} \cdot \exp\left(\frac{-ln^2\left(\frac{\lambda}{\lambda_c}\right)}{2 \cdot w^2}\right) \tag{2.6}$$

with I_λ being the wavelength-dependent fluorescence intensity, I_0 the offset, λ_c the mean, w the standard deviation, and A the area.

Time-resolved fluorescence spectroscopy. Time-resolved fluorescence spectroscopy was measured in collaboration with the group of Prof. Martin Hof of the Academy of Sciences of the Czech Republic, Prague. For a short introduction to the method see the corresponding section in 4.1. Emission decays were recorded at a series of wavelengths spanning the steady state emission spectrum in

5 nm steps with excitation at 375 nm. A cutoff filter at 399 nm was used in order to exclude scattered light. Bandwidths for both the excitation and emission monochromators were set to 32 nm. In order to eliminate anisotropy effects the spectra were recorded under the magic angle of 54.7°. Signal intensity was kept below 2% of the light source repetition rate (20,000 counts/sec). The raw data were fitted to multiexponentials using the iterative reconvolution procedure provided with the FluoFit software from PicoQuant. The time-resolved emission spectra (TRES) $S(\lambda,t)$ were obtained by the spectral reconstruction method as described in [98] and according to:

$$S(\lambda, t) = \frac{D(\lambda,t) \cdot S_0(\lambda)}{\int_0^\infty D(\lambda,t)\mathrm{d}t} \tag{2.7}$$

with $D(\lambda,t)$ being the fluorescence decays and S_0 the steady state emission spectra. The time zero spectrum was estimated according to [99]. The emission maxima $v(t)$ were obtained from the log-normal fitted TRES according to [100]. The correlation function $C(t)$ was calculated from $v(t)$ of the TRES at time t according to:

$$C(t) = \frac{v(t) - v(\infty)}{v(0) - v(\infty)} \tag{2.8}$$

In order to characterize the time scale of the solvent response, an integral relaxation time was calculated as follows:

$$\tau_r \equiv \int_0^\infty C(t)\mathrm{d}t \tag{2.9}$$

Fourier-transform infrared spectroscopy. Fourier-transform infrared spectra were recorded on an IFS/66v/S spectrometer in attenuated total reflection (ATR) mode on a diamond 9-reflections ATR unit. Approximately 11 µmole of the MBb peptide were dried carefully on the ATR crystal using a gentle stream of nitrogen. POPC liposomes were added at a molar ratio of 1:20 peptide to lipid with the same peptide concentration. Transmission spectra were recorded and processed using the OPUS software from Bruker.

3. Establishing an *in vitro* system to study *Lp*CopA in a membrane-mimetic environment

3.1. Introduction and overview

In 2011, CopA from *Legionella pneumophila* was the first heavy-metal transporting P-type ATPase for which a high resolution crystal structure became available [64]. This opened up the unique possibility to relate dynamic solution-state spectroscopic measurements in controllable lipidic environments to the static structural snapshots from crystallography.

Molecular biophysical, e.g. spectroscopic studies of a membrane protein require sufficient quantities of the protein in a pure and functional form and reconstituted in a native-like lipid environment. The recombinant production of *Lp*CopA (see Figure 3.1 for the amino acid sequence of the protein) comprises the following steps: the screening for a suitable recombinant production host, the selection of a purification tag, the detergent-mediated solubilization of the protein from the lipid membrane, the affinity purification, and the quality control of the protein in terms of homogeneity, structure, and function. Moreover, the structure and function of a membrane protein depends critically on the lipid environment. Thus, it is necessary to reconstitute the membrane protein of interest into an artificial membrane system that suits the requirements of the biophysical methods. Throughout this work, nanodiscs were used as a membrane mimetic system. They can be considered as a "soluble portion" of lipid bilayer in which a planar nano-scaled disc of lipid bilayer is encircled by a ring of two amphipathic membrane scaffolding proteins (MSPs). They can be prepared in a simple self-assembly process, provide a well-defined lipid environment, and are virtually scatter-free due to their small size, rendering them the ideal membrane mimetic system for solution spectroscopic techniques.

```
MKHDHHQGHT HSGKGHACHH EHNSPKTQQA SSKMEGPIVY TCPMHPEIRQ      50

SAPGHCPLCG MALEPETVTV SEVVSPEYLD MRRRFWIALM LTIPVVILEM     100

GGHGLKHFIS GNGSSWIQLL LATPVVLWGG WPFFKRGWQS LKTGQLNMFT     150

LIAMGIGVAW IYSMVAVLWP GVFPHAFRSQ EGVVAVYFEA AAVITTLVLL     200

GQVLELKARE QTGSAIRALL KLVPESAHRI KEDGSEEEVS LDNVAVGDLL     250

RVRPGEKIPV DGEVQEGRSF VDESMVTGEP IPVAKEASAK VIGATINQTG     300

SFVMKALHVG SDTMLARIVQ MVSDAQRSRA PIQRLADTVS GWFVPAVILV     350

AVLSFIVWAL LGPQPALSYG LIAAVSVLII ACPCALGLAT PMSIMVGVGK     400

GAQSGVLIKN AEALERMEKV NTLVVDKTGT LTEGHPKLTR IVTDDFVEDN     450

ALALAAALEH QSEHPLANAI VHAAKEKGLS LGSVEAFEAP TGKGVVGQVD     500

GHHVAIGNAR LMQEHGGDNA PLFEKADELR GKGASVMFMA VDGKTVALLV     550

VEDPIKSSTP ETILELQQSG IEIVMLTGDS KRTAEAVAGT LGIKKVVAEI     600

MPEDKSRIVS ELKDKGLIVA MAGDGVNDAP ALAKADIGIA MGTGTDVAIE     650

SAGVTLLHGD LRGIAKARRL SESTMSNIRQ NLFFAFIYNV LGVPLAAGVL     700

YPLTGLLLSP MIAAAMALS SVSVIINALR LKRVTL                    736
```

Figure 3.1: Amino acid sequence of *Lp*CopA. The cytosolic head piece of *Lp*CopA comprises the actuator (A), the phosphorylation (P), and the nucleotide-binding (N) domain, shown in yellow, purple, and magenta, respectively. The N-terminal heavy metal binding domain (HMBD, shown in cyan) is specific for the P_{IB}-subtype of P-ATPases, as well as the first two TM helices MA and MB (shown in dark cyan). The core TM helices are shown in light brown. The CPC copper binding motif on TM helix M4 is marked in red (C382) and blue (C384). The assignment of the domains is according to PDB 3RFU.

3.2. Results

3.2.1. Recombinant production of *Lp*CopA

Cloning of *Lp*CopA into the expression vectors. In order to test the expression vectors pProExHTa, pBR-IBA1, and pET51b_mod for overexpression and purification of *Lp*CopA, the gene was amplified from the pET28a(+) vector using the Phusion® High-Fidelity DNA Polymerase Kit and restriction sites for EcoRI and XhoI were introduced *via* the PCR primers (see section 2.2.1). Clearly, the PCR yielded the insert containing the *Lp*CopA gene as a single product (see Figure 3.2 A). PCR product and vector were digested with the restriction enzymes, ligated, and transformed into Giga cells. The successful insertion of the *Lp*CopA gene into the vector was verified by an analytic digest. Thereby, positive clones containing the insert could be unequivocally distinguished from negative clones (Figure 3.2 B). The agarose gel electrophoreses of the cloning of *Lp*CopA into pProExHTa are shown exemplarily. Cloning into the other vectors proceeded correspondingly with similar results.
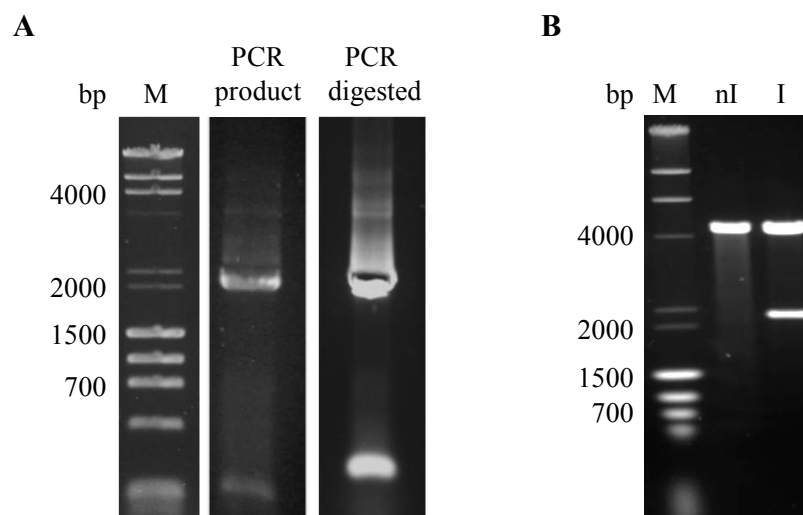

Figure 3.2: Agarose gel electrophoreses of the restriction enzyme cloning of *Lp*CopA into pProEXHTa. M: DNA size standard. (**A**) PCR product: The PCR product containing the *Lp*CopA gene (2229 bp). PCR digested: The PCR product was digested with EcoRI and XhoI and cut out from the gel (2217 bp). (**B**) Analytical digest of the *Lp*CopA gene cloned into pProEXHTa vector (copA_1N) with EcoRI and XhoI. The empty vector has 4686 bp. nI: negative clone without insert. I: positive clone with insert (2217 bp).

Recombinant expression of *Lp*CopA. Recombinant expression of prokaryotic proteins is usually performed in specially adapted strains of the Gram-negative intestinal bacterium *Escherichia coli*. However, the synthesis of membrane proteins can be a difficult task for the host due to toxicity effects. Membrane protein overexpression often results in improperly folded and non-functional proteins and at worst in the formation of inclusion bodies. Therefore, it is important to carefully select a suitable expression vector and expression strain for the target membrane protein and to optimize the cell growth conditions [101, 102].

The C43(DE3)pLysS strain was chosen for the expression of CopA_1N, as it gave the most promising results in preceding tests with various expression strains. In these tests, only CopA_1N, the pProExHTa-derived expression construct was used, because this vector had been used successfully for the purification of heavy metal transporters before [60]. The C43(DE3)pLysS strain is derived from the common BL21(DE3) strain, but is superior in expressing toxic and membrane proteins, as it features at least one uncharacterized mutation that prevents cell death associated with expression of toxic recombinant proteins. (Moreover, basal expression of T7 polymerase is suppressed as the cells harbour a plasmid expressing T7 phage lysozyme, a natural inhibitor of T7 polymerase. However, it has to be noted that pProExHTa does not feature a T7 promotor, and thus transcription is not T7 polymerase-dependent.) SDS-PAGE analysis of the protein expression shows that *Lp*CopA is strongly and completely expressed in C43(DE3)pLysS (see Figure 3.3). Furthermore, suitable growth and expression conditions were screened systematically. The aim was to decelerate the protein synthesis rate in order to reduce the stress exerted on the expression host, and consequently, to allow for the complete translation and correct folding of *Lp*CopA. Therefore, protein synthesis was induced at a relatively high OD (approximately 0.8), using the minimal IPTG concentration found to induce maximal protein expression (0.1 mM). Moreover, the cells were cultivated at 18°C. Taken together, *Lp*CopA could be expressed robustly in C43(DE3)pLysS at a low protein synthesis rate.
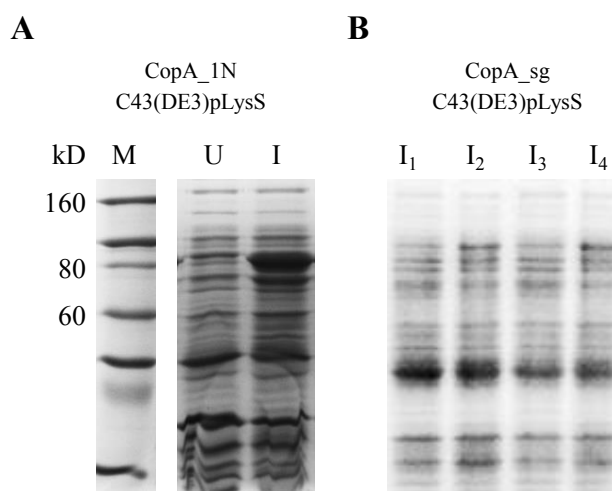
Figure 3.3: SDS-PAGE of *Lp*CopA overexpression in C43(DE3)pLysS. M: protein size standard. All cell extracts were loaded on the SDS-PAGE at a concentration of 1 mg/ml. (**A**) *Lp*CopA overexpressed from the pProExHTa derived expression construct CopA_1N. U: uninduced sample. I: protein expression was induced in the sample with 1 mM IPTG. No expression is observed in the uninduced sample, while strong expression is found for *Lp*CopA after induction. (**B**) Expression of *Lp*CopA from the pET28a(+) derived expression construct CopA_sg. I_1: induced with 0.5 mM IPTG for 3 h, I_2: induced with 0.5 mM IPTG oN, I_3: induced with 1 mM IPTG for 3 h, I_4: induced with 1 mM IPTG oN. In none of the samples, overexpression at the expected range of 80 kD could be detected.

Cell breakage and solubilization of *Lp*CopA. Unlike soluble proteins, integral membrane proteins cannot be readily purified from the aqueous cytoplasm after lysis of the expression host cells, but need to be solubilized from the host cell membrane using a suitable detergent. This process is often the most critical step in membrane protein purification, as too harsh detergent exposure may lead to the partial unfolding or degradation of the membrane protein and/or its inactivation. Therefore, it is crucial to choose the detergent and the solubilization carefully to balance between effective solubilization of the target protein and maintaining its integrity [103]. This section describes the results obtained for the mechanical lysis of the *E. coli* host cells and the tested solubilization protocols.

It is critical to prevent heating and frothing of the cell suspension during the cell lysis, as this may lead to protein denaturation and degradation. For the purification of *Lp*CopA this was achieved by cooling the suspension between the lysis cycles in the high pressure homogenizer on ice and supplying the solution with protease inhibitors. After removal of the cell debris by centrifugation, the cell

37

membrane fragments are usually collected from the cleared cell lysate by ultracentrifugation in order to separate the membrane fraction from cytoplasmic contaminations. However, this step is time-consuming and often leads to the loss of material.

Hence, it was tested if *Lp*CopA can also be solubilized directly from the cleared cell lysate without a quality bias. In the "classical" protocol, the membrane pellet was suspended after ultracentrifugation in the initial volume of buffer supplied with 1% DDM. In the direct solubilization protocol, DDM was directly added to the cleared cell lysate. In both cases solubilization was allowed to proceed for approximately 30 min before insoluble material was pelleted by centrifugation. In Figure 3.4 it can be seen that there was no obvious difference in purity after the IMAC (see section 2.2.3) between the two protocols. Thus, *Lp*CopA was routinely purified directly from the cleared cell lysate which shortened the purification protocol by half a day.
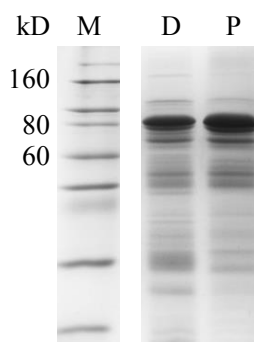
Figure 3.4: SDS-PAGE of purified *Lp*CopA solubilized with directly or from the cell membranes. M: protein size standard. D: *Lp*CopA was directly solubilized from the cleared cell lysate. P: cell membranes were harvested and *Lp*CopA was purified from the solubilized membrane pellet. No obvious difference in purity is observed. The samples were loaded on the SDS-PAGE at a concentration of 1 mg/ml.

3.2.2.   Purification of *Lp*CopA with C-terminal affinity tags

Another crucial factor for the success of a recombinant protein preparation is the selection of an appropriate expression vector that provides the target protein with an affinity tag that is suited to purify the protein in a functional form. Thus, the decision on the suitability of an expression construct can only be made after assessing the quality of the protein in terms of purity, homogeneity, structure, and

function. This section describes the attempts taken towards this aim. As mentioned in the preceding paragraph, pProExHTa was tested first. However, the appearance of contaminating bands at 70 and 50 kD on the SDS-PAGE (see Figure 3.6) that were assumed to be C-terminally truncated protein fragments, motivated me to test also vectors that provide C-terminal affinity tags, namely pET28a(+), pBR-IBA1, and pET51b_mod (see Table 2.3 for details of the vectors.) For the pET28a(+)-based expression construct CopA_sg no expression could be detected by SDS-PAGE (see Figure 3.3 B), even at high IPTG concentrations. For the expression constructs CopA_Nhis_Cstrep and CopA_C10His, based on the pBR-IBA1 and the pET51b_mod vector, respectively, successful expression at levels similar to CopA_1N was achieved using the protocol described above.

Purification and quality control of the C-terminally Strep-tagged construct. CopA_Nhis_Cstrep was purified after solubilization from the cleared cell lysate using the C-terminal Strep-tag II on a StrepTactin column. CopA_Nhis_Cstrep could be eluted at a relatively high purity, as can be determined from the SDS-PAGE (see Figure 3.5 A). However, a contaminating protein band at approximately 70 kD was observed. Since the purification tag was C-terminal, truncation or degradation could not account for this contamination. It is assumed that the band arose from DnaK, which is a member of the 70 kD heat shock protein family. DnaK is often found as a contaminant in recombinant protein production in connection with folding stress [104]. Since the chaperone action of DnaK and the interaction with the target protein is ATP-dependent, a washing step with ATP during the chromatographic purification can often help to unbind the DnaK from the protein [105]. In Figure 3.5 A it can be clearly seen that washing with ATP virtually abolishes the DnaK contamination. However, the protein yield per preparation was comparatively low with the CopA_Nhis_Cstrep construct. This, together with the indication of folding stress as judged by the contamination with DnaK, motivated testing the suitability of the CopA_C10His construct.

Purification and quality control of the C-terminally His-tagged construct. C-terminally His-tagged LpCopA could be eluted at high purity from the Ni-NTA HiTrap column (see Figure 3.5 B). Moreover, the protein yields were satisfactory.

Next the homogeneity of the prepared protein was studied by size exclusion chromatography. Unfortunately, a substantial fraction of the protein eluted at the exclusion volume of the Superdex200 10/300 GL column as aggregates as can be seen Figure 3.5 C. Thus, it may be concluded that a C-terminal tag might generally not be well suited for purifying *Lp*CopA in a functional form. This is conceivable, as the C-terminus of *Lp*CopA is located closely to the membrane interface at the end of a tightly folded TM helix, while the N-terminus is located in the flexible, cytoplasmic HMBD. Thus, an N-terminal tag would assumingly interfere less with protein folding and structure. Therefore, I focused on optimizing the purification conditions for the initially tested CopA_1N construct as will be described in the next section.
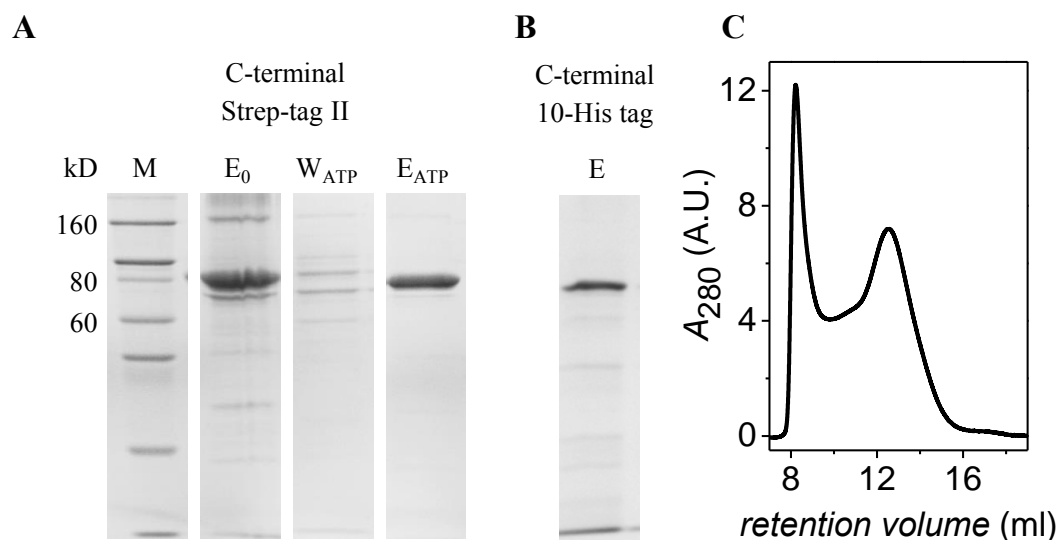

Figure 3.5: Purification of *Lp*CopA using C-terminal tags. (**A**) and (**B**) SDS-PAGEs. M: protein size standard. (**A**) *Lp*CopA purification using a C-terminal Strep-tag II from the CopA_Nhis_Cstrep construct. E_0: C-terminally Strep-tagged *Lp*CopA eluted from the StrepActin column without a prior ATP washing step. W_{ATP}: washing step with 5 CVs of 20 mM ATP. E_{ATP}: *Lp*CopA eluted from the StrepActin column after the ATP washing step. The contaminations can be clearly reduced by the ATP washing step. (**B**) *Lp*CopA purification using a C-terminal 10His-tag from the CopA_C10His construct. E: C-terminally His-tagged *Lp*CopA eluted from the HisTrap HP column. (**C**) Size exclusion chromatography of C-terminally His-tagged *Lp*CopA. The homogeneity of purified C10His-*Lp*CopA was analyzed on a Superdex200 10/300 GL column. A significant fraction of the protein elutes as aggregates at the column exclusion volume at ~8 ml.

3.2.3. Purification of *Lp*CopA with N-terminal His-tag

The N-terminally His-tagged CopA_1N is based on the pProExHTa vector. In this vector, the expression of *Lp*CopA is under the control of the relatively weak Trc-promotor. This promotor is a hybrid of the trp- and lacUV5-promotor that

allows for a gentle overexpression of the target gene [106, 107]. As mentioned above, the standard affinity purification of the CopA_1N construct usually resulted in the co-purification of putatively C-terminally truncated fragments of *Lp*CopA. A major fragment with a size of 70 kD was identified.

Analytical cleavage of N-terminally His-tagged CopA. In order to verify that the observed contaminants are indeed degradation products of *Lp*CopA, an analytical cleavage of the N-terminal His-tag using TEV-protease was performed. In Figure 3.6 it can be seen that the protein bands corresponding to full-length protein and the bands corresponding to the contamination shifted by the same amount on the SDS-PAGE after cleavage. This substantiates the assumption that the observed contaminants are *Lp*CopA fragments. Thus, it was necessary to optimize the purification protocol of CopA_1N in order to minimize the degradation of *Lp*CopA during the preparation.
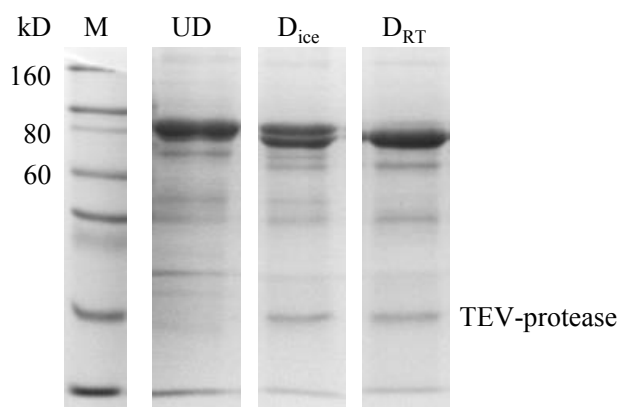
Figure 3.6: SDS-PAGE of analytical cleavage of the N-terminal His-tag of CopA_1N. M: protein size standard. UD: purified undigested CopA_1N. D_{ice}: CopA_1N incubated 1:100 w/w with TEV-protease on ice for 3 h. The His-tag was partially cleaved. D_{RT}: CopA_1N was incubated 1:100 w/w with TEV-protease at RT for 1.5 h. The His-tag was completely cleaved.

Generally, continuous cooling, quick purification, and the choice of a buffer, that optimally stabilizes the protein, helps to minimize degradation. These measures were also applied in the purification of CopA_1N. Since a lengthy membrane-harvesting step was omitted and the protein was directly solubilized from the cleared cell lysate as described above it was possible to perform the whole protein preparation in one day. A buffer with high sulfate content was chosen to stabilize

the protein in the E2-P$_i$ state [108]. Since the crystal structure of *Lp*CopA was also obtained in this state of the enzymatic cycle, it was assumed that the protein would be in a preferentially stable sub-conformation in this state. Moreover, it was observed that the first elution fractions were usually less pure than the late elution fractions (see Figure 3.7). By separately pooling the early and late fractions it was possible to obtain 3–7 mg of approximately 90% pure protein per liter of culture medium.
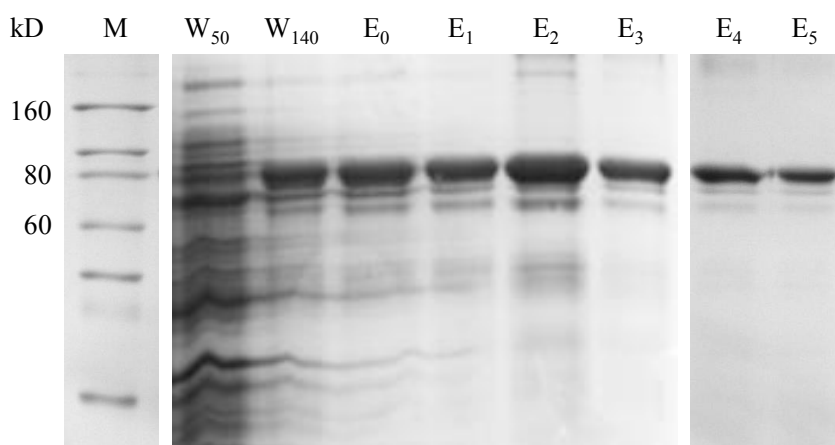

Figure 3.7: SDS-PAGE of the purification of N-terminally His-tagged *Lp*CopA. M: protein size standard. W$_{50}$: 10 column volume washing step with 50 mM imidazole . W$_{140}$: two column volume washing step with 140 mM imidazole. E$_0$ to E$_5$: elution fractions at 400 mM imidazole. Each fraction is 1 ml (equals 1 CV). E$_0$ represents the dead volume of the tubing. According to pixel intensity analysis of the Coomassie stain using ImageJ, the purity of fractions E$_1$ and E$_5$ is 73% and 95%, respectively.

Size exclusion chromatography of N-terminally His-tagged CopA. Possible aggregation of CopA_1N was studied by size exclusion chromatography (SEC, see Figure 3.8 A . Only a minor fraction of aggregates eluting at the exclusion volume of 8 ml was observed. The major protein peak was found at approximately 12.2 ml. As the size of the protein-detergent micelle is not known in the first place and has not been determined within the scope of this work, it was not possible to unambiguously assess if CopA_1N was monomeric. However, a first approximation can be made by adding up the molecular weight of CopA_1N (82 kD) and the weight of the DDM micelle (72 kD according to [109]) to 154 kD. According to the calibration of the Superdex200 10/300 GL column using soluble globular protein size standards, this would refer to an elution

volume of approximately 12.8 ml. Thus, given the described unknowns parameters, the non-globular shape, and the loose packing of CopA_1N as described in the next section, the observed elution volume of 12.2 ml is well in line with the assumption of monomeric CopA_1N.

Secondary structure determination of N-terminally His-tagged CopA. Next, it was studied if the secondary structure of CopA_1N corresponds to the crystal structure of *Lp*CopA. To this end, the secondary structure of *Lp*CopA was extracted from the PDB files of the crystal structure using the DSSP method (http://2struc.cryst.bbk.ac.uk). In the crystal structure of *Lp*CopA (PDB 3RFU9) the HMBD was not resolved and, thus, the corresponding coordinates are missing. Therefore the data were complemented with the coordinates of the third HMBD of ATP7A (PDB 2GA7). Using this approach, secondary structure values for *Lp*CopA of 49% α-helix, 14% β-sheet, and 37% others were extracted. Deconvolution of the circular dichroism spectrum of CopA_1N in DDM-micelles (see Figure 3.8 B) using the CDSSTR method (http://dichroweb.cryst.bbk.ac.uk/html/home.shtml) estimates the secondary structure as 46% α-helix, 13% β-sheet, and 41% others, which is in very good agreement with the crystal structure. Thus, it could be concluded that CopA_1N was correctly folded.

Taken together, purifying *Lp*CopA with an N-terminal His-tag resulted in satisfying yields of homogeneous, correctly folded protein. Protein degradation could be kept within acceptable limits by quick purification. Thus, the N-terminally His-tagged construct CopA_1N was used throughout this work. In the following CopA_1N will only be denoted as *Lp*CopA.

A

B
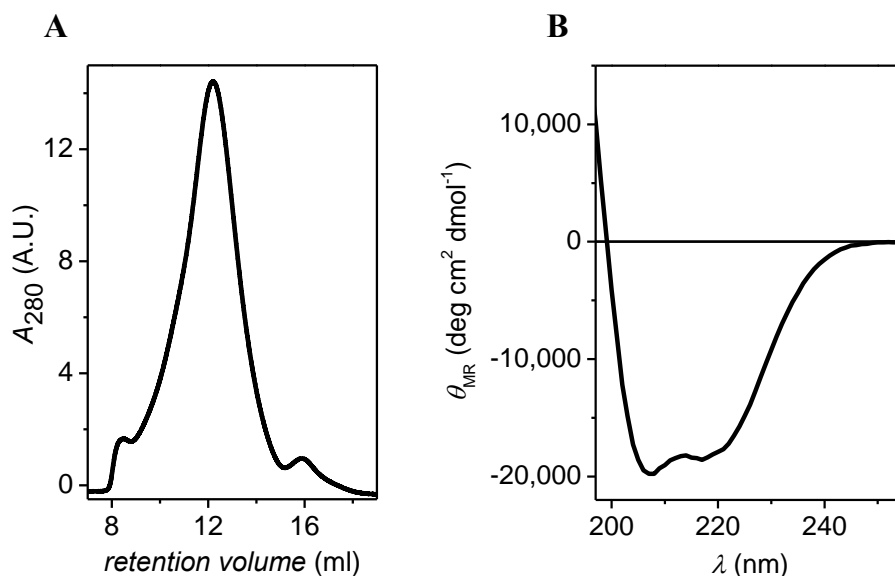
Figure 3.8: Quality controls for N-terminally His-tagged *Lp*CopA. (**A**) Size exclusion chromatography of purified CopA_1N on a Superdex200 10/300 GL column. Only one major protein peak at approximately 12.2 ml was observed. (**B**) Circular dichroism spectrum of CopA_1N measured in 0.15% DDM. Using the CDSSTR method the secondary structure fractions were estimated to be 46% α-helix, 13% β-sheet, and 41% others.

3.2.4. Reconstitution of *Lp*CopA into nanodiscs

The aim of this thesis was to study the influence of the lipid bilayer on intra-protein hydration of *Lp*CopA. Thus, a central aspect of this work was to reconstitute the functional protein into an artificial membrane system that mimics the cell membrane to the best extent possible and at the same time fulfills the experimental requirements. A relatively new membrane mimetic system that has proven its merits over the last years are the so-called nanodiscs [26, 110-113]. In nanodiscs, a small portion of planar bilayer is encircled by a homodimer of amphipathic α-helical membrane scaffolding proteins (MSPs) which are derived from the human apolipoprotein ApoA1. Thereby the hydrophobic hydrocarbon region of the lipids is shielded against the aqueous environment. In this way, very stable, soluble, and scatter-free particles with a diameter of 10 to 13 nm are created, which incorporate the target membrane protein as a single molecule with accessibility from both leaflets of the membrane. Nanodiscs can be produced using a well-controllable self-assembly process that can furthermore be adapted to meet the requirements of the membrane protein. In this section the recombinant

expression and purification of the MSPs and the development of the reconstitution protocol of *Lp*CopA into nanodiscs is described.

Purification of membrane scaffolding proteins. Two variants of MSPs are commonly used for the reconstitution of membrane proteins into nanodiscs. Both feature repeated amphipathic α-helices that are broken by prolin residues. Two molecules of the "standard" MSP1D1 with 10 consecutive α-helices form nanodiscs with approximately 10 nm diameter by aligning in an antiparallel fashion around the lipid patch. In the extended MSP1E3D1, the stretch comprising the helices 4, 5, and 6 is repeated which results in the formation of slightly bigger nanodiscs with approximately 13 nm diameter. See Table 3.1 for an overview of the protein sequences. Both MSPs were tested in this work and produced using the same protocol. The proteins were recombinantly expressed in *E. coli* and purified using a single step immobilized metal affinity (IMAC) purification.

Table 3.1: Overview of the sequence and characteristic of the MSPs

| protein	modular scheme	MW (kD)	diameter of nanodisc (nm)
Apo AI	GLOB-H1-H2-H3-H4-H5-H6-H7-H8-H9-H10	28	variable
MSP1D1	His-Tev-H0.5 -H2-H3-H4-H5-H6-H7-H8-H9-H10	25	10 nm
MSP1E3D1	His-Tev-H0.5-H2-H3-H4-H5-H6-H4-H5-H6-H7-H8-H9-H10	33	13 nm

As the MSPs naturally interact with the host lipid membrane, it was necessary to remove bound lipids by extensive washes with different detergents while the protein was bound to the Ni-NTA resin. By this means, a pure and reproducible preparation of MSP was obtained. To allow for the separation 6His-*Lp*CopA-nanodiscs and empty nanodiscs after reconstitution, the N-terminal 7His-tag was removed from the MSP. This was achieved by incubating the purified protein with His-tagged TEV-protease. The tag-free MSP, called MSP(-) was subsequently collected by reverse IMAC. Figure 3.9 A and B show that the MSPs can be purified to high purity and that the His-tag can be removed completely *via* enzymatic cleavage. Using the optimized expression and purification protocol, up

to 40 mg of MSP1D1(-) or MSP1E3D1(-) per 2 liter of bacterial liquid culture were obtained.

Preparation of empty nanodiscs. First, empty nanodiscs were prepared. This served as a proof of principle of the applicability of the method and allowed optimizing the lipid-MSP ratios. Moreover, different lipids and lipid mixtures as well as detergents were tested and the time and rate of detergent removal was optimized. The most homogeneous preparations were obtained with a molar lipid-MSP ratio of 1:70 for MSP1D1(-) and of 1:110 for MSP1E3D1(-). In case of the natural soy bean lipid extract asolectin a mean molecular weight of 750 g/mol was assumed. Larger ratios led to the formation of lipid aggregates as judged by the accumulation of precipitates after centrifugation of the nanodisc preparation. The most common detergent used in the preparation of nanodiscs is sodium cholate. This bile acid salt is known to readily dissolve lipid bilayers and to be easily removable due to its high CMC of 9 to 14 mM. However, sodium cholate is also known to have a denaturing effect on proteins [21]. Therefore, it was preferable to substitute cholate by a milder detergent, ideally by DDM, as this was used in the purification of *Lp*CopA anyway. Because of its long hydrocarbon tail, DDM is a mild detergent with very low CMC (0.17 mM) and does usually not denature membrane proteins. However, it is much slower at solubilizing lipid vesicles, which is a prerequisite for nanodisc preparation. Thus, the solubilization of lipid films by DDM was tested. Pure model lipids like POPC or DMPC were readily solubilized by resuspending the dried lipid film to 8 mM lipid concentration in 8 mM DDM at a temperature above the lipid phase transition temperature. Only in case of the natural soy bean lipid extract asolectin it was necessary to increase the DDM concentration to 12 mM and to sonicate and vortex the lipid-detergent suspension alternately up to 10 times.

Nanodiscs were then formed from the lipid-detergent suspension by removing the detergent with Bio-Beads SM-2. These are nonpolar polystyrene beads with a large surface area that selectively adsorb detergents from aqueous solution. For the formation of homogeneous nanodisc particles, it is important to remove the detergent completely and at a rate that allows for the partitioning and equilibration of the components between the solubilized micellar state and the

protein-bounded bilayer state. This rate can be controlled by the amount of added
Bio-Beads and the incubation time. The most homogeneous particles were
obtained at a Bio-Bead–DDM ratio of approximately 170:1 w/w and 3 h
incubation time. Figure 3.9 C shows the size exclusion chromatograms of
nanodiscs prepared from MSP1D1 and from MSP1E3D1 using DMPC.
MSP1D1(-)-nanodiscs elute at a retention volume of 13.0 ml corresponding to a
molecular weight of 144 kD according to globular protein molecular weight
standards. This agrees very well with the calculated molecular weight of 128 kD
of a nanodiscs consisting of 140 molecules of DMPC with MW = 0.678 kD and
two molecules MSP1D1(-) with MW = 22 kD. MSP1E3D1(-)-nanodiscs elute at a
retention volume of 12.2 ml corresponding to a molecular weight of 220 kD,
which is also well in line with the calculated value of 236 kD, comprising
260 DMPC molecules and two MSP1E3D1(-) molecules with MW = 30 kD.
Similar results were also obtained for POPC, DOPG, POPC:DOPG 3:1, *E. coli*
total lipid extract, and asolectin.
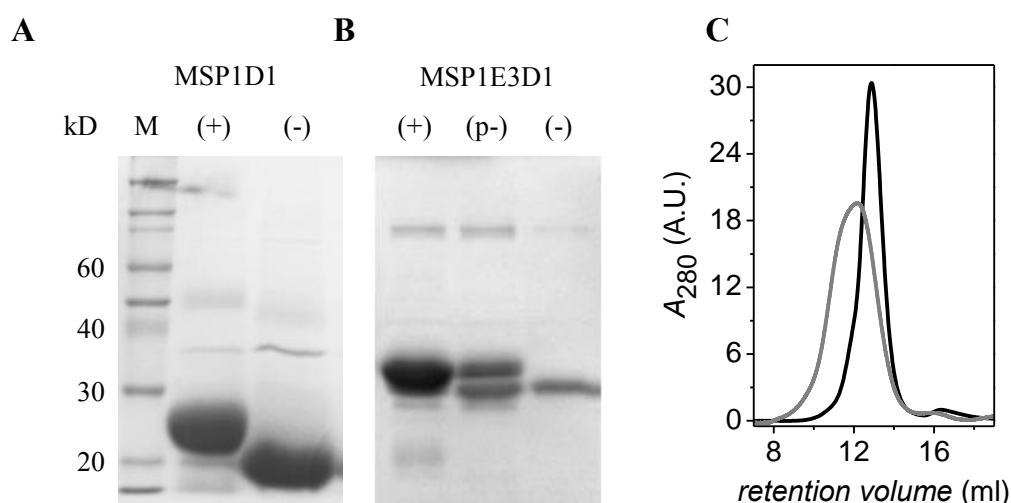
Figure 3.9: MSP purification and formation of empty nanodiscs.(A) and (B) SDS-PAGEs of
purified MSP before (+) and after (-) cleavage of the 7His-tag with TEV-protease. M: protein size
standard. (**A**) Purified MSP1D1. (**B**) Purified MSP1E3D1. Here additionally partial (p-) cleavage
of the 7His-tag is shown. (**C**) Size exclusion chromatography of empty DMPC-nanodiscs.
MSP1D1-nanodiscs (black line) elute at retention volume of 13.0 ml from the Superdex200
10/300 GL column, corresponding to a MW of 144 kD. MSP1E3D1-nanodiscs (gray line) elute at
retention volume of 12.2 ml corresponding to a MW of 220 kD.

Secondary structure and stability of MSP. The correct folding of the MSPs was
analyzed by CD spectroscopy. Figure 3.10 shows exemplarily the CD spectra of

MSP1D1(-) in aqueous phosphate buffer and in POPC-nanodiscs. The protein is clearly α-helical in both cases, with a slightly increased helicity for the reconstituted MSP. In order to test the stability of the nanodiscs, the thermal unfolding of MSP1D1(-) was analyzed by monitoring the ellipticity θ at 222 nm, which is commonly used as a measure for the helicity [114, 115]. Remarkably, the protein structure is much more stable in the nanodiscs: While pure MSP1D1(-) exhibits a moderately sigmoidal unfolding curve characteristic of a cooperative two-state unfolding event with a unfolding temperature T_m of approximately 55°C, the unfolding of MSP1D1(-) in the nanodiscs is characterized by a featureless shallow decrease in ellipticity with no clear turning point (see Figure 3.10 insert). This shows the high stability of the protein-lipid nanodiscs.

In summary, it was possible to prepare highly homogeneous nanodiscs with either MSP1D1(-) or the extended MSP1E3D1(-) using exclusively DDM and a variety of lipids and lipid mixtures.
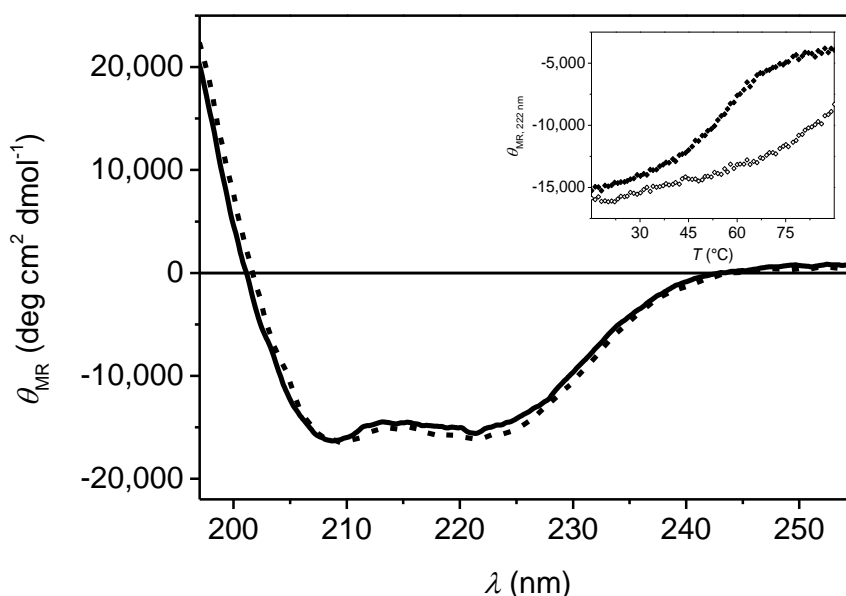
Figure 3.10: Circular dichroism spectrum of MSP1D1(-). The circular dichroism spectrum of MSP1D1(-) was measured in phosphate buffer (solid line) and POPC nanodiscs (dashed line). In both cases MSP1D1(-) is purely α-helical. *Insert:* Thermal unfolding of MSP1D1(-) in phosphate buffer (filled diamonds) and in POPC nanodiscs (open diamonds) monitored *via* the ellipticity at 222 nm. In the nanodiscs the thermal stability of MSP1D1(-) is significantly increased.

Reconstitution of *Lp*CopA into nanodiscs. Initially it was attempted to reconstitute *Lp*CopA using the "standard" MSP1D1 as a scaffolding protein. However, these experiments were not successful since they led to the formation of *Lp*CopA aggregates and empty nanodiscs as judged from the size exclusion chromatogram. This shows several overlapping peaks of high molecular weight species between 8 and 13 ml retention volume and a prominent peak at 14 ml (see Figure 3.11). No significant peak was observed at the expected retention volume around 12.5 ml, which would correspond to a molecular weight of around 190 kD. Also changing the ratio of *Lp*CopA, MSP1D1(-), and lipid did not improve the homogeneity of the preparation. This observation was somewhat puzzling, as other membrane proteins bearing seven or eight TM helices had been successfully reconstituted into MSP1D1-nanodiscs before [111, 116]. Moreover, the hydrodynamic radius of the native *Lp*CopA homologue from the thermophilic *Archaeoglobus fulgidus* was determined to be 6 nm using quasi elastic light scattering [117]. Furthermore, the longest cross section of the TM stalk as extracted from the crystal structure is only 4.5 nm. Thus, also the reconstitution of *Lp*CopA into MSP1D1-nanodiscs was expected to be feasible. However, the fact that it was not possible to reconstitute *Lp*CopA into the smaller nanodiscs could indicate that the protein is not as tightly packed as other membrane proteins in the flexible environment of the detergent micelle.
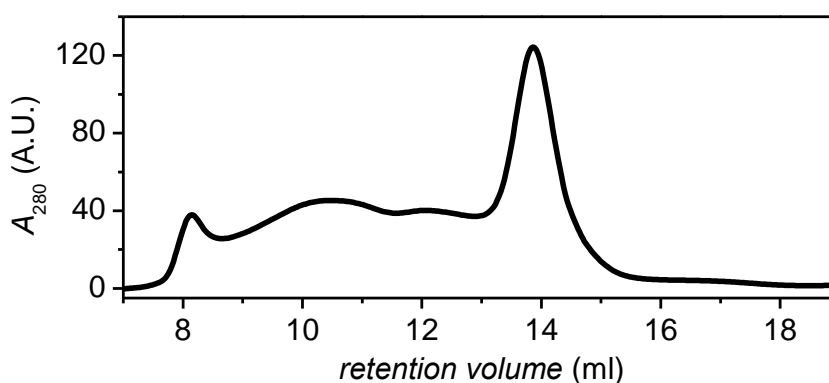

Figure 3.11: Size exclusion chromatogram of *Lp*CopA reconstitution into MSP1D1(-)-nanodiscs. The approach to reconstitute *Lp*CopA into nanodiscs encircled by MSP1D1(-) resulted in an inhomogeneous elution from the Superdex200 10/300 GL column. Several overlapping peaks of high molecular weight species between 8 and 13 ml retention volume and a prominent peak at 14 ml are observed.

Due to the results described above, the extended scaffolding protein MSP1E3D1(-) was tested for the reconstitution of *Lp*CopA. MSP1E3D1(-) is used in excess in the preparation to ensure complete reconstitution of *Lp*CopA. Thus, a mixture of *Lp*CopA-nanodiscs and empty nanodiscs is obtained, which can be separated by IMAC *via* the His-tag of *Lp*CopA (see Figure 3.12 A). The eluate contains the *Lp*CopA-nanodiscs while empty nanodiscs are expected in the flow through and wash fractions. In order to analyze the homogeneity, size-exclusion chromatography was performed. As can be seen in Figure 3.12 B *Lp*CopA-MSP1E3D1(-)-nanodiscs eluted at a retention volume of 11.8 ml from the Superdex200 10/300 GL column, corresponding to the expected weight of approximately 250 kD of a nanodisc composed of one *Lp*CopA, two MSP1E3D1(-), and 140 phospholipid molecules. Only a minor aggregate fraction eluting at the exclusion volume of the column was obtained. The size exclusion chromatography of the flow through of the IMAC contains one fraction eluting at 8 ml which contains presumably aggregated *Lp*CopA and a second fraction at 13.5 ml containing presumably empty nanodiscs with a low lipid : MSP1E3D1(-)-ratio. The mass fractions of MSP1E3D1(-) and *Lp*CopA in the *Lp*CopA-nanodiscs before as well as after the size exclusion chromatography are approximately 1:1 as estimated from the pixel intensity analysis of the Coomassie stain using the software ImageJ (http://imagej.nih.gov/ij/). This also corresponds to one *Lp*CopA per nanodisc.

The finding that it was only possible to reconstitute *Lp*CopA into the larger MSP1E3D1(-) particles substantiates the hypothesis that the flexible TM domain of detergent-solubilized *Lp*CopA requires probably more lateral area as provided in the MSP1E3D1-nanodisc with its 13 nm diameter. Taken together, a very homogeneous preparation of *Lp*CopA-nanodisc using the extended MSP1E3D1 scaffolding protein could be obtained.

A

B
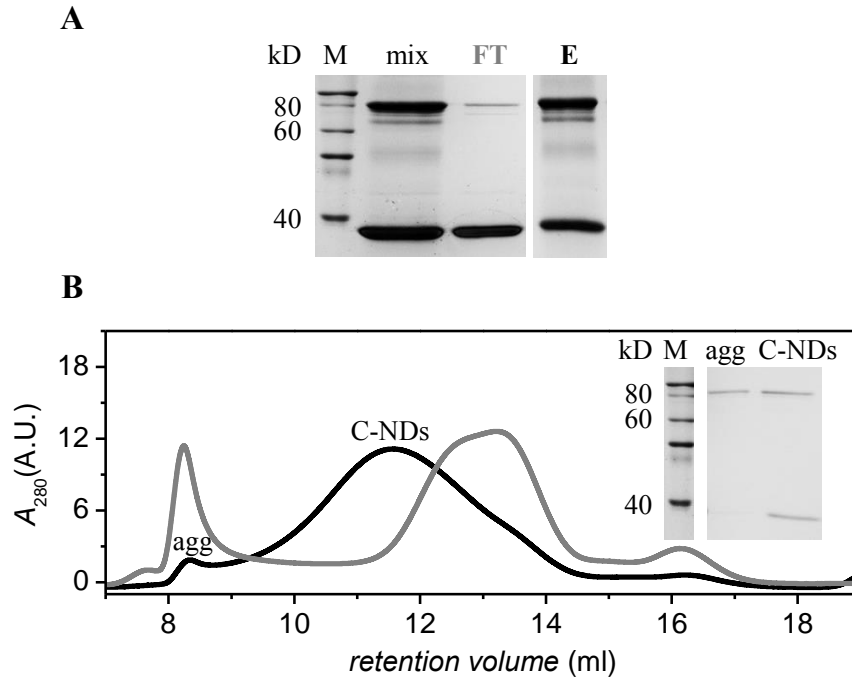
Figure 3.12: Reconstitution of *Lp*CopA into MSP1E3D1(-)-nanodiscs. (**A**) SDS-PAGE of the
IMAC. M: protein size standard. mix: mixture of *Lp*CopA and MSP1E3D1 before reconstitution.
After detergent removal, the mixture was subject to IMAC in order to separate empty and
*Lp*CopA-nanodiscs. FT: flow through of IMAC containing mostly empty nanodiscs. E: eluate of
IMAC containing mostly *Lp*CopA-nanodiscs. (**B**) Flow through and eluate of the IMAC were
analyzed on a Superdex200 10/300 GL size exclusion column. The flow through (gray line) of the
IMAC showed two major peaks in the size exclusion chromatogram: the peak at the exclusion
volume of 8 ml corresponds putatively to aggregated CopA and the peak at 13.5 ml corresponds to
lipid-poor nanodiscs. The eluate of the IMAC showed one major peak at 11.8 ml corresponding to
CopA-nanodiscs (C-NDs, see also in inserted SDS-PAGE) and a minor aggregated fraction
at 8 ml (agg, see insert).

3.2.5. ATPase activity of *Lp*CopA

Finally, it was tested whether the nanodisc-reconstituted *Lp*CopA was functional.
To this end, the ATP-hydrolytic activity of *Lp*CopA in nanodiscs upon stimulation
by Cu^+ was tested. The freshly prepared *Lp*CopA-nanodiscs were transferred to
the assay buffer. Thereby, the sulfate, which had stabilized the protein in the
$E2.P_i$ state throughout the purification and reconstitution was substituted by
chloride. After a pre-incubation with Cu^+, ATP was added and the reaction was
allowed to proceed for 30 min at 37°C. The amount of released inorganic
phosphate P_i was determined using the well-established colorimetric Lanzetta
assay [94] and compared with a standard curve prepared with KH_2PO_4. The
ATP-hydrolytic activity was activated 3-fold in the presence of 50 µM Cu^+. A
higher Cu^+-concentration of 100 µM inhibited activity again (see Figure 3.13).

It has to be noted, that a relatively high unspecific activity was found in the absence of added copper. ATP self-hydrolysis was ruled out as a possible cause by running appropriate controls. Possibly, the "basal" activity of LpCopA in the nominal absence of copper results from the contamination of the asolectin lipids with small amounts of copper. An estimation of the copper content using inductively-coupled-plasma mass spectrometry revealed a copper contamination of the asolectin of approximately 1.3% w/w. This would result in approximately 0.2 µM copper in the final LpCopA-nanodisc sample. Although this value is much smaller than the 50 µM copper found to maximally activate LpCopA, it is still conceivable, that this small amount of copper might contribute to the ATP hydrolysis in the absence of added copper. The affinity of LpCopA for Cu^+ is known to be in the femtomolar range [82]. Thus, very low concentrations of copper could already stimulate the ATPase. Moreover, it has to be noted, that the amount of available Cu^+ is likely to differ substantially from the amount of added Cu^+, as the copper ion is readily complexed by buffer substances [118] . The observed maximal activity of 15 nmole P_i / mg of protein / min is well in the range of published values of P_{IB}-ATPase activity [64, 68, 119]. Taken together, it could be shown that LpCopA could be reconstituted into MSP1E3D1(-)-nanodiscs in a functional form.
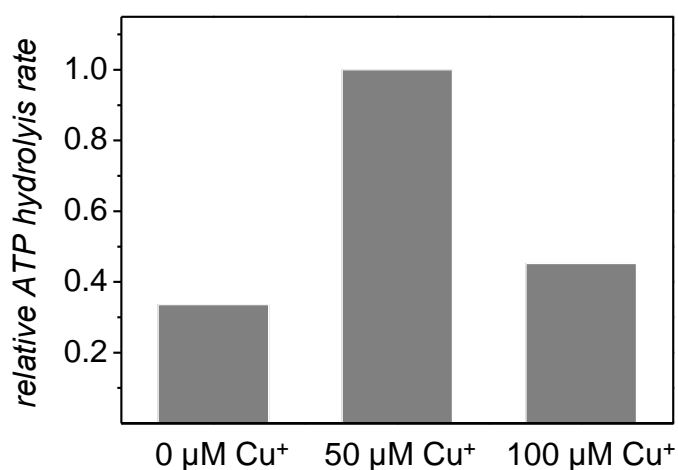

Figure 3.13: ATP hydrolytic activity of LpCopA reconstituted into nanodiscs. Activation of LpCopA reconstituted into MSP1E3D1(-)-nanodiscs by addition of different amounts of Cu^+. The maximal activity was 15 nmole P_i / mg of protein / min. LpCopA and ATP concentrations were 0.1 µM and 2 mM, respectively. ATP hydrolysis was measured for 30 min at 37°C.

3.3. Summary and discussion

*Lp*CopA from *Legionella pneumophila* was the first copper-transporting P_{IB}-type ATPase for which a high resolution crystal structure became available [64]. This provided the unique opportunity to relate the three-dimensional static crystallographic structures to site-specific information of the functional protein in the context of a lipid bilayer in order to achieve a deeper insight into the ion transport mechanism of this protein. This chapter described the establishment of an *in vitro* system allowing the biophysical study of the *Lp*CopA transport mechanism, which will be the focus of the following chapter. *Lp*CopA was recombinant expressed in *E. coli* and affinity-purified using an N-terminal 6His-tag after solubilization with DDM directly from the cleared cell lysate. Size exclusion chromatography prove that the protein was obtained in a homogeneous and monomeric form and the correct folding was confirmed by CD spectroscopic analysis. In order to study the influence of the lipid membrane, *Lp*CopA had to be reconstituted in an artificial bilayer system. Nanodiscs were chosen, as they can be easily assembled and provide a planar bilayer of controllable composition. Moreover, they are virtually scatter-free which qualifies them especially for optic spectroscopies, as will be shown in the next chapter. *Lp*CopA was successfully reconstituted into nanodiscs prepared with the extended membrane scaffolding protein MSP1E3D1 and showed a Cu^+-stimulated ATPase activity. To my knowledge the reconstitution of *Lp*CopA into nanodiscs described here constitutes the first successful nanodisc-reconstitution of a P_{IB}-type ATPase reported so far. An illustration of *Lp*CopA embedded into a nanodisc is shown in Figure 3.14. A robust and reproducible *in vitro* system was established that allows the detailed investigation of the ion transport mechanism and the role of the lipid membrane for the structure and function of the protein.
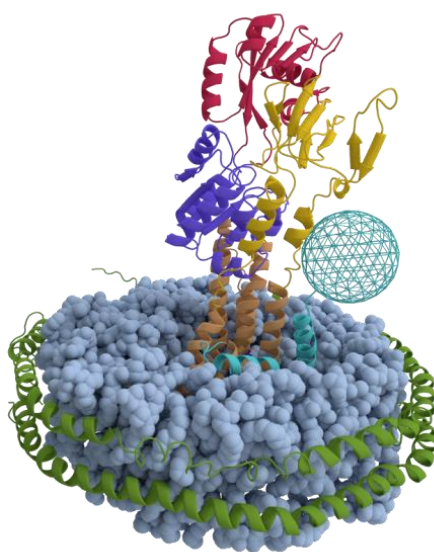
Figure 3.14: Illustration of *Lp*CopA embedded into a nanodisc. *Lp*CopA is embedded in to the lipid membrane (gray). Membrane scaffolding proteins (MSP, green) stabilize the hydrophobic rim of the lipid bilayer. The figure was created with the softwares PyMOL and Blender using PDB 4V6M for the MSP and lipid coordinates, and PDB 3RFU for the *Lp*CopA coordinates.

4. Spectroscopic determination of polarity gradients in the transport channel of *Lp*CopA

4.1. Introduction and overview

The functional reconstitution of *Lp*CopA into the controllable lipid environment of the nanodiscs set the basis for studying the involvement of the highly structured interface of water, protein, and lipids on the structure and function of the protein. The focus of this work was to investigate the hydration in the environment of the copper-binding motif CPC on TM helix M4. So far, crystallographic and computational studies suggest an unexpected open configuration of the copper exit channel in the E2.P$_i$ state of the enzymatic cycle [47], which would distinguish *Lp*CopA from other P-type ATPases, where this state is characterized by the luminal occlusion of the transport channel. Crystal waters as well as molecular dynamic (MD) calculations suggest a remarkable hydration of the channel with water reaching up to the cysteine C382 in the copper-binding site. This might play a role in the coordination of H-bond networks that are important for the exit of copper to the extracellular side. Here, experiments were designed to study polarity and water mobility in the environment of the main copper-binding motif in both a dynamic detergent-solubilized state and in the presence of a lipid bilayer. Therefore, these studies complement and expand the insights gathered from the crystal structures which are only static snapshots of the protein conformation obtained in the absence of a lipid bilayer. To this end, the polarity-sensitive fluorescent probe BADAN was introduced site-specifically into *Lp*CopA. Figure 4.1 shows a possible configuration of BADAN bound to the cysteines of the copper-binding site of *Lp*CopA.
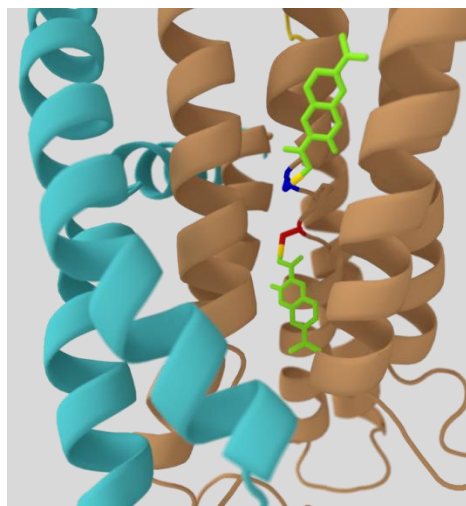
Figure 4.1: BADAN bound to the CPC motif of *Lp*CopA. The figure shows BADAN (light green) linked to C382 (red) and C384 (blue) of the copper-binding motif of *Lp*CopA. The orientation of BADAN is purely hypothetical and was adjusted manually respecting steric constraints. Also other orientations of BADAN are feasible. No software-based energy minimization of the BADAN orientation was attempted.

Fluorescence properties of BADAN. The fluorescent probe used in this study is the thiol-reactive naphthalene derivative BADAN (6-bromoacetyl-2-dimethylaminonaphthalene). With its small size, which is in the range of an amino acid side chain, and its short linker it allows monitoring local molecular details. Its fluorescence is sensitive to the polarity and solvent mobility in its immediate environment. Therefore, it is an excellent probe to study water distribution and dynamics in proteins [120]. Generally, BADAN exhibits a so called "dual fluorescence" [121] with two excited states: the locally excited (or Franck Condon) state and the internal charge transfer (ICT) state. The information on solvent polarity and mobility in the environment of the probe manifests mainly in the energy reduction of the more polar ICT state due to solvent relaxation (SR) as explained below. The locally excited state does not contribute due to the fast charge transfer process. Upon excitation the dipole moment of BADAN increases approximately threefold [122]. Therefore, solvent molecules reorient in order to minimize the total energy of the electronically excited chromophore and its solvation envelope. Since SR lowers the energy of the excited state, the relaxation process causes a continuous red-shift of the BADAN emission during the lifetime of the excited state. In other words, the longer the time between excitation and

photon emission the lower is its energy, since it originates from a more relaxed state. Clearly, the extent of SR depends on the amount and mobility of the water in the fluorophore´s environment, rendering it a measure of the polarity in the vicinity of the chromophore. However, it has to be noted, that also internal label dynamics, namely the rotation or wobbling of the propanoyl moiety with respect to the aromatic ring can lead to spectral shifts (see also Figure 4.4). As proposed by Koehorst el al. [120], the ICT species of BADAN can be further distinguished according to their hydrogen bonding mode as illustrated in the energy level scheme in Figure 4.2: in the ground state BADAN can be in a non-hydrogen-bonded ICT state, or hydrogen-bonded ICT state (HICT). The hydrogen bond can furthermore be immobile (i) or mobile (m) resulting in a $HICT_i$ and a $HICT_m$ state, respectively. The difference in the energy state between $HICT_i$ and $HICT_m$ can be attributed to solvent relaxation of water molecules as well as internal label dynamics. Due to the short excitation lifetime of BADAN of 5 ns [123] this energy difference is also reflected in the emission spectra. Consequently, information on solvent mobility can also be withdrawn from steady-state fluorescence spectra. However, a more detailed and unambiguous determination of solvent mobility can only be attained using time-resolved measurements.
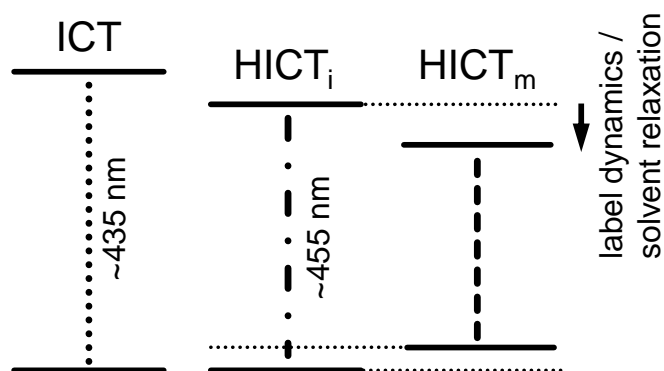
Figure 4.2 Energy level scheme of BADAN. The heterogeneity of the ground state results from differences in hydrogen-bonding capacity of BADAN in polar and apolar environments that subsequently will affect the various excited states. The three discriminated states denote the internal charge transfer state (ICT), the ICT state with an immobile hydrogen bond ($HICT_i$), and the ICT state with a mobile hydrogen bond ($HICT_m$). Information about solvent relaxation processes in the environment of the fluorescent probe can be obtained from the shift of $HICT_m$.

Principle of time-resolved fluorescence spectroscopy. Steady-state fluorescence spectra only contain time-averaged information on solvent relaxation. Hence, they can be understood as a weighed superposition of all relaxation states occurring during the lifetime of the fluorophore. Using time-resolved fluorescence spectroscopy, the evolution of the time-resolved spectra starting from the initial Franck-Condon state to the final completely relaxed state can be followed. Technically, this is usually accomplished using time-correlated single photon counting (TCSPC) [124]. The time-resolved emission spectra (TRES) are reconstructed from the obtained fluorescence decays at distinct wavenumbers. The information on the polarity (and also mobility) of the environment of the fluorophore is found in the time-dependent Stokes shift (TDSS), i.e. the shift of the emission maximum between the initial and the fully relaxed state. The kinetics, i.e. the time constants or relaxation times of the fluorescence decay, contain information on the solvent mobility in the environment of the probe. Thus, the results gained by time-resolved fluorescence spectroscopy provide quantitative information on the hydration and mobility of a specific site of the protein and monitor differences in the probe's microenvironment.

This chapter describes first the mutants designed to create site-specific polarity reporters in *Lp*CopA, the labeling strategy, and the quality controls of the dye–protein system. The second part of this chapter presents the results and the analysis of the polarity-sensitive fluorescence spectroscopy of BADAN in *Lp*CopA, obtained using steady-state as well as time-resolved fluorescence spectroscopy. Time-resolved fluorescence spectroscopy was performed in collaboration with the group of Prof. Martin Hof of the Academy of Sciences of the Czech Republic in Prague.

4.2. Results

4.2.1. Preparation of site-specifically labeled *Lp*CopA

Cloning of *Lp*CopA mutants for site-specific labeling. Besides the two cysteines in the copper-binding motif, CopA from *Legionella pneumophila* contains four cysteine residues in the two conserved copper-binding motifs in the

cytoplasmic heavy metal binding domain (HMBD). Thus, it was necessary to remove these residues in order to obtain information exclusively on the TM cysteines. It is expected that the elimination of the cysteines in the HMBD affects the functionality of *Lp*CopA, as observed for *Lp*CopA homologues [67, 125-127]. However, cysteine was substituted here by the sterically conserved and chemically related amino acid serine. Therefore, the overall structure and conformational flexibility of the protein was expected to be largely unaffected. The mutant lacking the cytoplasmic cysteines was denoted cmCopA, standing for "cysteine minus". It was created from the *Lp*CopA gene in the CopA_1N construct using PCR-based site-directed mutagenesis. Based on cmCopA, cmC382S and cmC384S were created. By this means, site-specific positioning of the polarity probe BADAN was allowed. Moreover, the completely cysteine-free ("cf") mutant cfCopA was created in order to evaluate unspecific labeling effects. Table 2.2 sums up the protein mutants and indicates the position of the BADAN label.

Table 4.1: *Lp***CopA mutants and the corresponding BADAN-label positions**

| protein name	mutations	reactive cysteines	name of labeled protein
*Lp*CopA	none	6	/
cmCopA	C18S/C42S/C56S/C59S	CPC	**BADAN-cmCopA**
cmC382S	C18S/C42S/C56S/C59S/C382S	C384	**BADAN@C384**
cmC384S	C18S/C42S/C56S/C59S/C384S	C382	**BADAN@C382**
cfCopA	C18S/C42S/C56S/C59S/C382S/C384S	none	**BADAN-cfCopA**

Recombinant production of *Lp*CopA mutants. For the recombinant expression of cmCopA, cmC382S, cmC384S, and cfCopA one needs to deviate from the original expression protocol for *Lp*CopA because expression of cmCopA was very weak in the C43(DE3)pLysS strain. Therefore, other strains were tested and robust and complete expression of cmCopA could be achieved in BL21(DE3)Rosetta (see Figure 4.3). Moreover, it was necessary to decelerate the cultivation and protein expression by inducing at the high OD of 1.0 and using an IPTG concentration of 0.5 mM. In the purification of the *Lp*CopA mutants β-ME

had to be omitted in order to avoid outcompeting of cysteine in the conjugation with the thiol reactive BADAN.
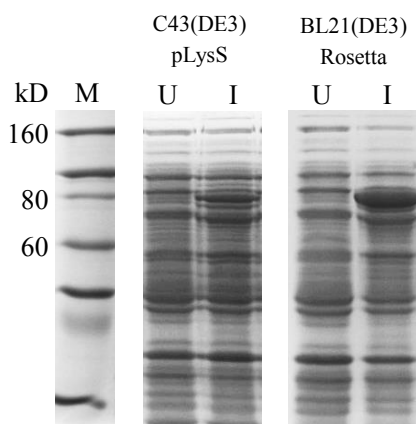
Figure 4.3: SDS-PAGE of cmCopA overexpression. M: protein size standard. All cell extracts were loaded on the SDS-PAGE at a concentration of 1 mg/ml. U: uninduced sample. I: protein expression was induced with 1 mM IPTG. Weak expression was found in the C43(DE3)pLys strain while robust and complete expression was found in the BL21(DE3)Rosetta strain.

Labeling of *Lp*CopA with BADAN. The polarity-sensitive fluorescent probe BADAN selectively reacts with the thiol moiety of the cysteine residues of the protein (see Figure 4.4).
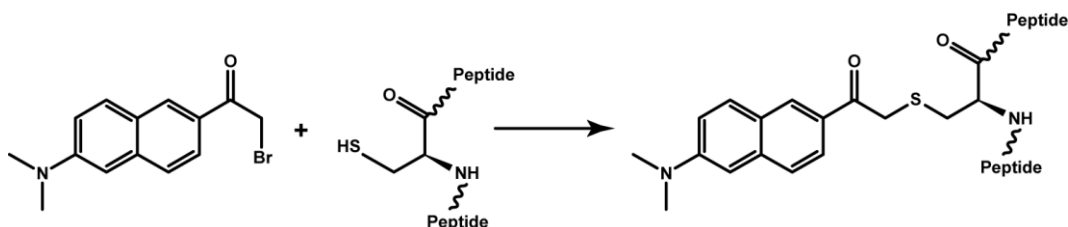

Figure 4.4: Conjugation scheme of BADAN with thiol groups. The highly reactive α-bromide of BADAN forms a stable covalent thioether bond with the protein *via* a nucleophilic attack by the sulfur of the cysteine residue.

Usually proteins are dye-labeled in a simple batch approach, where the protein is mixed with an excess of dye and incubated for a certain time in order to allow for the reaction to complete. Then, non-reacted dye is removed by dialysis or buffer exchange. However, experiments performed in our lab showed that when using this approach a significant amount of non-reacted BADAN remained in the sample which was not readily removable. One reason for this observation could be

the association of the hydrophobic BADAN with the detergent molecules in the protein-detergent micelle. In order to overcome this problem, a more efficient way of replacing the detergent was needed. Generally, detergents and buffers can be effectively exchanged while the protein is bound to an affinity resin. For instance, excess Coumarin dye could be successfully removed from a purified haloalkane dehalogenase by an additional IMAC after batch labeling [128]. Here, the process was further condensed by labeling the protein with BADAN on the IMAC column already during the purification (after contaminating proteins had been washed out using low millimolar imidazole concentrations). Monitoring of the BADAN absorption during the chromatographic run allowed following the labeling process online, as shown in Figure 4.5 exemplarily for cmC382S. For the other mutants very similar results were obtained.

A

B

C
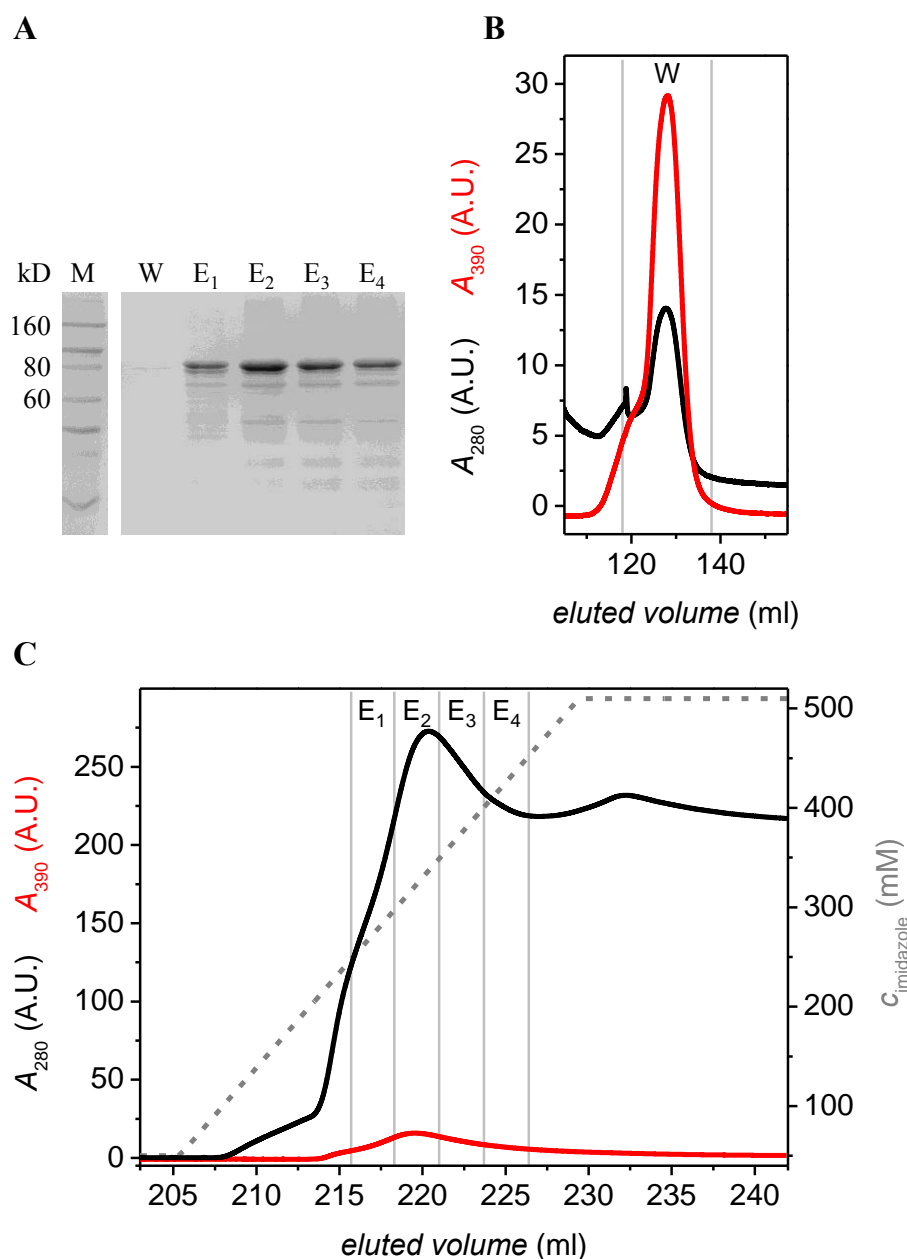
Figure 4.5: Labeling of cmC382S labeling with BADAN on the column. (**A**) SDS-PAGE of purification and on column labeling of cmC382S. M: protein size standard. W, E_1, E_2, E_3, and E_4 correspond to the IMAC fractions marked in the chromatograms in (**B**) and (**C**). (**B**) BADAN labeling and washing step on the HisTrap HP column. Protein and BADAN absorption was monitored at 280 nm (black line) and 390 nm (red line), respectively. The BADAN absorption shows a prominent peak after approximately 10 CVs of washing and returns back completely to the initial level, indicating that free BADAN has been removed completely. The small peak at 280 nm arises either from minor amounts of washed out protein or from the contribution of the additional BADAN-absorption peak at 290 nm. (**C**) Elution step of BADAN-labeled cmC382S from the HisTrap HP column. Color code is as in (**B**). The peaks of protein and BADAN absorption coincide, confirming the specific labeling of cmC382S.

Labeling efficiency and background determination. The label coupling efficiency (*CE*) was determined from the absorption spectra of labeled protein according to [95] and as described in section 2.6. The label *CE* is ~0.6 for all cmCopA mutants bearing one or two cysteines (cmC382S, cmC384S, and cmCopA). This suggests that even when two cysteines are available, preferentially only one is labeled. It can be concluded that BADAN preferentially reacts with C384 from the cytoplasmic side thereby obstructing sterically the access to the more membrane-inserted C382. This explains why cmCopA shows a label *CE* similar to the single cysteine mutants. Moreover, its fluorescence spectra resemble the spectra of BADAN@C384, as detailed in the next section. The label *CE* of cfCopA is ~0.2. The absorption spectra of BADAN-cmCopA and BADAN-cfCopA in detergent are shown in Figure 4.6 A. This implies that even after the extensive washing procedure a fraction of BADAN stays associated with the protein. This fraction probably results from unspecific binding to amines. Hence, up to 30% of the BADAN fluorescence may originate from a non-specific environment. This was taken into consideration for the data analysis by subtracting the 30% scaled spectrum of BADAN-cfCopA in detergent or nanodiscs (see Figure 4.6 B) from the sample spectrum. The comparison of Figure 4.6 C and D shows that this correction only led to a small shift of the spectral shape and did not devaluate the spectral interpretation. However, it should be noted that it is legitimate to assume that the background in the cysteine-bearing protein mutants is considerably lower than 30%, as unspecific binding is strongly suppressed when thiol groups as the preferential reactive groups are available.
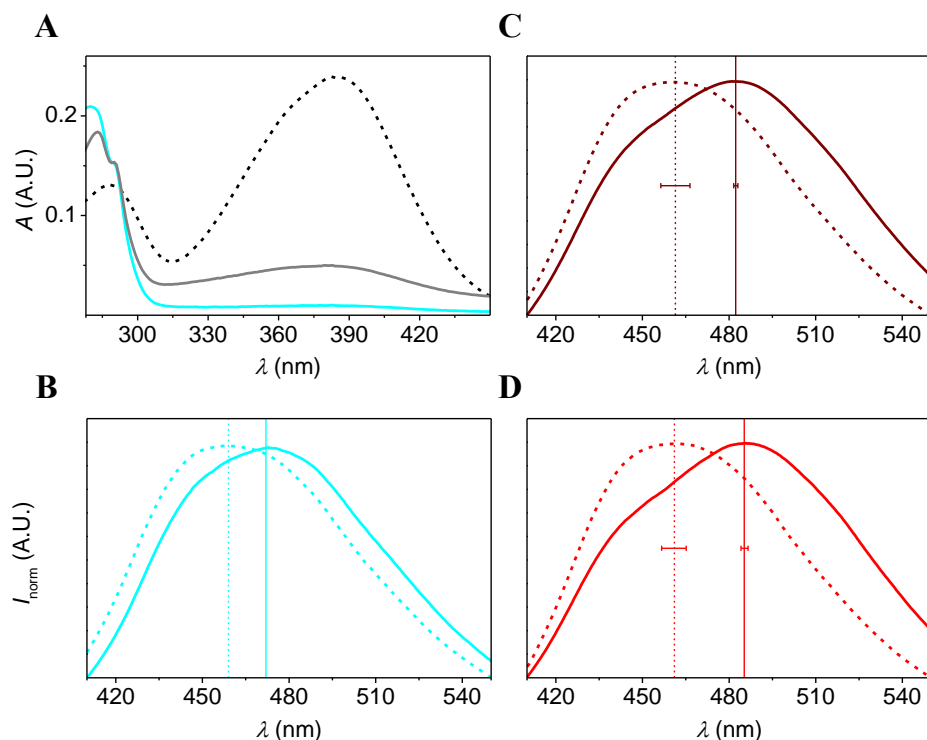
Figure 4.6: BADAN labeling efficiency and quality controls. (**A**) Absorption spectra of BADAN. The absorption spectra of a BADAN-β-ME adduct at 15 μM (dashed black line), and of BADAN-cmCopA (gray line) and BADAN-cmCopA (cyan line) in 0.15% DDM at 3 μM are shown. The label *CE* was determined to be 0.6 and 0.2 for BADAN-cmCopA and BADAN-cfCopA, respectively, according to [95]. (**B**) to (**D**) Normalized static fluorescence spectra of BADAN-labeled *Lp*CopA mutants upon excitation at 390 nm. Solid and dashed lines represent spectra obtained from protein in 0.15% DDM and reconstituted into asolectin-nanodiscs, respectively. Vertical lines indicate the position of maximum emission. The standard deviation is obtained from a minimum of three independent batches of experiments. (**B**) Spectra of BADAN-cfCopA. (**C**) Spectra of BADAN@C382. (**D**) Spectra of BADAN@C382 corrected for background fluorescence due to unspecific labeling of non-cysteine residues. To this end, the corresponding spectrum of BADAN-cfCopA (**B**) scaled to 30% intensity was subtracted from the raw data to account for the maximally possible influence of the unspecific signal.

Reconstitution of BADAN-labeled *Lp*CopA mutants into nanodiscs. The BADAN-labeled *Lp*CopA variants were reconstituted into nanodiscs prepared with asolectin essentially as described in section 3.2.4. In contrast to *Lp*CopA-nanodiscs, the preparation of cmCopA-nanodiscs contained a significant aggregate fraction. Since cmCopA was shown to be monomeric prior to the labeling procedure (not shown), partial aggregation is likely to have proceeded during the labeling. However, only monomeric protein can reconstitute into the nanodiscs. Therefore, the reconstitution and the ensuing size separation of the particles using SEC can be used as a selection process for monomeric and

properly folded membrane protein. BADAN-cmCopA-nanodiscs were obtained
from the peak at 11.8 ml, which overlapped in BADAN absorption and protein
absorption, as can be seen in Figure 4.7.
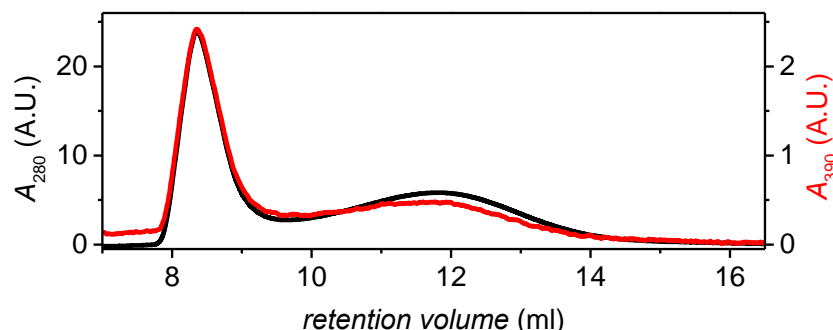
Figure 4.7: Size-exclusion chromatography of BADAN-cmCopA reconstitution into nanodiscs. Protein absorption was monitored at 280 nm (black line) and absorption of BADAN was monitored at 390 nm (red line). The absorption at 390 nm is scaled 1:10 for a better comparison. BADAN-cmCopA-nanodiscs were obtained from the peak at 11.8 ml. The peak at 8 ml contained aggregates of BADAN-cmCopA.

Secondary structure of BADAN-cmCopA in nanodiscs. The correct folding of
BADAN-cmCopA was also assessed by determining the secondary structure
using circular dichroism (CD) spectroscopy. Figure 4.8 compares the CD spectra
of BADAN-cmCopA in nanodiscs with the spectrum calculated from the weighed
spectra of empty MSP1E3D1(-)-nanodiscs and BADAN-cmCopA in 0.15% DDM
according to the protein mass fraction of *Lp*CopA and MSP1E3D1(-). A
*Lp*CopA-nanodisc contains one *Lp*CopA with a MW of 81,960 g/mol and two
MSP1E3D1(-) with a MW of 29,982 g/mol each. This yields a mass fraction of
0.57 and 0.43, respectively. The correlation between the measured and the
calculated spectrum further confirms that one *Lp*CopA is reconstituted per
nanodisc particle and that the secondary structure is not altered. Taken together,
these results show that *Lp*CopA can be selectively labeled with the cysteine-
reactive polarity-probe BADAN without affecting the protein integrity and that
the protein can still be successfully reconstituted into nanodiscs.
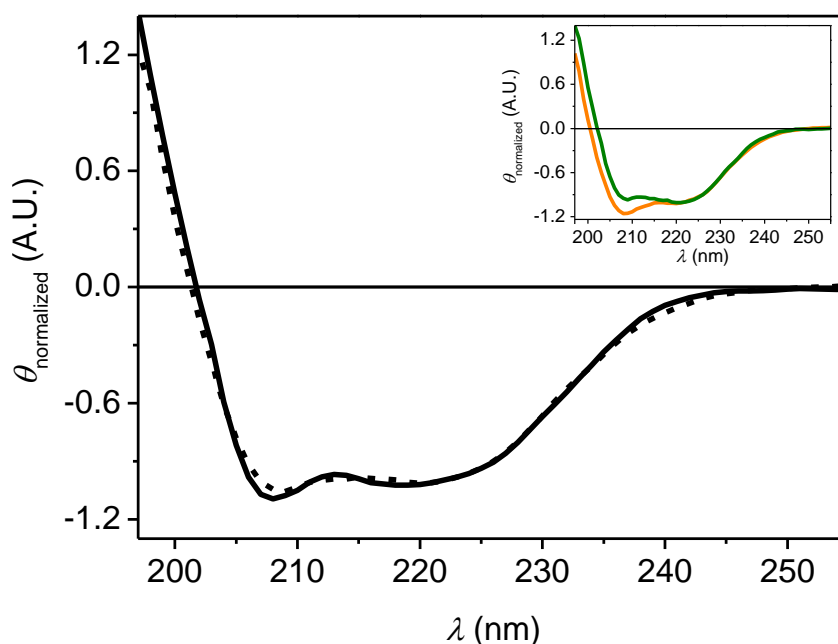
Figure 4.8: Circular dichroism spectra of *Lp*CopA. Measured spectrum of BADAN-cmCopA in nanodiscs (solid black line) and the same spectrum calculated from the spectrum of BADAN-cmCopA in 0.15% DDM and the spectrum of empty MSP1E3D1(-)-nanodiscs as described in the result section (dashed line). **Insert**: Reference spectra of BADAN-cmCopAC in 0.15%DDM (orange) and of empty MSP1E3D1(-)-nanodiscs (green).

4.2.2. Polarity and water mobility in the transport channel

The covalently bound polarity-monitor BADAN was site-specifically introduced into the copper-binding site of *Lp*CopA mutants. This section describes the study of micropolarity and solvent mobility around specific positions in the copper-binding motif using steady-state and time-resolved fluorescence spectroscopy and explains the implications of the results for the copper transport mechanism.

Steady-state spectroscopy of BADAN-labeled *Lp*CopA variants in micelles. First, BADAN-labeled *Lp*CopA mutants were studied in the flexible micellar state. These experiments address the question whether the TM helix packing interactions are sufficient to stabilize the hydrophobic core of the ATPase in the absence of additional protein–lipid interactions. Remarkably, pronounced differences between the spectral shapes of the steady-state spectra for different labeling positions are observed. The emission maximum of BADAN@C382 is 485.3 (±1.2) nm while emission is blue shifted to 471.5 (±2.1) nm in

BADAN@C384. BADAN-cmCopA exhibits an emission maximum at 468.3 (±1.9) nm which is very similar to BADAN@C384 (see Figure 4.9). This indicates that C384 is preferentially labeled in the presence of C382 such that the removal of C382 has little influence on the labeling behavior, provided that C384 is present. This finding agrees well with the observation that the label *CE* of cmCopA is in the same range as for cmC382S and cmC384S as detailed in the preceding section. The more membrane-inserted C382 could be labeled with BADAN in the cmC384S mutant, where no obstruction of the labeling accessibility from the cytosolic side by BADAN at C384 can occur. Strikingly, in DDM-micelles the more cytosolic cysteine C384 resides in a less polar environment than the membrane-buried C382 according to the steady-state spectra.
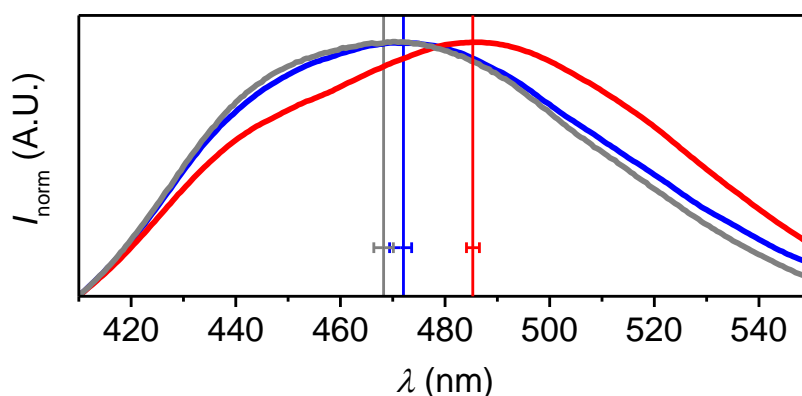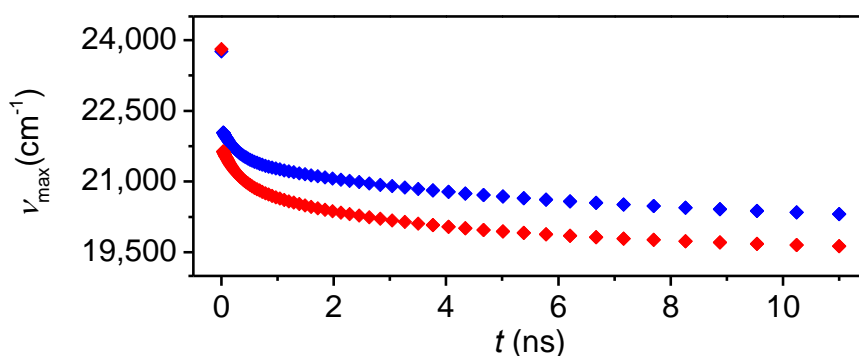

Figure 4.9: Normalized steady-state fluorescence spectra of BADAN-labeled *Lp*CopA mutants in DDM-micelles. The spectra were recorded in 0.15% DDM and background-corrected as described above and in Figure 4.6. Vertical lines indicate the position of maximum emission upon excitation at 390 nm. The standard deviation is obtained from a minimum of three independent batches of experiments. BADAN@C382 with $\lambda_{max} = 485.3$ (±1.2) nm, BADAN@C384 with $\lambda_{max} = 471.5$ (±2.1) nm, and BADAN-cmCopA with $\lambda_{max} = 468.3$ (±1.9) nm are represented by red, blue, and gray lines respectively.

Time-resolved spectroscopy of BADAN-labeled *Lp*CopA mutants in micelles. Steady-state spectra of BADAN do not contain direct information the kinetics of solvent relaxation. Rather, they represent a superposition of the time-resolved emission spectra (TRES) and can therefore only give time-averaged information on the polarity of the fluorophore's environment. In order to obtain the Stokes shift dynamics, time-resolved emission intensities were measured at different

wavelengths. Figure 4.10 shows the time evolution of TRES peak maxima of BADAN@C382 and BADAN@C384. As expected, the energy of the emitted photons (shown as maximum wavenumber ν_{max}) decreases over time. Clearly, the total Stokes shift, that is the difference in maximum wavenumber between $t = 0$ and $t = \infty$, is much larger for BADAN@C382 than for BADAN@C384 (4,250 cm^{-1} and 3,650 cm^{-1}, respectively), which confirms the higher polarity in the environment of the buried C382 seen already in the static emission spectra.

Additionally, the relaxation time τ_r can be calculated from the kinetics of the decay. The relaxation times τ_r, which directly reflect the microviscosity, i.e. the mobility of the dye environment, are in the ns-range for both probe positions, implying that the water is "structured" and no bulk water is observed. The relaxation time $\tau_r = 1.84$ ns of BADAN@C384 is longer than the $\tau_r = 1.23$ ns measured for BADAN@C382. This implies that the environment of BADAN attached to the buried C382 residue is not only more hydrated but that the water is also more mobile than in the environment of C384.

Figure 4.10: Time evolution of TRES peak maxima of BADAN-labeled *Lp*CopA mutants in DDM-micelles. The spectra were recorded in 0.15% DDM and are not background-corrected. Samples were excited at 375 nm. Total Stokes shifts of 4,250 cm^{-1} and 3,650 cm^{-1} were determined for BADAN@C382 (red diamonds) and BADAN@C384 (blue diamonds), respectively. The relaxation times τ_r of BADAN@C382 and BADAN@C384 are 1.23 ns and 1.84 ns, respectively. This implies that the environment of BADAN@C382 is more polar and also more mobile than that of BADAN@C384.

Taken together, it can be concluded from the steady-state and time-resolved fluorescence spectroscopy of BADAN-labeled *Lp*CopA mutants that a pronounced hydration gradient within a small distance is realized in the environment of the CPC copper-binding motif of the protein. According to the

crystal structure, the S–S distance of the residues C382 and C384 is only 9 Å. However, the actual probe distance may be larger due to label and linker size and uncertainties in label orientation. In the flexible detergent solubilized state, the microenvironment of the more cytoplasmic C384 is less polar and contains less mobile water than the environment of the more buried C382. This unexpected result supports MD calculations on LpCopA in the E2.P$_i$ state by Andersson et al. [47] that suggest that water molecules penetrate the transport channel up to C382, presumably *via* the proposed copper exit pathway to the extracellular side. However, the MD calculations were carried out in a model lipid environment, whereas here the high degree of hydration is observed in the more flexible micellar state. Obviously, however, C382 is the intrinsically favored hydration site over C384 when sufficient structural flexibility of the TM domains is provided in a micellar state. It can be expected that LpCopA is preferentially stabilized in the E2.P$_i$-state since all spectra were recorded at high sulfate concentration which was reported to act as a phosphate analogue in P-type ATPases by binding to the phosphate binding site in the P-domain and thereby stabilizing the protein in an E2.P$_i$-like conformation [108, 129]. Accordingly, the observation that the hydration in the TM channel increases towards the extracellular side is in line with the open exit pathway proposed for LpCopA [47, 68], although fluctuations into other states may also be possible as the detergent provides little structural constraints.

### 4.2.3. Influence of the lipid bilayer on protein hydration.

Protein–lipid interactions are well known to be crucial for structural and functional tuning of a membrane protein. Therefore, the influence of a lipid bilayer on helical packing and intra-protein hydration at the copper-binding site was studied for LpCopA reconstituted into asolectin-nanodiscs.

Steady-state spectroscopy of BADAN-labeled LpCopA mutants in nanodiscs. Figure 4.11 shows that the emission maximum for BADAN@C382 shifts significantly by approximately 21 nm to 461.4 (±5.0) nm upon insertion into the nanodiscs, whereas the emission maximum of BADAN@C384 experiences a small shift by approximately 6 nm to 465.6 (±1.8) nm. The shift upon membrane

insertion for BADAN-cmCopA by approximately 6 nm to 464.8 (±2.2) nm is again very similar to the shift observed for BADAN@C384. Thus, the polarity in the environment of the more cytoplasmic C384 is only weakly influenced by the lipid environment, while hydration of the more membrane-buried C382 is much more variable. This indicates that the hydration of C382 is not determined by TM helix packing interactions, but strongly controlled by protein–lipid interactions. The lateral pressure exerted by the lipidic phase in the nanodisc is considered to match that in native plasma membranes [130, 131] and is probably the salient factor that lowers the hydration of the protein interior.
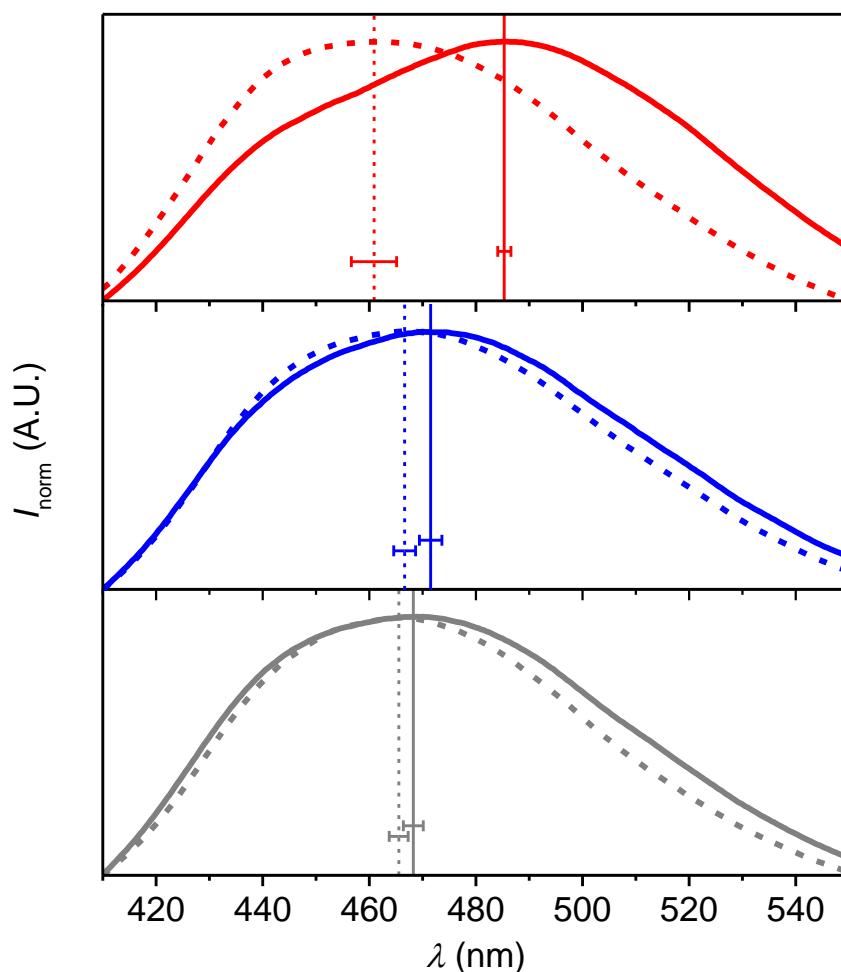
Figure 4.11: Normalized steady-state fluorescence spectra of BADAN-labeled *Lp*CopA mutants in DDM-micelles and nanodiscs. Spectra of *Lp*CopA mutants in 0.15% DDM (solid lines) and in asolectin-nanodiscs (dashed lines) are shown. The color code is as in Figure 4.9. Background-correction was performed as described above and in Figure 4.6. Vertical lines indicate the position of maximum emission upon excitation at 390 nm. The standard deviation is obtained from a minimum of three independent batches of experiments. (**A**) The λ_{max} of BADAN@C382 is 485.3 ($\pm$1.2) nm in detergent and shifts to 461.4 ($\pm$5.0) nm in nanodiscs. (**B**) The λ_{max} of BADAN@C384 is 471.5 ($\pm$2.1) nm in detergent and 465.6 ($\pm$1.8) nm in nanodiscs. (**C**)The λ_{max} of BADAN-cmCopA is 468.3 ($\pm$1.9) nm in detergent and 464.8 ($\pm$2.2) nm on nanodiscs.

Quantitative analysis of the steady state emission spectra. Additionally to the plain comparison of the shifts of the fluorescence emission maxima of the steady-state spectra, a more thorough quantitative analysis of the spectral shapes was performed. Due to the heterogeneity of the ground state of BADAN which consequently affects also the excited states as described in section 4.1, the fluorescence of protein-bound BADAN does not exhibit a simple line shape. Rather, the spectra represent a superposition of multiple Gaussian bands. Koehorst

71

et al. [120] proposed the decomposition of the spectra into three components according to the energy scheme of BADAN presented in Figure 4.2. The energy of the ICT and the $HICT_i$ species can be fixed, as solvent relaxation does not play a role for these states and thus the energy, i.e. the wavelength of maximum emission, does not change. The energy of the initial excited state of the $HICT_m$ species, on the contrary, can be lowered by solvent relaxation in the environment of the fluorophore if the reorientation of the water dipoles is much faster than the depopulation of the excited state. Additionally to solvent relaxation, internal label dynamics may contribute to the energy reduction of the $HICT_m$. The excited state energy, i.e. the maximum wavenumber (or indirectly the maximum wavelength) of the $HICT_m$ species, can serve as a measure for the solvent mobility of the fluorophore´s environment. The Gaussian decompositions into the components representing the ICT, $HICT_i$, and $HICT_m$ species of BADAN are shown in Figure 4.12 for BADAN@C382 and BADAN@C384 in micelles and nanodiscs, respectively. An overview of the obtained parameters can be found in Table 4.2.
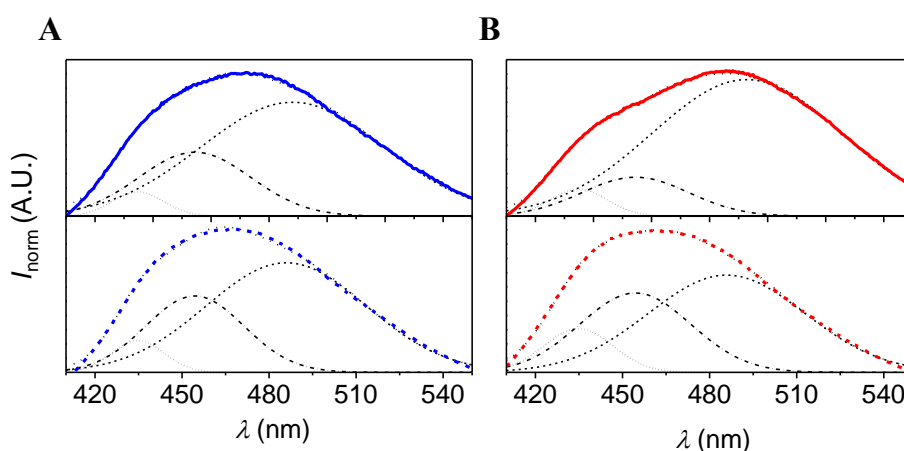
Figure 4.12: Decompostion of the steady-state fluorescence spectra according to the energy level scheme of BADAN. The color code is as in Figure 4.9 and according to the energy scheme in Figure 4.1. The ICT, $HICT_i$, and $HICT_m$ contributions are represented by dotted, dotted-dashed, and dashed black lines, respectively. (**A**) Decomposition of the spectra of BADAN@C384 in micelles (upper panel) and in nanodiscs (lower panel). (**B**) Decomposition of the spectra of BADAN@C382 in micelles (upper panel) and in nanodiscs (lower panel). An overview of the determined parameters can be found in Table 4.2.

Reconstitution of BADAN@C382 into nanodiscs caused a blue shift of λ_m from 493 to 486 nm. On the energy-proportional wavenumber scale, the excited state of BADAN linked to C382 is thus by 289 cm^{-1} (equivalent to ~37 meV or ~3.6 kJ/mol) higher in nanodiscs than in the micellar system. The population of the spectral fraction f_m decreases by 0.26 while f_i increases by 0.20. Thus, also the population of the ICT species is slightly increased. Hence, the lipid bilayer reduced the extent to which dipolar relaxation processes in the vicinity of the fluorophore lowered the energy of the excited state of BADAN. On the contrary, BADAN@C384 showed a much weaker dependence of λ_m on the insertion into nanodiscs. The λ_m shift from 488 nm to 486 nm corresponds to a relative energy difference of only 92 cm^{-1}. The different spectral response of the two sites to lipid insertion is due to a lower hydration around position 384 in the micellar state of the protein as compared to position 382, whereas both sites sample almost identical dielectric properties in the ND-inserted state. Comparing the obtained parameters with a reference data set acquired for the α-helical membrane-embedded M13 major coat protein by Koehorst et al. [120, 132] reveals that the values of f_m and v_m of BADAN@C382 in nanodiscs are typical for the glycerol-backbone region, while they are typical for a water exposed protein region when the protein is solubilized in a detergent micelle. However it has to be noted that in the *Lp*CopA structure BADAN is not in contact with a lipidic phase but rather sandwiched between the TM helices. Therefore, label dynamics are expected to be more restricted than in the single TM helix reference protein.

Generally, the decomposition of the spectra according to the spectral fractions of BADAN is consistent with the qualitative analysis of the spectra and indicates that the polarity in the environment of the membrane-buried C382 is strongly dependent on the lipidic phase, while the C384 environment exhibits a relatively stable hydration. In terms of possible functional transitions, the data show that C382 could be a flexible intra-protein hydration site that could be well regulated through altered helix arrangements under the influence of the ATP-hydrolytic cycle. In contrast, the structure around C384 appears to form a more stable "hydrophobic gate" which is largely defined by inter-helical contacts with little additional influence by altered helix packing.

Table 4.2: Parameters for the decomposition of the steady-state fluorescence spectra according to the energy level scheme of BADAN

| | BADAN@C384 | | BADAN@C382 | |
	micelle	nanodisc	micelle	nanodisc
f_i	0.24	0.28	0.13	0.33
f_m	0.71	0.66	0.82	0.56
v_m (cm^{-1})	20,489	20,579	20,292	20,581
λ_m (nm)	488.1	485.9	492.8	485.9

Time-resolved spectroscopy of BADAN-labeled *Lp*CopA mutants in nanodiscs. Figure 4.13 shows the fluorescence decays of BADAN@C384 and BADAN@C382 reconstituted into asolectin-nanodiscs compared to the respective spectra in DDM-micelles. With 3,600 cm^{-1}, the total Stokes shift for BADAN@C384 in nanodiscs is only slightly smaller than the value in detergent (3,650 cm^{-1}), whereas the total Stokes shift for BADAN@C382 decreases considerably to 3,200 cm^{-1} in the nanodiscs as compared to 4,250 cm^{-1} in the detergent micelle. This reflects the drop in polarity that was also seen in the static spectra. For BADAN@C382 the relaxation time τ_r increases slightly from 1.23 to 1.34 ns upon membrane insertion, reflecting a slightly reduced solvent mobility in the environment of the probe. Surprisingly, in the case of BADAN@C384 the relaxation time τ_r decreases from 1.84 to 1.30 ns which would imply that the solvent mobility in the environment of BADAN@C384 increases upon membrane insertion. The reason for this observation is not clear and does also not correspond with the results obtained from the quantitative analysis of the steady-state spectra. However, all determined relaxation times comply with the assumption of "structured" water in the environment of the BADAN probe and exclude the presence of bulk water.
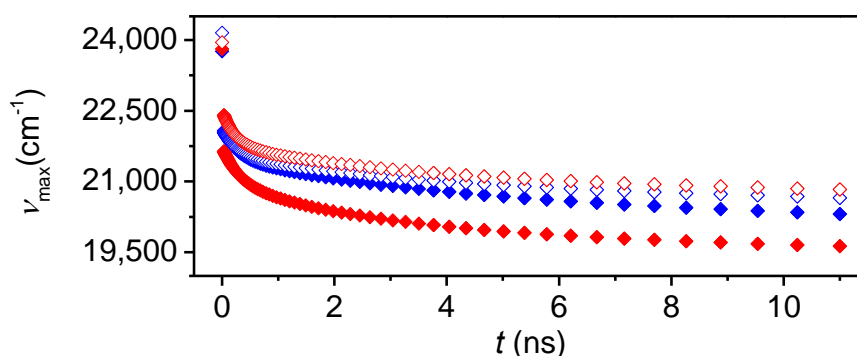
Figure 4.13: Time evolution of TRES peak maxima of BADAN-labeled *Lp*CopA mutants in DDM-micelles and nanodiscs. The spectra were recorded in 0.15% DDM (filled diamonds) and in asolectin-nanodiscs (open diamonds) and are not background-corrected. Samples were excited at 375 nm. The total Stokes shift of BADAN@C384 (blue) in nanodiscs is 3,600 cm^{-1} and is only slightly smaller than the corresponding value in micelles (3,600 cm^{-1}). The total Stokes shift of BADAN@C382 (red) in nanodiscs is 3,200 cm^{-1} and is thus considerably smaller than the corresponding value in micelles (4,250 cm^{-1}).

In summary, it was found that the microenvironment of the more cytoplasmic C384 is less influenced by the membrane insertion while the microenvironment of the buried C382 changes dramatically upon membrane insertion. The degree to which the polarity around the two cysteine residues depends on lipid-induced helical packing does not correlate in an intuitive manner with the topology of the two residues: C384 resides at the interface of the aqueous and the membrane phase, where a more variable hydration would be expected, while one would expected a more stable hydrophobic environment for the more membrane-embedded C382, regardless of the lipidic environment. However, steady-state as well as time-resolved fluorescence using the environment-sensitive probe BADAN show that upon lipid-reconstitution the hydration in the environment of C382 drops significantly to a similar value as for the environment of C384 in the lipid bilayer. According to the time-resolved fluorescence data, the degree of water mobility is comparable at both sites. This is also consistent with the finding that the mobile fractions of BADAN at C382 and C384 in nanodiscs have the same excited state energy.

4.2.4. Estimation of the heterogeneous dielectric constant around the CPC motif

The shifts of steady-state and time-resolved fluorescence spectra provide information on relative changes of the micropolarity and solvent mobility in the environment of the BADAN probe. These values were related to the local dielectric constant within the protein. To this end, reference spectra of a BADAN-β-mercaptoethanol (β-ME) adduct in solvents of known permittivity were recorded. Unlike the BADAN-protein spectra, these spectra exhibit a single Gaussian shape because the spectral contributions of ICT and $HICT_i$ are negligible in the mobile isotropic solvent environment. Figure 4.14 shows the close to linear dependence of the wavenumber v_{max} at the emission maximum on the relative permittivity ε. In water ($\varepsilon = 80.1$) BADAN-β-ME exhibits a v_{max} of approximately 18,000 cm^{-1}. This represents the state of both maximal polarity and maximal solvent dipole mobility. In the protein context, this corresponds to BADAN bound to a fully bulk-water exposed and fully flexible amino acid. However, the maximum wavenumbers v_m of the $HICT_m$ species of BADAN-labeled *Lp*CopA variants are found in the region between 20,300 cm^{-1} and 20,580 cm^{-1}, which would correspond to dielectric constants between 15 and 5 in a fully mobile solvent (see Figure 4.14). However, given the stronger sterical restriction of BADAN within the multi-helical protein structure as compared to the solvent model, the dielectric estimates provide only lower limits of ε for the protein-interior. In the context of a phospholipid bilayer these values would typically correspond to the glycerol backbone region and low phosphate region [133]. On the other hand, typical values of relative permittivity in the interior of a protein range between 3 and 6, while significantly higher values of up to 20 are reported for the protein-water interface of soluble proteins where easier polarizable amino acid side chains reside [134-136]. First of all, the consistency between the published and the experimentally determined scales demonstrates the general applicability of this approach. According to the linear dependence of v_{max} and ε, the permittivity ε in the environment of BADAN@C382 is >15 in the flexible detergent environment, while the corresponding value for BADAN@C384 is only >8. For both BADAN positions, the value shifts down

to >5 upon reconstitution of the protein into nanodiscs. These results imply that the dielectric constant around the CPC is still higher than in a typical protein interior when *Lp*CopA is buried in the lipid membrane and that no significant difference is found between the environment of C382 and C384. However, differences between the BADAN positions are seen for the flexible micellar environment. Here BADAN samples a considerably higher dielectric constant in the environment of the buried C382 than in the environment of the more cytoplasmic BADAN@C384.
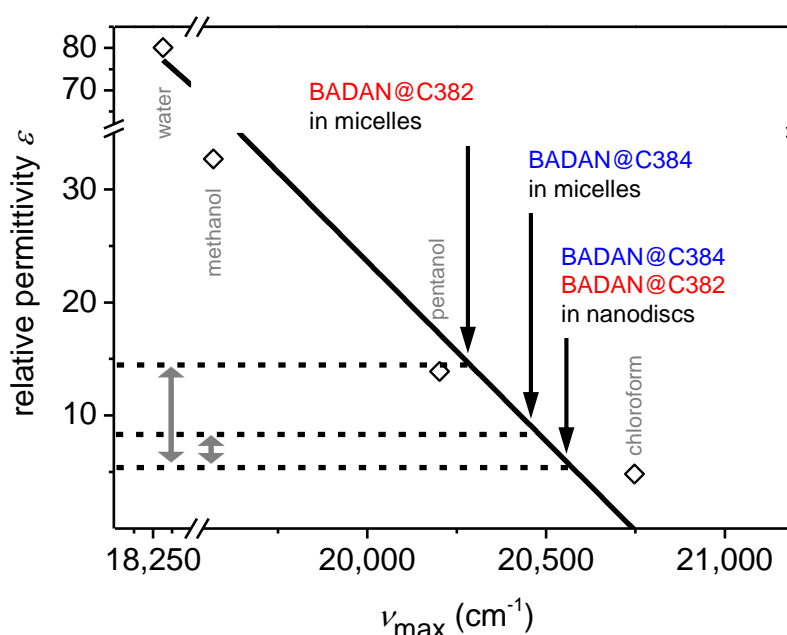

Figure 4.14: Correlation between maximum wavenumber of BADAN emission and relative permittivity. The emission maxima v_{max} of a BADAN-β-mercaptoethanol adduct in reference solvents were determined and correlated to their relative permittivity ε. This reference line was used to estimate the dielectric constant corresponding to the maximum wavenumber v_m of the HICT$_m$ species of BADAN bound site-specifically to *Lp*CopA mutants in detergent-micelles and nanodiscs.

4.3. Summary and discussion

Studying hydration and water mobility in the TM copper channel of the P$_{IB}$-type copper-transporting ATPase CopA from *Legionella pneumophila* allows new insights into the mechanism of copper transport through the protein. This is of particular interest, because intra-protein hydration will affect the fate of the hydration shell of the copper ion which needs to be rearranged during transport.

Since this is a fundamental requirement of any ion transport process through hydrophobic barriers, the obtained data are of general importance for the understanding of ion transport mechanisms. Here, intra-protein hydration was studied in a flexible micellar state of the protein and compared with its more rigid membrane-embedded state using the polarity-sensitive fluorescent probe BADAN. Information on hydration and water mobility was obtained applying steady-state as well as time-resolved fluorescence techniques. To my knowledge these studies are the first example of applying time resolved-fluorescence to investigate water dynamics in the active site of a membrane protein. Previous work on the soluble haloacid dehalogenase [128] or isolated cytoplasmic domains of the SERCA [137] already showed impressively the potential of the method. Moreover, steady-state spectroscopic studies using polarity-sensitive dyes have so far mostly focused on monitoring sites located at the TM protein surface and therefore monitored direct protein–lipid interactions rather than lipid-dependent intra-protein hydration.

Here, a novel labeling method together with thorough quality controls allowed the site-specific study of the environment of the conserved copper-binding residues C382 and C384 in the TM helix M4 of *Lp*CopA. Notably, it was shown that the environment of the main copper-binding motif CPC in the transmembrane channel of *Lp*CopA is characterized by strong hydration gradients within very small distances and that the presence of a lipidic phase affects the environment of the more membrane-buried C382 significantly. Generally, the relaxation times deduced from the time-resolved fluorescence data characterize the water as "structured" at both positions and exclude the presence of bulk water. A careful analysis of the crystal structure of *Lp*CopA (PDB 3RFU) with respect to the properties of the amino acids in the environment of C382 and C384 in a radius of ~5 Å reveals that the increased hydration in the environment of C382 does not coincide with a "higher density" of polar residues. Rather, C384 is located closer to polar residues. Thus, the observed high and variable hydration around C382 can probably be directly attributed to the penetration of water from the luminal side of the channel. Figure 4.15 shows a synopsis of all relevant parameters determined in this chapter.
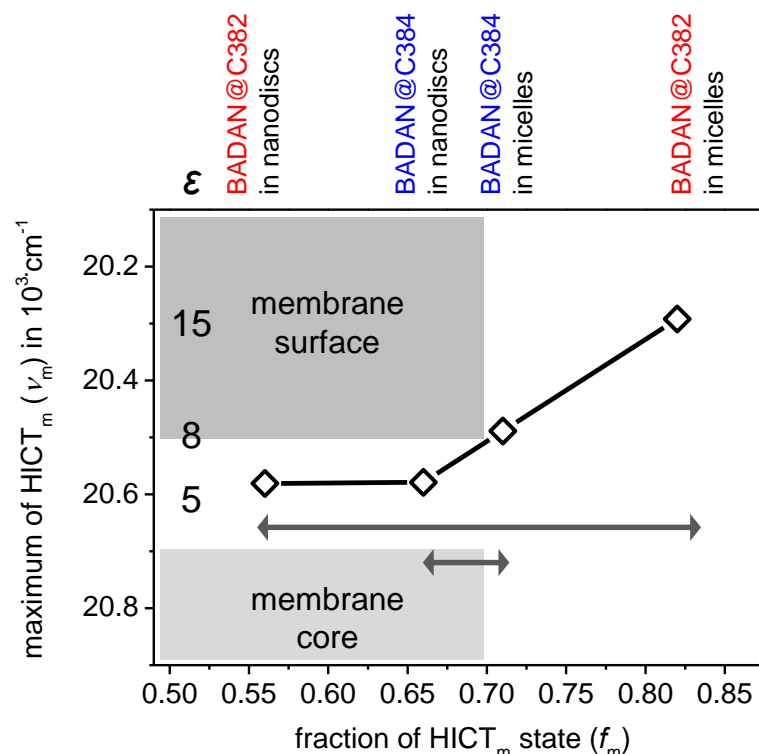
Figure 4.15: Correlation between the polarity and water mobility in the environment of the copper-binding CPC motif of *Lp*CopA. The environment of BADAN@C382 in micelles is characterized by a large fraction of water $f_m = 0.82$ with high mobility, reflected by the position of $v_m = 20,292$ cm^{-1}. The associated lower boundary of the dielectric constant is $\varepsilon \approx 15$. Upon reconstitution into nanodiscs a substantial drop in f_m to 0.56 and an increase of v_m to 20,581 cm^{-1} (corresponding to $\varepsilon > 5$) was observed. The environment of BADAN@C384 in micelles is characterized by moderate polarity ($f_m = 0.71$) and water mobility ($v_m = 20,489$ cm^{-1}, $\varepsilon > 8$) Membrane insertion led to only a small decrease in in polarity ($f_m = 0.66$) and solvent mobility ($v_m = 20,580$ cm^{-1}, $\varepsilon > 5$). The shaded areas represent the typical parameter ranges found in the membrane core (average $v_m > 20,500$ cm^{-1}) and the membrane surface region (average $v_m < 20,500$ cm^{-1}) of a bilayer as determined in [132].. Distinct hydration gradients characterize the environment of the CPC motif. Hydration and water mobility at the more membrane-buried residue C382 are strongly affected by the presence of a lipidic phase.

In the micellar state, the value of v_m differs by 197 cm^{-1} (equivalent to ~25 meV or ~2.4 kJmol^{-1}) between the BADAN positions at C384 and C382. The higher water mobility (lower v_m) around C382 correlates also with a higher fraction f_m. The concerted change of both variables indicates that a higher amount of inter-helical water near C382 causes a softening of intra-membrane protein structure, thereby allowing also more efficient solvent relaxation. The values of v_m correspond to approximate relative permittivities ε of >9 and >15 for BADAN@C384 and BADAN@C382, respectively. Thus, the dielectric environment of these residues is significantly more polar than the hydrophobic

interior of membrane proteins. The results demonstrate that helical packing interactions are sufficient to shield C384 from more extensive hydration despite its exposed location, whereas C382 resides in an intra-membrane protein hydration site.

Upon membrane reconstitution, the amount (f_m) and the mobility (v_m) of water decrease significantly for both label positions. This implies that the structural constraints exerted by the lipid bilayer lead both to the exclusion as well as to the immobilization of water in the environment. However, the effect is much more pronounced for BADAN@C382. Here, the lipid reconstitution induces an energy difference of 298 cm^{-1} (~37 meV or ~ 3.6 kJ/mol) with respect to the micellar state. In the lipid bilayer, the CPC motif senses a rather uniform dielectric environment of $\varepsilon > 5$ due to the reduced polarity around C382. Interestingly, the intra-membrane protein dielectric properties around C384 and C382 of the protein in nanodiscs very much coincide with those of the surrounding bilayer at the membrane surface and sub-head group region, respectively. The homogenous dielectric environment becomes strongly inhomogeneous by intra-membrane protein hydration at C382 upon reduced lateral pressure.

Taken together, these results illustrate the assumed significant role of intra-protein hydration for the transport mechanism of P$_{IB}$-type ATPases. Remarkable intra protein hydration has been seen in crystallographic snapshots and MD calculations of *Lp*CopA before. Moreover, a comparatively hydrated TM domain of the *Lp*CopA homologue from the thermophilic archaeon *Archaeoglobus fulgidus* could also explain its potential to be reversibly unfolded [117]. Notably, a more static and comparatively low hydration was found around the more cytoplasmic residue C384. This cysteine residue is less conserved and can be substituted by serine or histidine within the subclass of P$_{IB}$-type ATPases [41, 138]. In contrast, the more-membrane-buried cysteine of the metal-binding motif (C382 in *Lp*CopA), which was found to feature a highly variable environment in terms of hydration is stronger conserved. This notion coincides well with the finding by Renthal [139] that buried water sites are conserved across families of proteins and play an important role not only in structural stabilization but also correlate with protein function.

In the context of the fragmentary knowledge on the Cu^+-transport mechanism of *Lp*CopA, the obtained results could fill some evident gaps. The more exposed C384 is assumed to play a role in initial copper coordination together with M148 [47]. The low hydration in its environment suggests that it is the site where the hydration shell of the Cu^+-ion is partially stripped off to enable its binding to the protein. Moreover, this site could serve as a "hydrophobic gate" preventing the back-diffusion of the Cu^+-ion to the cytoplasm. The variable hydration in the environment of the more membrane-buried C382 which is involved in high-affinity copper coordination together with M717 indicates that this site might play an important role for the re-solvation of the Cu^+-ion in order to prime it for extrusion to the luminal side of the membrane. This variability indicates also the conformational flexibility of this region of the protein. The conserved site may thus constitute a default "switch" as part of the ATP-driven enzymatic reaction cycle. This implies that the balance between forces exerted by the lipid membrane like lateral pressure and hydrophobic match on the one hand and those exerted by the cytosolic head piece on the TM helices on the other hand, plays a crucial role in determining the water accessibility and mobility in this protein region. The data suggest that in the resting state, the TM domain of the ATPase is in a compact state matching the dielectric properties of the surrounding membrane. Intra-membrane protein hydration near C382 would then occur transiently during the Post-Albers cycle due to forces exerted by the catalytic head piece and possibly initiate the extracellular ion release. In this picture, lateral pressure would act as the restoring force that dehydrates the copper binding motif and re-establishes the dielectric match with the planar bilayer.

Changes in internal hydration in different states of a membrane protein have been previously shown for the light activated state of rhodopsin [140-142], where increased hydration was specifically attributed to the metarhodopsin-I-intermediate as determined by NMR. Moreover, the functional role of water dynamics has been studied using MD calculations e.g. for the Na^+-channel Gramicidin A [143] or for the proton pump AHA2 [144]. On the other hand, it is well recognized that the lipid environment can strongly influence the population of conformational states and therewith protein activity, e.g. for rhodopsin [16] or

the prototypical P-type ATPase SERCA. In fact, SERCA is activated by a specific hydrophobic mismatch between its TM region and the surrounding lipid membrane [40, 145]. This can be understood when taking into consideration that conformational changes during function lead to the shift of membrane domains, such that the hydrophobic thickness of the membrane protein changes and, consequently, also the hydrophobic match. Thus, the state of ideal hydrophobic adaption between lipid bilayer and protein TM region can only be transient during a functional cycle. Instead, states of hydrophobic mismatch pose energetically unfavorable barriers that are important for reaction kinetics. In this case, altered protein–lipid interactions reduce the energy barrier to reach the different protein conformations. It is expected that these interactions between the protein and the lipid membrane are especially important for membrane proteins that undergo large conformational changes during their enzymatic cycle, such as P-type ATPases. In contrast, in comparatively rigid and tightly packed TM proteins like dark-state bovine rhodopsin the packing and structure is largely independent of the lipidic environment, as judged from the unaltered absorption of the 11-cis-Retinal chromophore [79]. Similarly, it is conceivable that solvation forces exerted by the high water potential which constantly counteracts on the stabilizing protein–protein and protein–lipid interactions ultimately contributes to enabling the conformational changes required for protein function. In case of *Lp*CopA this possibility appears to be particularly important for transporting the initially hydrated copper ion through the membrane channel. The controlled but transient coordination of the copper ion by the protein needs to be achieved by partial stripping of the hydration shell. Thus, the discovered high variability of hydration around the buried C382 may be functionally important during re-solvation of the copper ion [47, 68, 146].

In summary, it can be proposed that the environment of C384 serves as a "hydrophobic gate" preventing the re-diffusion of the copper ion to the intracellular side while variable polarity around C382 could contribute to directing the copper ion towards the extracellular exit site of the channel during the E2 steps of the enzymatic cycle. The results agree with the observation of water accessibility of the CPC motif as deduced from the crystal structure and the

MD calculations in the $E2.P_i$ transition state. However, the data presented in this chapter demonstrate that the hydration of the exit channel is under the strong control of the lipidic phase which may thus act as a restoring force for structural changes induced by ATP-hydrolysis. Thus, the unexpected "open" $E2.P_i$ transition state seen in the crystals could partly be a consequence of the high flexibility of this part of the protein structure in the absence of the sterical constraints of a lipid bilayer. Regarding the importance of a transiently formed large dielectric gradient across the CPC motif, it is plausible that this gradient is crucial for the directionality of ion transport. The restriction of peptide bond rotation by the conserved proline residue that separates the two studied cysteine residues probably gives structural support for the formation of adjacent domains of different flexibility and dielectric property.

5. Studying lipid interactions of the amphipathic helix MBb at the copper entry platform of *Lp*CopA

5.1. Introduction and Overview

The crystal structure of *Lp*CopA revealed that the entry site to the copper transport channel forms a wide entry platform (see also Figure 1.4). The class-IB-specific TM helices MA and MB constitute part of this platform and the helix MB kinks at the cytosolic membrane interface to form the amphipathic helix MBb. This entry platform is assumed to serve as a docking site for the HMBD or soluble copper chaperones due to electrostatic interactions and to be involved in initial low-affinity copper coordination [74]. From a biophysical point of view it is remarkable that the amphipathic helix MBb resides at the presumed interface between the aqueous cytoplasm and the lipid bilayer and is therewith exposed to environments with drastically different dielectric properties. This would render the amphipathic character, i.e. the positioning of polar and hydrophobic side chains at opposite sides of the helical structure, important in regulating the protein tertiary structure at the water–membrane interface. Besides positioning the entry platform at the border between cytoplasm and membrane it could also serve as a flexible structural element and adopt different conformations with respect to the lipid membrane during the enzymatic cycle, which had been shown for an equivalent helix in other P-type ATPases [77]. In this way, it could mediate conformational changes associated with copper transport. Thus, it was interesting to characterize the environment-dependent structural changes of the amphipathic helix MBb as such in order to explore the "conformational space" that can be occupied by this prominent structure element of P_{IB}-type ATPases.

In a simplistic approach, a synthetic model peptide of helix MBb with the sequence GWPFFKRGWQSLK was studied. Structural changes induced by the helicity-promoting solvent trifluoroethanol (TFE) or lipid vesicles were monitored using CD spectroscopy as well as Fourier-transform infrared (FT-IR) spectroscopy and the changes in the polarity of the environment upon lipid interaction were monitored by intrinsic tryptophan fluorescence. The

spectroscopic data presented in this chapter were collected in the course of a bachelor thesis (Lennart Gaus, TU Dresden, 2014) that I co-supervised as a part of my doctoral work.

5.2. Results

5.2.1. Interaction of the MBb peptide with the helicity-promoting solvent TFE

2,2,2-Trifluoroethanol (TFE) is an isotropic solvent with a relative permittivity of approximately 27 [147], resembling in this respect the lipid head group region [148]. In TM peptide research it is often used as a crude membrane-mimetic system. As suggested by molecular dynamic simulations, TFE induces secondary structure by accumulating around the peptide and thus limiting water access to the peptide backbone [149]. Thereby, external hydrogen bond donors and acceptors are reduced so that intramolecular hydrogen bonds and consequently secondary structure formation is favored. Thus, it was obvious to study the impact of TFE on the amphipathic peptide MBb.

Tryptophan fluorescence of MBb at varying TFE concentrations. The intensity-normalized emission spectra of tryptophan at varying TFE contents are shown in Figure 5.1 A. Clearly, TFE induces a blue shift of the emission maximum. In pure aqueous buffer λ_{max} is 359 nm. In almost pure TFE (97.5% v/v) λ_{max} is shifted to 351 nm. This observation is not surprising and represents the isotropic change in the dielectricity of the tryptophan environment. Furthermore, it can be assumed that a similar shift of tryptophan emission occurs upon interaction of MBb with a hydrophobic lipid bilayer.

Secondary structure of MBb at varying TFE concentrations. The changes in the secondary structure of MBb at different TFE concentrations were studied by CD spectroscopy (see Figure 5.1 B). TFE induces a significant change of the shape of the CD spectrum. In aqueous buffer, the MBb shows a characteristic random coil spectrum featuring an intense minimum at 199 nm and a weak maximum at 223 nm [150]. Upon increasing the TFE concentration to 89%, the signal minimum shifts to 206 nm and the signal maximum at 223 nm disappears.

Instead, a maximum at 193 nm develops. As no satisfying fit for secondary structure fractions of MBb using standard methods (CDSSTR, SELCON, etc.) was obtained, the spectra were compared qualitatively to reference spectra that are specifically appropriate for short polypeptides [150]. While MBb adopts a clear random coil conformation in aqueous buffer, TFE addition induces structural changes towards a helical structure. However, the most prominent feature of an α-helical structure, the signal minimum at 222 nm [114] does not evolve. Thus, even at the highest TFE concentration, MBb seems to be partly in a random coil structure. This implies that on the one hand, structure induction by reduction of external hydrogen bonds by TFE is not sufficient to force MBb into the helical conformation which it adopts in the context of the full length protein according to the crystal structure. On the other hand, this indicates that MBb is not α-helical *per se* but can rather adopt different structures according to its environment. This suggests that MBb may act as a variable protein element that adopts different conformations in the enzymatic cycle of *Lp*CopA.

A

B
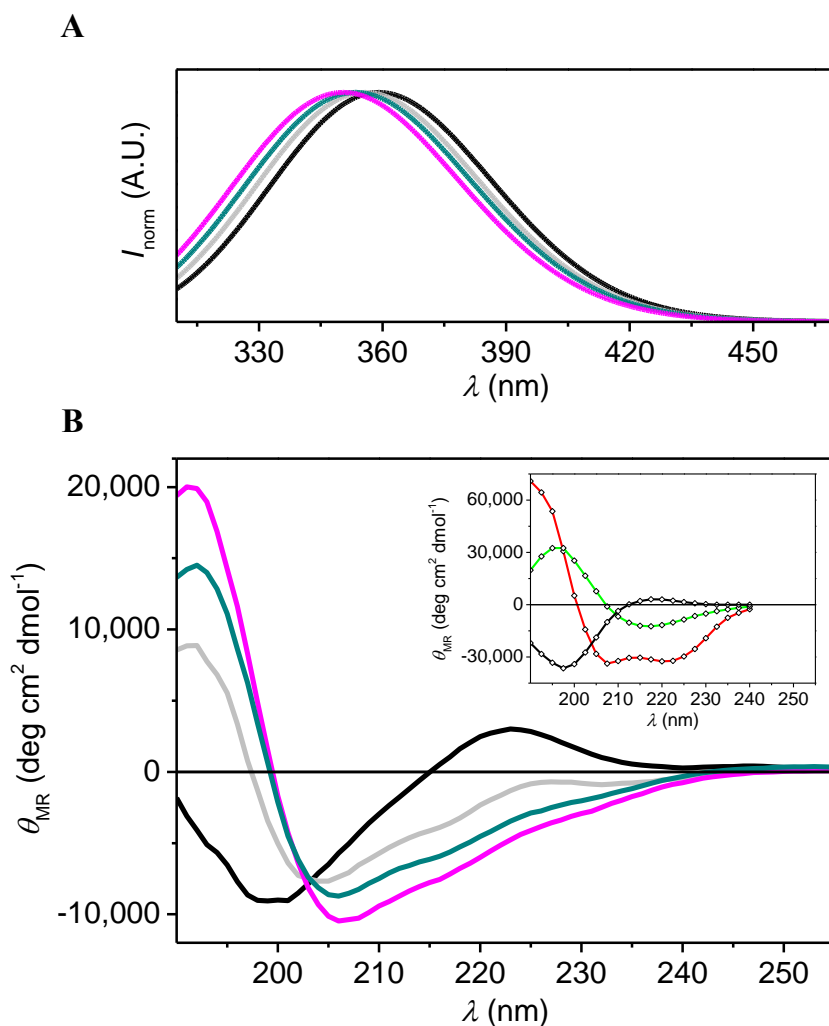
Figure 5.1: Interaction of the peptide MBb with TFE. (**A**) Steady-state fluorescence spectra (log-normal fits) of MBb in Tris-SO$_4$ buffer without TFE (black) and with 25 (gray), 75 (teal) and 97.5% TFE (magenta) The peptide concentration was 10 µM (**B**) CD spectra of MBb in Tris-SO$_4$ buffer without TFE and with 10 (blue), 25 (gray), 75 (teal) , and 89% TFE (magenta). The peptide concentration was 50 µM. **Insert**: Reference spectra of model peptides representing the three main secondary structures alpha helix (red), beta sheet (green) and random coil (black). The reference spectra are taken from [150].

## 5.2.2.   Interaction of the MBb peptide with lipid vesicles

TFE is a poor mimic of the lipid membrane as it provides only an isotropic environment. However, the lipid membrane is clearly anisotropic and characterized by pronounced changes in dielectricity along the membrane normal, with values from 80 for the bulk water phase to 0 for the center of the membrane. Thus, an amphipathic polypeptide which is located at the membrane–water interface experiences a high degree of anisotropy. In amphipathic polypeptides hydrophobic residues and hydrophilic residues are usually distributed alternately

over the sequence. Hydrophobic residues point towards the lipids and the hydrophilic charged or polar residues are directed towards the aqueous phase. When the appropriate sequence is given, an α-helical structure allows satisfying the internal and external hydrogen bonds to the best possible extent and is therewith energetically most favorable. Thus, the interaction of MBb with large unilamellar vesicles (LUVs) of POPC was also studied in order to model the native environment of the MBb sequence at the water–membrane interface in the full length *Lp*CopA.

Tryptophan fluorescence of MBb upon interaction with POPC liposomes. As can be seen in the intensity normalized fluorescence emission spectra, liposome addition results in a blue shift of the emission maximum indicating that the peptide MBb binds to the liposomes (Figure 5.2 A). The emission maximum shifts by 9 nm to 350 nm at the highest lipid concentration of 1700 µM. No saturation of λ_{max} is observed, indicating that not all peptide is bound to the liposomes. Thus, assuming a two-state model of interaction, the spectrum at a certain lipid concentration represents two peptide species: a liposome-bound species (denoted as "bound peptide") and a species in aqueous buffer. Hence, the total spectrum can be understood as a superposition of the particular spectra of these peptide species. However, the spectrum for fully bound peptide could not be obtained experimentally and thus fully-bound MBb was mimicked by dissolving MBb in the very apolar solvent mixture of methanol : chloroform 20:80 v/v, which has a calculated dielectric constant of 10.4. Then, spectra representing fractions of bound peptide from 0 to 1 in steps of 0.1 were calculated from the spectrum in aqueous buffer (representing free peptide, *fp*) and in the methanol : chloroform mixture (representing bound peptide, *bp*) according to

$$I(\lambda) = I_{bp}(\lambda) \cdot f_{bp} + I_{fp}(\lambda) \cdot (1 - f_{bp}) \tag{5.1}$$

with $I(\lambda)$ being the wavelength dependent intensity of the calculated spectrum and $I_{bp}(\lambda)$ and $I_{fp}(\lambda)$ the corresponding intensities for bound and free peptide, respectively and f_{bp} the fraction of bound peptide. The obtained calibration curve is shown in Figure 5.2 B.

A

B
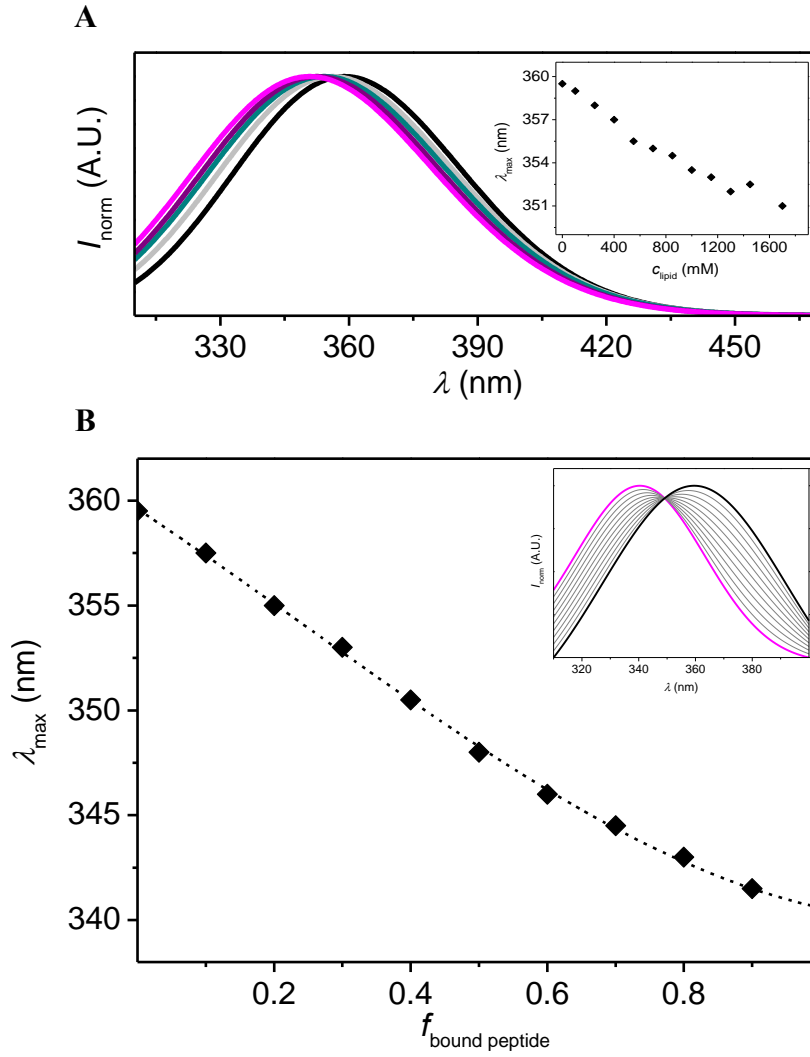
Figure 5.2: Interaction of MBb with POPC-liposomes monitored by tryptophan fluorescence. (**A**) Steady-state fluorescence spectra (log-normal fits) of MBb in Tris-SO$_4$ buffer. The peptide concentration was 5 µM. Lipid concentrations were 0 (black), 400 (gray), 700 (teal), 1000 (purple), and 1700 µM (magenta). **Insert**: Correlation between the maximum emission λ_{max} and the concentration of lipid c_{lipid}. (**B**) Calibration curve relating λ_{max} with the fraction f of bound peptide. The reference spectra for free and completely bound peptide MBb, were recorded in aqueous buffer and in methanol : chloroform 20:80 v/v, respectively. The spectra at intermediate fraction of bound peptide were calculated from linear combinations of the two extreme spectra (see **insert**).

Determination of a Langmuir adsorption isotherm. With the help of the described calibration it is possible extract a Langmuir adsorption isotherm from the experimental spectra. The concentration of free peptide c_{fp} is related to the dissociation constant K according to

$$c_{fp} = K \cdot \frac{L}{1-L} \tag{5.2}$$

with L being the fractional saturation of lipid binding sites. The total peptide concentration c_p is constant so that

$$c_{\text{fp}} = c_{\text{p}} - c_{\text{bp}} \qquad (5.3)$$

On the other hand, the concentration of bound peptide c_{bp} is also related to lipid concentration c_{lipid} by

$$c_{\text{bp}} = L \cdot c_{\text{lipid}} \qquad (5.4)$$

so that one can rewrite

$$c_{\text{lipid}} = \frac{1}{L} \cdot \left(c_{\text{p}} - K \cdot \frac{L}{1-L} \right). \qquad (5.5)$$

With the help of the calibration curve described in the last section, the emission maxima λ_{max} of the spectra were related to the fraction of bound peptide f_{bp}, which equals $c_{\text{bp}}/c_{\text{p}}$. Thus, the Langmuir adsorption isotherm can be obtained from plotting f_{bp} against the lipid concentration c_{lipid} (see Figure 5.3) and fitting the dissociation constant K as a free parameter. The obtained large dissociation constant of $K = 2.9$ mM indicates a low affinity between peptide and lipid. Clearly, the low affinity does not result from the occupation of the liposome surface. Rather it is conceivable, that the low affinity is caused by electrostatic repulsion between free and bound peptide caused by positively charged residues. A more thorough analysis would be possible by applying the Gouy-Chapman theory, but was not undertaken within the scope of this work. Importantly, also these results on the interaction of MBb with a lipid membrane indicate that this stretch of *Lp*CopA might be flexible and not stationary bound to the lipid membrane.
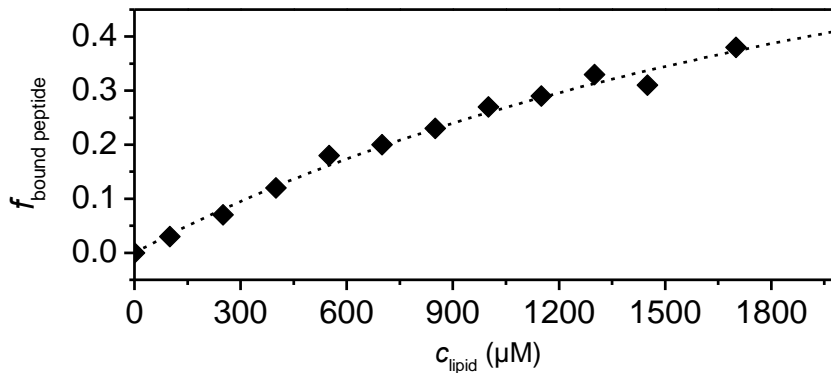
Figure 5.3: Langmuir adsorption isotherm of the peptide MBb to lipid vesicles. The fraction of lipid-bound peptide f_{bp} *versus* lipid concentration c_{lipid} is plotted. The dissociation constant derived from the adsorption isotherm fit is $K = 2.9$ mM.

Structure formation of MBb upon POPC interaction. The experiments described above were based on tryptophan emission only and confirm the fundamental property of the amphipathic MBb sequence to associate with the lipid surface through partial insertion of hydrophobic side chains (here tryptophan) into the lipid phase. However, it cannot be concluded from these experiments whether the presumed α-helical structure forms during this process. Therefore, it was also investigated if the interaction of MBb with lipids induces structure formation. Figure 5.4 A shows the CD spectra of MBb upon titration with POPC liposomes. No significant changes in secondary structure were observed. However, this is not surprising when considering the seven times lower lipid to peptide ratio in the CD data as compared to the fluorescence data that was a consequence of the higher peptide concentration. Unfortunately, high noise due to light scattering from the POPC vesicles hampered spectra acquisition at higher lipid concentrations. Using the Langmuir adsorption isotherm (see Figure 5.3) the maximal fraction of bound peptide f_{bp} was estimated to be only about 10% at the highest lipid to peptide ratio measured. As an approach to explore structure formation of MBb under conditions that would favor the interaction of the peptide with lipid, the system was studied in a hydrated rather than suspended state. To this end, the FT-IR spectra were recorded, which allow direct observation of secondary structure-sensitive vibrations of the peptide backbone. Figure 5.4 B shows the transmission spectra of MBb in the absence and in the presence of POPC. For pure MBb, the amide I band, representing the C=O stretching mode of the peptide bonds, shows a maximum at 1,652 cm^{-1}. This frequency is typical for a partly random coiled and partly α-helical structure. When mixed with lipid, the amide I band shifts to 1,656 cm^{-1} which is indicative of the formation of α-helical structure. Thus, it can be expected that helical structure formation of MBb is favored in the context of the full length *Lp*CopA protein, where the sequence element is structurally restrained to interact with the lipid membrane through its localization between the adjacent TM helices M1 and the N-terminal part of MB.
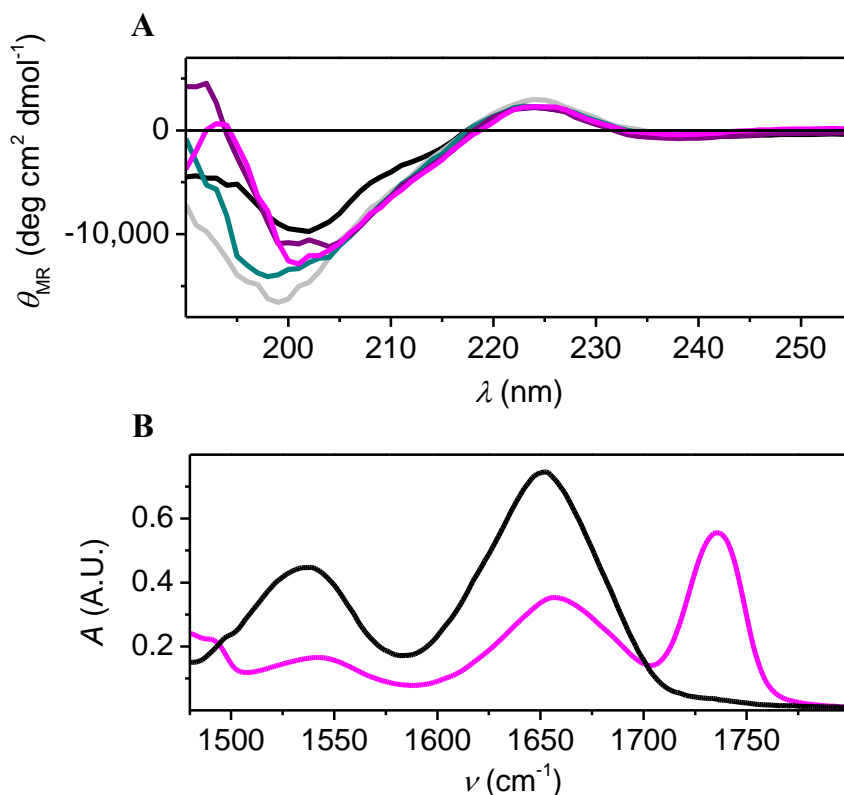
Figure 5.4: Structure formation of MBb upon lipid interaction. (**A**) CD spectra of MBb in Tris-SO$_4$ buffer. The peptide concentration was 35 µM. The lipid concentration was 0 (black), 250 (gray), 600 (teal), 1000 (purple), and 1500 µM (magenta). (**B**) FT-IR absorption spectrum of MBb in the absence and in the presence of POPC liposomes. 11 µmole MBb in Tris-SO$_4$ buffer (black) and in POPC (magenta) were used. Pure MBb has an amide I vibration with a maximum at 1,652 cm^{-1}, which is typical for a partly random coil and partly α-helical structure. In the presence of lipid the amide I band shifts to 1,656 cm^{-1} which indicates the development of α-helical structure. The band at 1,736 cm^{-1} corresponds to the C=O stretching band of the phospholipid glycerol moiety.

5.3. Summary and Discussion

The entry platform to the copper transport channel of *Lp*CopA is lined by the amphipathic helix MBb which resides at the membrane–water interface and adjoins the TM helices M1 and MB. Due to its amphipathic nature, this part of *Lp*CopA may be important for the correct positioning of *Lp*CopA in the membrane. Moreover, it could serve as a flexible structural element and mediate conformational changes associated with the copper transport cycle. The results, gathered by a combination of CD, FT-IR and intrinsic tryptophan fluorescence spectroscopy, revealed that the synthetic peptide of MBb has no strong intrinsic

helicity when it is dissolved in an aqueous phase. In the low dielectric solvent TFE – where internal hydrogen bonds are favored – structure is formed. However, no complete α-helical fold is attained, as shown by CD spectroscopy. In contrast, FT-IR spectroscopy shows that MBb has an α-helical structure when it is brought into contact with a lipid layer under dehydrated conditions, i.e. when re-partitioning into the aqueous phase is prevented. However, a Langmuir adsorption isotherm derived from the intrinsic tryptophan fluorescence spectra of MBb in the presence of lipid vesicles revealed that MBb has only a low affinity to the neutral lipid POPC.
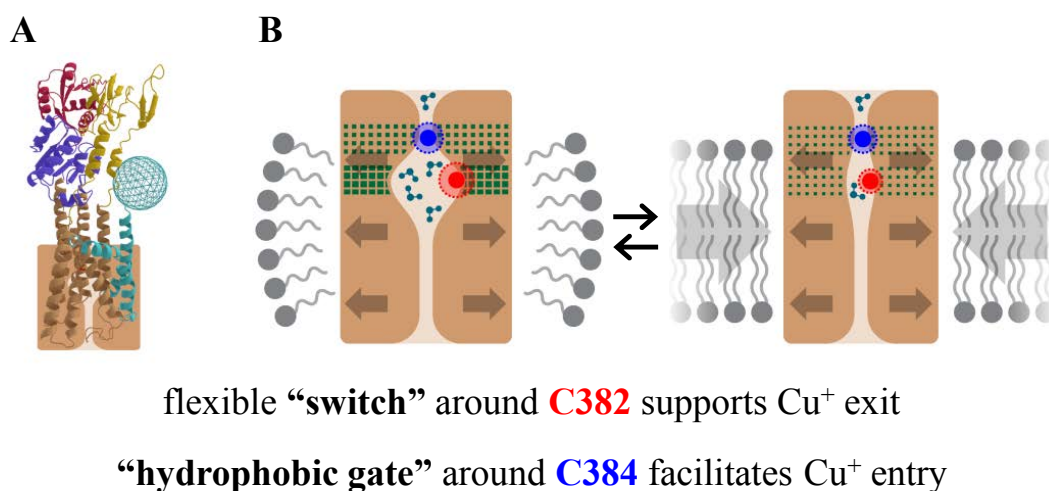
Taken together these results indicate that the α-helical structure seen in the crystal structure is not necessarily an intrinsic property of MBb. Instead, the MBb sequence is to some extent anchored to the membrane surface through the adjacent TM helices, and thereby stabilized in its helical structure by forced lipid interactions [64]. In this way the hydrophobic and hydrophilic amino acid side chains orient in an energetically favorable way between the membrane end the aqueous environment, respectively [151]. Consequently, this work can confirm the α-helical structure in the context of *Lp*CopA but shows that the amino acid sequence itself does not strictly encode for this type of secondary structure, even though the peptide shows the typical sequence features of an amphipathic helix [13]. Thus, dielectric and geometric factors inherent to the water–lipid phase boundary could be crucial factors in regulating structural transitions during the highly dynamic ion transport process through *Lp*CopA. For example it could be involved in rearrangements of helix M1 and therewith of M148 that probably participates in initial copper coordination. For translocation of the ion to the copper binding site CPC on helix M4, helix M1 and helix M4 need to slide along each other to the extracellular and intracellular side, respectively [47, 68]. Such a movement of helix M1 could be facilitated by a change in the membrane orientation and/or structure of the adjacent amphipathic helix MBb.

6. Conclusions and perspectives

The Cu^+-transporting P_{IB}-type ATPase *Lp*CopA is a prominent member of the diverse ion pump family of P-type ATPases. This ubiquitous transmembrane protein and its homologues are vital for regulating copper levels in humans, bacteria, and plants. The ion transport mechanism of this transmembrane pump has unique features in terms of the ion entry and exit steps and its study holds great potential to gain a deeper understanding of the role of protein–lipid interactions and the role of water dynamics for membrane protein function.

In this work, the role of intra-protein hydration during the transport cycle was studied in a dynamic solution state of the protein and the influence of the lipid environment was addressed. To this end, the functional recombinant protein was purified in a detergent-solubilized state and reconstituted into MSP1E3D1-nanodiscs, which was the first reported successful reconstitution of a P_{IB}-ATPase into this versatile nano-scaled planar lipid bilayer system. Site-specific fluorescence spectroscopic studies using the small polarity-sensitive dye BADAN allowed probing polarity and water mobility in a radius of approximately 5 Å around the residues of the central copper-binding motif CPC on TM helix M4. It is assumed that copper is initially coordinated by C384 together with M148 and other low-affinity residues, while conformational changes lead to its high-affinity binding at C384, C382, and M717 on helix M6. Further TM helix rearrangements are necessary for the extrusion of the ion to the extracellular side and water networks in the TM channel could play an important role for this step. In this work it could be shown that the environment of the copper binding site is characterized by strong polarity gradients and that the lipid environment plays a crucial role in determining intra-protein hydration around the buried and conserved residue C382. Quantitative analysis of the fluorescence spectra showed that the constraints imposed by the lipid bilayer lead both to the exclusion as well as to the immobilization of water at this intramembranous site, while the hydration is little altered around C384. It can be proposed that the environment of C384 serves as a "hydrophobic gate" where the hydration shell of the Cu^+-ion is partially stripped off to enable its binding to the protein and its back-diffusion to the cytoplasm is prevented. The relatively narrow and rigid character of the entry

channel as expected for a "hydrophobic gate" is also supported by the fact that BADAN labeling at the more cytoplasmic C384 led to the steric hindrance of further labeling at C382 as observed for cmCopA bearing the native CPC motif. The remarkable hydration in the environment of C382 points to its role for the re-solvation of the Cu$^+$-ion in order to prime it for extrusion to the luminal side of the membrane. However, the dependence of the hydration properties on the constraints of a lipidic environment indicates the flexibility of this site. This flexibility could also be partly mediated by rearrangements of the adjacent amphipathic helix MBb which in this work was found to exhibit lipid-dependent structural variability. MBb is located at the cytoplasmic entry platform to the copper channel adjacent to helix M1, which is neighboring the CPC motif-bearing helix M4. Thus, the environment of C382 might constitute a default "switch" as part of the ATP-driven enzymatic reaction cycle. Figure 6.1 shows a schematic representation of the proposed model.

A   B

flexible **"switch"** around **C382** supports Cu$^+$ exit

"hydrophobic gate" around **C384** facilitates Cu$^+$ entry

Figure 6.1: Schematic model of the proposed role of C382 and C384 for the ion transport mechanism of *Lp*CopA. (**A**) Overview of the *Lp*CopA structure with highlighted TM domain. (**B**) Model of lipid-mediated hydration changes in the TM domain of *Lp*CopA. The fractions f_m of mobile water are indicated by the size of the halo around the residues. The density of the green pattern symbolizes the dielectricity in the environment of the probed sites. The environment of C384 has a moderate polarity that is largely unaffected by the lipid environment. Thus, it may act as a "hydrophobic gate" during the initial copper coordination, facilitating the stripping of the ion hydration shell. The environment of membrane-buried residue C382 is characterized by a high fraction of mobile water in the flexible detergent micelle (**left hand side**), while membrane reconstitution leads to the exclusion and immobilization of water (**right hand side**). Thus, this site may act as a flexible conformational "switch" facilitating the ion extrusion. The model suggests a functional role of the lateral pressure as a restoring force that dehydrates the C382 environment during the catalytic cycle when the ion is released to the extracellular opening.

The functional reconstitution of *Lp*CopA into the native lipid environment of the nanodiscs established a platform that will be of great use in the future. One exciting perspective is to "change the point of view" and study the environment of the protein-bound ion with the help of advanced element-specific X-ray spectroscopic techniques at X-ray free-electron lasers (X-FELs). Here, nanodiscs constitute a perfectly suited system to deliver the membrane protein in a native lipid environment to the intense pulsed X-ray beam and could enable the collection of single particle diffraction patterns before sample destruction. Preliminary experiments could already show that diffraction patterns of intact nanodiscs can be recorded in an X-FEL beam (CXI beamline at LCLS in cooperation with Anton Barthy, unpublished data). In this context, mutation of the ion-binding protein residues could dissect the roles of the "protein scaffold" and the ligands involved in ion coordination [152]. This knowledge could be fundamental in the process of engineering transmembrane ion pumps with altered ion specificity. For example, it is conceivable that the flexible and hydrated interior of the *Lp*CopA TM channel could be a suitable environment for actinides and lanthanides due to their large hydration shell, once the thiol-base ligands are substituted by carboxylates. Creating such an engineered transporter would be a milestone of biotechnological research.

Altogether, the results gathered throughout this work stress the paramount importance of the lipid bilayer for membrane protein function and especially address the question how dynamic intra-protein hydration is interlinked with the conformational flexibility of the membrane protein during function. Such questions cannot be addressed through the study of "frozen" crystal states. Thus, spectroscopic research on dynamic membrane proteins with the option of particularly studying the role of the native bilayer environment is a powerful way to follow vital structural transitions that will ultimately contribute to decipher the riddles of protein structure–function relationships.

7. References

1. Alberts, B., *Molecular Biology of the Cell 5th Edition*. 2008: Garland Science New York.

2. von Heijne, G., *The Membrane Protein Universe: What's out There and Why Bother?* J Intern Med, 2007. **261**(6): p. 543-557.

3. Mueller, P., *Molecular Aspects of Electrical Excitation in Lipid Bilayers and Cell Membranes.* Horiz Biochem Biophys, 1976. **2**: p. 230-284.

4. Hille, B., *Ionic Channels: Molecular Pores of Excitable Membranes.* Harvey Lect, 1986. **82**: p. 47-69.

5. Pardee, A.B., *Biochemical Studies on Active Transport.* J Gen Physiol, 1968. **52**(1): p. 279-295.

6. Gadsby, D.C., *Ion Channels Versus Ion Pumps: The Principal Difference, in Principle.* Nat Rev Mol Cell Biol, 2009. **10**(5): p. 344-352.

7. Wallin, E. and von Heijne, G., *Genome-Wide Analysis of Integral Membrane Proteins from Eubacterial, Archaean, and Eukaryotic Organisms.* Protein Sci, 1998. **7**(4): p. 1029-1038.

8. Hopkins, A.L. and Groom, C.R., *The Druggable Genome.* Nat Rev Drug Discov, 2002. **1**(9): p. 727-730.

9. Pieper, U., et al., *Coordinating the Impact of Structural Genomics on the Human Alpha-Helical Transmembrane Proteome.* Nat Struct Mol Biol, 2013. **20**(2): p. 135-138.

10. Meer, G.V., Voelker, D., and Feigenson, G., *Membrane Lipids: Where They Are and How They Behave.* Nat Rev Mol Cell Biol, 2008. **9**(2): p. 112-124.

11. Lee, A.G., *How Lipids Affect the Activities of Integral Membrane Proteins.* Biochim Biophys Acta, 2004. **1666**(1-2): p. 62-87.

12. Nyholm, T.K., Ozdirekcan, S., and Killian, J.A., *How Protein Transmembrane Segments Sense the Lipid Environment.* Biochemistry, 2007. **46**(6): p. 1457-1465.

13. Killian, J.A. and von Heijne, G., *How Proteins Adapt to a Membrane-Water Interface.* Trends Biochem Sci, 2000. **25**(9): p. 429-434.

14. Hristova, K., et al., *An Amphipathic Alpha-Helix at a Membrane Interface: A Structural Study Using a Novel X-Ray Diffraction Method.* J Mol Biol, 1999. **290**(1): p. 99-117.

15. White, S.H. and Wimley, W.C., *Hydrophobic Interactions of Peptides with Membrane Interfaces.* Biochim Biophys Acta, 1998. **1376**(3): p. 339-352.

16. Soubias, O. and Gawrisch, K., *The Role of the Lipid Matrix for Structure and Function of the GPCR Rhodopsin.* Biochim Biophys Acta, 2012. **1818**(2): p. 234-240.

17. Wood, K., et al., *Coupling of Protein and Hydration-Water Dynamics in Biological Membranes.* Proc Natl Acad Sci U S A, 2007. **104**(46): p. 18049-18054.

18. Bondar, A.N. and White, S.H., *Hydrogen Bond Dynamics in Membrane Protein Function.* Biochim Biophys Acta, 2012. **1818**(4): p. 942-950.

19. Yang, J., Aslimovska, L., and Glaubitz, C., *Molecular Dynamics of Proteorhodopsin in Lipid Bilayers by Solid-State NMR.* J Am Chem Soc, 2011. **133**(13): p. 4874-4881.

20. Grossfield, A., et al., *Internal Hydration Increases During Activation of the G-Protein-Coupled Receptor Rhodopsin.* J Mol Biol, 2008. **381**(2): p. 478-486.

21. Seddon, A.M., Curnow, P., and Booth, P.J., *Membrane Proteins, Lipids and Detergents: Not Just a Soap Opera.* Biochim Biophys Acta, 2004. **1666**(1-2): p. 105-117.

22. Zhou, H.X. and Cross, T.A., *Influences of Membrane Mimetic Environments on Membrane Protein Structures.* Annu Rev Biophys, 2013. **42**: p. 361-392.

23.   Bowie, J.U., *Stabilizing Membrane Proteins.* Curr Opin Struct Biol, 2001. **11**(4): p. 397-402.

24.   Hofmann, K.P., et al., *A G Protein-Coupled Receptor at Work: The Rhodopsin Model.* Trends Biochem Sci, 2009. **34**(11): p. 540-552.

25.   Bayburt, T.H., Grinkova, Y.V., and Sligar, S.G., *Self-Assembly of Discoidal Phospholipid Bilayer Nanoparticles with Membrane Scaffold Proteins.* Nano Letters, 2002. **2**(8): p. 1-4.

26.   Nath, A., Atkins, W.M., and Sligar, S.G., *Applications of Phospholipid Bilayer Nanodiscs in the Study of Membranes and Membrane Proteins.* Biochemistry, 2007. **46**(8): p. 2059-2069.

27.   Denisov, I. and McLean, M., *Thermotropic Phase Transition in Soluble Nanoscale Lipid Bilayers.* J Phys Chem B, 2005. **109**(32): p. 15580-15588.

28.   Karasawa, A., et al., *Physicochemical Factors Controlling the Activity and Energy Coupling of an Ionic Strength-Gated ABC Transporter.* J Biol Chem, 2013. **288**(41): 29862-29871.

29.   Axelsen, K.B. and Palmgren, M.G., *Evolution of Substrate Specificities in the P-Type ATPase Superfamily.* Journal of Molecular Evolution, 1998. **46**(1): p. 84-101.

30.   Benarroch, E.E., *Na^+, K^+-ATPase: Functions in the Nervous System and Involvement in Neurologic Disease.* Neurology, 2011. **76**(3): p. 287-293.

31.   Periasamy, M. and Kalyanasundaram, A., *Serca Pump Isoforms: Their Role in Calcium Transport and Disease.* Muscle Nerve, 2007. **35**(4): p. 430-442.

32.   Sachs, G., et al., *The Gastric H,K ATPase as a Drug Target: Past, Present, and Future.* J Clin Gastroenterol, 2007. **41 Suppl 2**: p. S226-242.

33.   Gaballa, A. and Helmann, J.D., *Bacillus Subtilis Cpx-Type ATPases: Characterization of Cd, Zn, Co and Cu Efflux Systems.* Biometals, 2003. **16**(4): p. 497-505.

34.   Mills, R.F., et al., *The Plant P_{IB}-Type ATPase AtHMA4 Transports Zn and Cd and Plays a Role in Detoxification of Transition Metals Supplied at Elevated Levels.* FEBS Lett, 2005. **579**(3): p. 783-791.

35.   Yatime, L., et al., *P-Type ATPases as Drug Targets: Tools for Medicine and Science.* Biochim Biophys Acta, 2009. **1787**(4): p. 207-220.

36.   Seto-Young, D., et al., *Exploring an Antifungal Target in the Plasma Membrane H^+-ATPase of Fungi.* Biochim Biophys Acta, 1997. **1326**(2): p. 249-256.

37.   Serrano, R., Kielland-Brandt, M.C., and Fink, G.R., *Yeast Plasma Membrane ATPase Is Essential for Growth and Has Homology with (Na^+,K^+), K^+- and Ca^{2+}-ATPases.* Nature, 1986. **319**(6055): p. 689-693.

38.   MacLennan, D.H., et al., *Amino-Acid Sequence of a Ca^{2+} + Mg^{2+}-Dependent ATPase from Rabbit Muscle Sarcoplasmic Reticulum, Deduced from Its Complementary DNA Sequence.* Nature, 1985. **316**(6030): p. 696-700.

39.   Palmgren, M.G. and Nissen, P., *P-Type ATPases.* Annu Rev Biophys, 2011. **40**: p. 243-266.

40.   Møller, J.V., et al., *The Sarcoplasmic Ca^{2+}-ATPase: Design of a Perfect Chemi-Osmotic Pump.* Q Rev Biophys, 2010. **43**(4): p. 501-566.

41.   Argüello, J.M., *Identification of Ion-Selectivity Determinants in Heavy-Metal Transport P_{IB}-Type ATPases.* J Membr Biol, 2003. **195**(2): p. 93-108.

42.   Jardetzky, O., *Simple Allosteric Model for Membrane Pumps.* Nature, 1966. **211**(5052): p. 969-970.

43. Post, R.L. and Sen, A.K., *An Enzymatic Mechanism of Active Sodium and Potassium Transport.* J Histochem Cytochem, 1965. **13**: p. 105-112.

44. Albers, R.W., Fahn, S., and Koval, G.J., *The Role of Sodium Ions in the Activation of Electrophorus Electric Organ Adenosine Triphosphatase.* Proc Natl Acad Sci U S A, 1963. **50**: p. 474-481.

45. Olesen, C., et al., *The Structural Basis of Calcium Transport by the Calcium Pump.* Nature, 2007. **450**(7172): p. 1036-1042.

46. Niggli, V. and Sigel, E., *Anticipating Antiport in P-Type ATPases.* Trends Biochem Sci, 2008. **33**(4): p. 156-160.

47. Andersson, M., et al., *Copper-Transporting P-Type ATPases Use a Unique Ion-Release Pathway.* Nat Struct Mol Biol, 2014. **21**(1): p. 43-48.

48. Kaplan, J.H., *Biochemistry of Na,K-ATPase.* Annu Rev Biochem, 2002. **71**: p. 511-535.

49. Klein, J.S. and Lewinson, O., *Bacterial ATP-Driven Transporters of Transition Metals: Physiological Roles, Mechanisms of Action, and Roles in Bacterial Virulence.* Metallomics, 2011. **3**(11): p. 1098-1108.

50. Haferburg, G. and Kothe, E., *Metallomics: Lessons for Metalliferous Soil Remediation.* Appl Microbiol Biotechnol, 2010. **87**(4): p. 1271-1280.

51. Tapiero, H., Townsend, D.M., and Tew, K.D., *Trace Elements in Human Physiology and Pathology. Copper.* Biomedicine & Pharmacotherapy, 2003. **57**(9): p. 386-398.

52. Tapiero, H. and Tew, K.D., *Trace Elements in Human Physiology and Pathology: Zinc and Metallothioneins.* Biomedicine & Pharmacotherapy, 2003. **57**(9): p. 399-411.

53. Collins, J.F., Prohaska, J.R., and Knutson, M.D., *Metabolic Crossroads of Iron and Copper.* Nutr Rev, 2010. **68**(3): p. 133-147.

54. Prohaska, J.R., *Role of Copper Transporters in Copper Homeostasis.* Am J Clin Nutr, 2008. **88**(3): p. 826S-829S.

55. Boal, A. and Rosenzweig, A., *Structural Biology of Copper Trafficking.* Chem Rev, 2009. **109**(10): p. 4760-4779.

56. Zumft, W.G., Viebrock-Sambale, A., and Braun, C., *Nitrous Oxide Reductase from Denitrifying Pseudomonas Stutzeri. Genes for Copper-Processing and Properties of the Deduced Products, Including a New Member of the Family of ATP/GTP-Binding Proteins.* Eur J Biochem, 1990. **192**(3): p. 591-599.

57. Higgins, C.F., *ABC Transporters: From Microorganisms to Man.* Annu Rev Cell Biol, 1992. **8**: p. 67-113.

58. Odermatt, A., et al., *Primary Structure of Two P-Type ATPases Involved in Copper Homeostasis in Enterococcus Hirae.* J Biol Chem, 1993. **268**(17): p. 12775-12779.

59. Tottey, S., et al., *Two Menkes-Type ATPases Supply Copper for Photosynthesis in Synechocystis Pcc 6803.* J Biol Chem, 2001. **276**(23): p. 19999-20004.

60. Wunderli-Ye, H. and Solioz, M., *Purification and Functional Analysis of the Copper ATPase CopA of Enterococcus Hirae.* Biochem Biophys Res Commun, 2001. **280**: p. 713-719.

61. Su, C.C., Long, F., and Yu, E.W., *The Cus Efflux System Removes Toxic Ions Via a Methionine Shuttle.* Protein Sci, 2011. **20**(1): p. 6-18.

62. Mana-Capelli, S., Mandal, A.K., and Argüello, J.M., *Archaeoglobus Fulgidus CopB Is a Thermophilic Cu^{2+}-ATPase: Functional Role of Its Histidine-Rich-N-Terminal Metal Binding Domain.* J Biol Chem, 2003. **278**(42): p. 40534-40541.

63.   Inesi, G., *Calcium and Copper Transport ATPases: Analogies and Diversities in Transduction and Signaling Mechanisms.* J Cell Commun Signal, 2011. **5**(3): p. 227-237.

64.   Gourdon, P., et al., *Crystal Structure of a Copper-Transporting P_{IB}-Type ATPase.* Nature, 2011. **475**(7354): p. 59-64.

65.   Rosenzweig, A.C. and O'Halloran, T.V., *Structure and Chemistry of the Copper Chaperone Proteins.* Curr Opin Chem Biol, 2000. **4**(2): p. 140-147.

66.   Rosenzweig, A.C., et al., *Crystal Structure of the ATX1 Metallochaperone Protein at 1.02 Å Resolution.* Structure, 1999. **7**(6): p. 605-617.

67.   Padilla-Benavides, T., McCann, C.J., and Argüello, J.M., *The Mechanism of Cu^+-Transport ATPases: Interaction with Cu^+-Chaperones and the Role of Transient Metal-Binding Sites.* J Biol Chem, 2013. **288**: p. 69-78.

68.   Mattle, D., et al., *A Sulfur-Based Transport Pathway in Cu^+-ATPases.* EMBO Rep, 2015. **16**(6): p.728-740

69.   Gourdon, P., et al., *Structural Models of the Human Copper P-Type ATPases ATP7A and ATP7B.* Biological Chemistry, 2012. **393**(4): p. 205-216.

70.   Bal, N., et al., *A Possible Regulatory Role for the Metal-Binding Domain of CadA, the Listeria Monocytogenes Cd^{2+}-ATPase.* FEBS Lett, 2001. **506**(3): p. 249-252.

71.   Wu, C.-C., Rice, W.J., and Stokes, D.L., *Structure of a Copper Pump Suggests a Regulatory Role for Its Metal-Binding Domain.* Structure, 2008. **16**(6): p. 976-985.

72.   Wernimont, A.K., et al., *Structural Basis for Copper Transfer by the Metallochaperone for the Menkes/Wilson Disease Proteins.* Nat Struct Biol, 2000. **7**(9): p. 766-771.

73.   von Heijne, G., *The Distribution of Positively Charged Residues in Bacterial Inner Membrane Proteins Correlates with the Transmembrane Topology.* EMBO J, 1986. **5**(11): p. 3021-3027.

74.   Banci, L., et al., *Copper(I)-Mediated Protein-Protein Interactions Result from Suboptimal Interaction Surfaces.* Biochem J, 2009. **422**(1): p. 37-42.

75.   Segrest, J.P., et al., *A Molecular Theory of Lipid-Protein Interactions in the Plasma Lipoproteins.* FEBS Lett, 1974. **38**(3): p. 247-258.

76.   Pedersen, B.P., et al., *Crystal Structure of the Plasma Membrane Proton Pump.* Nature, 2007. **450**(7172): p. 1111-1114.

77.   Thøgersen, L. and Nissen, P., *Flexible P-Type ATPases Interacting with the Membrane.* Curr Opin Struct Biol, 2012. **22**(4): p. 491-499.

78.   Bousché, O., et al., *Vibrational Spectroscopy of Bacteriorhodopsin Mutants. Evidence that Asp-96 Deprotonates During the M-N Transition.* J Biol Chem, 1991. **266**(17): p. 11063-11067.

79.   Khorana, H.G., *Bacteriorhodopsin, a Membrane Protein That Uses Light to Translocate Protons.* J Biol Chem, 1988. **263**(16): p. 7439-7442.

80.   Oiki, S., Madison, V., and Montal, M., *Bundles of Amphipathic Transmembrane Alpha-Helices as a Structural Motif for Ion-Conducting Channel Proteins: Studies on Sodium Channels and Acetylcholine Receptors.* Proteins, 1990. **8**(3): p. 226-236.

81.   Pearson, R.B., *Hard and Soft Acids and Bases* J Am Chem Soc, 1963. **85**(22): p. 3533-3539.

82.   González-Guerrero, M., et al., *Structure of the Two Transmembrane Cu^+-Transport Sites of the Cu^+-ATPases.* J Biol Chem, 2008. **283**(44): p. 29753-29759.

83.   Silver, S., et al., *Bacterial Resistance ATPases: Primary Pumps for Exporting Toxic Cations and Anions.* Trends Biochem Sci, 1989. **14**(2): p. 76-80.

84. Olesen, C., et al., *Dephosphorylation of the Calcium Pump Coupled to Counterion Occlusion.* Science, 2004. **306**(5705): p. 2251-2255.

85. Sørensen, T.L., Møller, J.V., and Nissen, P., *Phosphoryl Transfer and Calcium Ion Occlusion in the Calcium Pump.* Science, 2004. **304**(5677): p. 1672-1675.

86. Nagle, J.F. and Tristram-Nagle, S., *Hydrogen Bonded Chain Mechanisms for Proton Conduction and Proton Pumping.* J Membr Biol, 1983. **74**(1): p. 1-14.

87. Lewis, D., et al., *Distinctive Features of Catalytic and Transport Mechanisms in Mammalian Sarco-Endoplasmic Reticulum Ca^{2+}-ATPase (SERCA) and Cu^+-(ATP7A/B) ATPases.* J Biol Chem, 2012. **287**(39): p. 32717-32727.

88. Barry, A.N., et al., *The Lumenal Loop Met672-Pro707 of Copper-Transporting ATPase ATP7A Binds Metals and Facilitates Copper Release from the Intramembrane Sites.* J Biol Chem, 2011. **286**(30): p. 26585-26594.

89. Disalvo, E.A., et al., *Structural and Functional Properties of Hydration and Confined Water in Membrane Interfaces.* Biochim Biophys Acta, 2008. **1778**(12): p. 2655-2670.

90. Lee, A.G., *Lipid–Protein Interactions in Biological Membranes: A Structural Perspective.* Biochim Biophys Acta, 2003. **1612**(1): p. 1-40.

91. Sambrook, J. and Russell, D.W., *Molecular Cloning: A Laboratory Manual*. 2001: Cold Spring Harbor Laboratory Press 3rd Edition.

92. Inoue, H., Nojima, H., and Okayama, H., *High Efficiency Transformation of Escherichia Coli with Plasmids.* Gene, 1990. **96**(1): p. 23-28.

93. Laemmli, U.K., *Cleavage of Structural Proteins During the Assembly of the Head of Bacteriophage T4.* Nature, 1970. **227**(5259): p. 680-685.

94. Lanzetta, P.a., et al., *An Improved Assay for Nanomole Amounts of Inorganic Phosphate.* Anal Biochem, 1979. **100**(1): p. 95-97.

95. Johnson, I. and Spence, M.T.Z., *The Molecular Probes Handbook: A Guide to Fluorescent Probes and Labeling Technologies.* 2010: Invitrogen.

96. Greenfield, N.J., *Using Circular Dichroism Spectra to Estimate Protein Secondary Structure.* Nat Protoc, 2006. **1**(6): p. 2876-2890.

97. Royer, C.A., *Fluorescence Spectroscopy.* Methods Mol Biol, 1995. **40**: p. 65-89.

98. Jurkiewicz, P., et al., *Solvent Relaxation in Phospholipid Bilayers: Principles and Recent Applications.* J Fluoresc, 2005. **15**(6): p. 883-894.

99. Fee, R.S. and Maroncelli, M., *Estimating the Time-Zero Spectrum in Time-Resolved Emission Measurements of Solvation Dynamics.* Chem Phys, 1994. **183**(2-3): p. 235–247.

100. Horng, M.L., et al., *Subpicosecond Measurements of Polar Solvation Dynamics: Coumarin 153 Revisited.* J Phys Chem, 1995. **99**(48): p. 17311–17337.

101. Wagner, S., et al., *Tuning Escherichia Coli for Membrane Protein Overexpression.* Proc Natl Acad Sci U S A, 2008. **105**(38): p. 14371-14376.

102. Zoonens, M. and Miroux, B., *Expression of Membrane Proteins at the Escherichia Coli Membrane for Structural Studies.* Methods Mol Biol, 2010. **601**: p. 49-66.

103. Arnold, T. and Linke, D., *The Use of Detergents to Purify Membrane Proteins.* Current Protocols in Protein Science, 2008.

104. LaRossa, R.A. and Van Dyk, T.K., *Physiological Roles of the DnaK and GroE Stress Proteins: Catalysts of Protein Folding or Macromolecular Sponges?* Mol Microbiol, 1991. **5**(3): p. 529-534.

105. Rial, D.V. and Ceccarelli, E.A., *Removal of DnaK Contamination During Fusion Protein Purifications.* Protein Expr Purif, 2002. **25**(3): p. 503-507.

106.   Brosius, J., Erfle, M., and Storella, J., *Spacing of the -10 and -35 Regions in the Tac Promoter. Effect on its in Vivo Activity.* J Biol Chem, 1985. **260**(6): p. 3539-3541.

107.   Amann, E., Brosius, J., and Ptashne, M., *Vectors Bearing a Hybrid Trp-Lac Promoter: Useful for Regulated Expression of Cloned Genes in Escherichia Coli.* Gene, 1983. **25**(2-3): p. 167-178.

108.   Lübben, M., et al., *Sulfate Acts as Phosphate Analog on the Monomeric Catalytic Fragment of the CPx-ATPase CopB from Sulfolobus Solfataricus.* J Mol Biol, 2007. **369**(2): p. 368-385.

109.   Strop, P. and Brunger, A.T., *Refractive Index-Based Determination of Detergent Concentration and Its Application to the Study of Membrane Proteins.* Protein Sci, 2005. **14**(8): p. 2207-2211.

110.   Bayburt, T.H. and Sligar, S.G., *Membrane Protein Assembly into Nanodiscs.* FEBS Lett, 2010. **584**(9): p. 1721-1727.

111.   Alvarez, F.J.D. and Davidson, A.L., *Functional Reconstitution of an ABC Transporter in Nanodiscs for Use in Electron Paramagnetic Resonance Spectroscopy.* J Am Chem Soc, 2010. **132**(28): p. 9513-9515.

112.   Shenkarev, Z.O., et al., *Lipid-Protein Nanodiscs Promote in Vitro Folding of Transmembrane Domains of Multi-Helical and Multimeric Membrane Proteins.* Biochim Biophys Acta, 2013. **1828**(2): p. 776-784.

113.   Finkenwirth, F., et al., *ATP-Dependent Conformational Changes Trigger Substrate Capture and Release by an ECF-Type Biotin Transporter.* J Biol Chem, 2015. Epub ahead of print

114.   Johnson, W.C.J., *Protein Secondary Structure and Circular Dichroism: A Practical Guide.* Proteins, 1990. **7**(3): p. 205-214.

115.   Kelly, S.M., Jess, T.J., and Price, N.C., *How to Study Proteins by Circular Dichroism.* Biochim Biophys Acta, 2005. **1751**(2): p. 119-139.

116.   Ranaghan, M.J., et al., *Green Proteorhodopsin Reconstituted into Nanoscale Phospholipid Bilayers (Nanodiscs) as Photoactive Monomers.* J Am Chem Soc, 2011. **133**(45): p. 18318-18327.

117.   Roman, E.A., Argüello, J.M., and González Flecha, F.L., *Reversible Unfolding of a Thermophilic Membrane Protein in Phospholipid/Detergent Micelles.* J Mol Bio, 2010. **397**(2): p. 550-559.

118.   Sokolowska, M., Pawlas, K., and Bal, W., *Effect of Common Buffers and Heterocyclic Ligands on the Binding of Cu(II) at the Multimetal Binding Site in Human Serum Albumin.* Bioinorg Chem Appl, 2010: 725153.

119.   Mandal, A.K., Cheung, W.D., and Argüello, J.M., *Characterization of a Thermophilic P-Type Ag^+/Cu^+-ATPase from the Extremophile Archaeoglobus Fulgidus.* J Biol Chem, 2002. **277**(9): p. 7201-7208.

120.   Koehorst, R.B., Spruijt, R.B., and Hemminga, M.A., *Site-Directed Fluorescence Labeling of a Membrane Protein with Badan: Probing Protein Topology and Local Environment.* Biophys J, 2008. **94**(10): p. 3945-3955.

121.   Parasassi, T. and Krasnowska, E., *Laurdan and Prodan as Polarity-Sensitive Fluorescent Membrane Probes.* Journal of Fluorescence, 1998. **88**(4): p. 365-373.

122.   Kawski, A., Kuklinski, B., and Bojarski, P., *Ground and Excited State Dipole Moments of Badan and Acrylodan Determined from Solvatochromic Shifts of Absorption and Fluorescence Spectra.* Z. Naturforsch. A, 2001. **56**(5): p.407-411

123.   Hammarström, P., et al., *High-Resolution Probing of Local Conformational Changes in Proteins by the Use of Multiple Labeling: Unfolding and Self-Assembly of Human*

Carbonic Anhydrase II Monitored by Spin, Fluorescent, and Chemical Reactivity Probes. Biophys J, 2001. **80**(6): p. 2867–2885.

124.   Wahl, M., *Time-Correlated Single Photon Counting.* Pico Quant Technical Note, 2014.

125.   Mandal, A.K. and Argüello, J.M., *Functional Roles of Metal Binding Domains of the Archaeoglobus Fulgidus Cu⁺-ATPase CopA.* Biochemistry, 2003. **42**(37): p. 11040-11047.

126.   Okkeri, J. and Haltia, T., *The Metal-Binding Sites of the Zinc-Transporting P-Type ATPase of Escherichia Coli. Lys693 and Asp714 in the Seventh and Eighth Transmembrane Segments of ZntA Contribute to the Coupling of Metal Binding and ATPase Activity.* Biochim Biophys Acta, 2006. **1757**(11): p. 1485-1495.

127.   González-Guerrero, M. and Argüello, J.M., *Mechanism of Cu⁺-Transporting ATPases: Soluble Cu⁺ Chaperones Directly Transfer Cu⁺ to Transmembrane Transport Sites.* Proc Natl Acad Sci U S A, 2008. **105**(16): p. 5992-5997.

128.   Jesenská, A., et al., *Nanosecond Time-Dependent Stokes Shift at the Tunnel Mouth of Haloalkane Dehalogenases.* J Am Chem Soc, 2009. **131**(2): p. 494-501.

129.   Toyoshima, C., et al., *Crystal Structures of the Calcium Pump and Sarcolipin in the Mg^{2+}-Bound E1 State.* Nature, 2013. **495**(7440): p. 260-264.

130.   Warschawski, D.E., et al., *Choosing Membrane Mimetics for NMR Structural Studies of Transmembrane Proteins.* Biochim Biophys Acta, 2011. **1808**(8): p. 1957-1974.

131.   Shaw, A.W., McLean, M.a., and Sligar, S.G., *Phospholipid Phase Transitions in Homogeneous Nanometer Scale Bilayer Discs.* FEBS Lett, 2004. **556**(1-3): p. 260-264.

132.   Koehorst, R.B.M., et al., *Profiling of Dynamics in Protein-Lipid-Water Systems: A Time-Resolved Fluorescence Study of a Model Membrane Protein with the Label BADAN at Specific Membrane Depths.* European Biophysics Journal, 2010. **39**(4): p. 647-656.

133.   Kucerka, N., et al., *Lipid Bilayer Structure Determined by the Simultaneous Analysis of Neutron and X-Ray Scattering Data.* Biophys J, 2008. **95**(5): p. 2356-2367.

134.   Schutz, C.N. and Warshel, A., *What Are the Dielectric "Constants" of Proteins and How to Validate Electrostatic Models?* Proteins, 2001. **44**(4): p. 400-417.

135.   Li, L., et al., *On the Dielectric "Constant" of Proteins: Smooth Dielectric Function for Macromolecular Modeling and Its Implementation in DelPhi.* J Chem Theory Comput, 2013. **9**(4): p. 2126-2136.

136.   Nielsen, J.E., Gunner, M.R., and Garcia-Moreno, B.E., *The pKa Cooperative: A Collaborative Effort to Advance Structure-Based Calculations of pKa Values and Electrostatic Effects in Proteins.* Proteins, 2011. **79**(12): p. 3249-3259.

137.   Autry, J.M., et al., *Nucleotide Activation of the Ca-ATPase.* J Biol Chem, 2012. **287**(46): p. 39070-39082.

138.   Solioz, M. and Vulpe, C., *CPx-Type ATPases: A Class of P-Type ATPases That Pump Heavy Metals.* Trends Biochem Sci, 1996. **21**(7): p. 237-241.

139.   Renthal, R., *Buried Water Molecules in Helical Transmembrane Proteins.* Protein Sci, 2008. **17**(2): p. 293-298.

140.   Allan, A.E. and Cooper, A., *Hydration of Retinal and the Structure of Metarhodopsin Ii.* FEBS Lett, 1980. **119**(2): p. 238-240.

141.   Okada, T., et al., *Functional Role of Internal Water Molecules in Rhodopsin Revealed by X-Ray Crystallography.* Proc Natl Acad Sci U S A, 2002. **99**(9): p. 5982-5987.

142.   Grossfield, A., et al., *Internal Hydration Increases During Activation of the G-Protein-Coupled Receptor Rhodopsin.* J Mol Biol, 2008. **381**(2): p. 478-486.

143. Aqvist, J. and Warshel, A., *Energetics of Ion Permeation through Membrane Channels. Solvation of Na$^+$ by Gramicidin A.* Biophys J, 1989. **56**(1): p. 171-182.

144. Guerra, F. and Bondar, A.N., *Dynamics of the Plasma Membrane Proton Pump.* J Membr Biol, 2014. Epub ahead of print.

145. Sonntag, Y., et al., *Mutual Adaptation of a Membrane Protein and Its Lipid Bilayer During Conformational Changes.* Nat Commun, 2011. **2**.

146. Mattle, D., et al., *On Allosteric Modulation of P-Type Cu$^+$-ATPases.* J Mol Biol, 2013. **425**(13): p. 2299-2308.

147. Gente, G. and Mesa, C.L., *Water—Trifluoroethanol Mixtures: Some Physicochemical Properties.* Journal of Solution Chemistry, 2000. **29**(11): p. 1159-1172.

148. Buck, M., *Trifluoroethanol and Colleagues: Cosolvents Come of Age. Recent Studies with Peptides and Proteins.* Q Rev Biophys, 1998. **31**(3): p. 297-355.

149. Roccatano, D., et al., *Mechanism by which 2,2,2-Trifluoroethanol/Water Mixtures Stabilize Secondary-Structure Formation in Peptides: A Molecular Dynamics Study.* Proc Natl Acad Sci U S A, 2002. **99**(19): p. 12179-12184.

150. Reed, J. and Reed, T.A., *A Set of Constructed Type Spectra for the Practical Estimation of Peptide Secondary Structure from Circular Dichroism.* Anal Biochem, 1997. **254**(1): p. 36-40.

151. Bechinger, B., *Understanding Peptide Interactions with the Lipid Bilayer: A Guide to Membrane Protein Engineering.* Current Opin Chem Biol, 2000. **4**(6): p. 639-644.

152. Gamble, A.J. and Peacock, A.F., *De Novo Design of Peptide Scaffolds as Novel Preorganized Ligands for Metal-Ion Coordination.* Methods Mol Biol, 2014. **1216**: p. 211-231.

Acknowledgements

Erklärung entsprechend §5.5 der Promotionsordnung

Hiermit versichere ich, dass ich die vorliegende Arbeit ohne unzulässige Hilfe Dritter und ohne Benutzung anderer als der angegebenen Hilfsmittel angefertigt habe; die aus fremden Quellen direkt oder indirekt übernommenen Gedanken sind als solche kenntlich gemacht. Die Arbeit wurde bisher weder im Inland noch im Ausland in gleicher oder ähnlicher Form einer anderen Prüfungsbehörde vorgelegt.

Die Dissertation wurde im Zeitraum vom 1. September 2011 bis 26. Juni 2015 angefertigt und von Prof. Dr. Karim Fahmy, Abteilung Biophysik, Institut für Ressourcenökologie, Helmholtz-Zentrum Dresden-Rossendorf betreut.

Meine Person betreffend erkläre ich hiermit, dass keine früheren erfolglosen Promotionsverfahren stattgefunden haben.

Hiermit erkenne ich die Promotionsordnung der Fakultät Mathematik und Naturwissenschaften der Technischen Universität Dresden an.

26. Juni 2015

Elisabeth Fischermeier